SINGLE-FRAME COMPLETE SPATIOTEMPORAL MEASUREMENT OF COMPLEX ULTRASHORT LASER PULSES

A Thesis
Presented to
The Academic Faculty

by

Zhe Guang

In Partial Fulfillment
of the Requirements for the Degree
Doctor of Philosophy in the
School of Physics

Georgia Institute of Technology

May 2016

SINGLE-FRAME COMPLETE SPATIOTEMPORAL MEASUREMENT OF COMPLEX ULTRASHORT LASER PULSES

Approved by:

Professor Rick Trebino, Advisor
School of Physics
Georgia Institute of Technology

Professor Ali Adibi
School of Electrical and
Computer Engineering
Georgia Institute of Technology

Professor Jennifer Curtis
School of Physics
Georgia Institute of Technology

Professor Michael Chapman
School of Physics
Georgia Institute of Technology

Professor Zhigang Jiang
School of Physics
Georgia Institute of Technology

Date Approved: March 18, 2016

Dedicated to my parents, and my wife Guimin Xia

ACKNOWLEDGEMENTS

I would like to express the deepest gratitude for my Ph.D. advisor, Prof. Rick Trebino, for his patient education and careful guidance over the years. He is not only an excellent professor with abundant knowledge and great understanding of ultrafast optics, but also a friendly mentor who has helped me a lot on my study, career and life. Especially, I would thank him for his numerous enlightening ideas, many comprehensive tutorials in classes and meetings, and kind and helpful instructions on academic affairs. He has given me the opportunity and confidence to pursue my career in research, without whose relentless efforts this work would never become possible. Also, I am grateful for the encouragement and care from my thesis committee members: Prof. Ali Adibi, Prof. Jennifer Curtis, Prof. Michael Chapman, and Prof. Zhigang Jiang. Thanks for all of you!

There are also many colleagues I am thankful for in the ultrafast optics lab. Some of us used to work together, including Jeff Wong, Michelle Rhodes, Patrick Gartland, Saidur Rahaman, Fumin Zhang, Dongjoo Lee, Aziz Rahaman and Ping Zhu. They have offered me great tips on how to conduct optical experiment and how to perform computer signal processing and simulation. Their collaborations and discussions on research topics and other projects were usually deep in thoughts and very helpful. Also, I would like to express my thanks for people working at the School of Physics. Many of them helped me in various manners, resolving academic or administrative issues over the years for my graduate study.

In addition, I would like to show my appreciation for the support from many friends around our group and in Atlanta. Especially, I would thank Ms. Linda Trebino, who is always so energetic, so enthusiastic, and so encouraging, that she handed me the most valuable help and sweet advice when I was in a difficult and suppressed state. I also thank my classmates in School of Physics, members of GTCFA, and colleagues in OSA

and SPIE student chapters, for their companion and friendship.

For the financial support of my graduate study and dissertation work, I am thankful for the School of Physics at Georgia Tech, the National Science Foundation and the Georgia Research Alliance.

Finally, I would like to thank my parents who have been always there to support, and my wife for her endless love.

TABLE OF CONTENTS

LIST OF TABLES

LIST OF FIGURES

LIST OF SYMBOLS

Variables

a,b	beam width parameter
a',b'	modified beam width parameter
A, B, C, D	element of conventional beam matrix
c	speed of light in vacuum, pulse duration parameter
C_0	pulse distortion constant
E	electric field
E_{arb}	arbitrary electric field
$\tilde{E}$	electric field in frequency
E'	electric field in FROG retrieval
E, F, G, H, I	field
I	intensity
$\vec{k}$	wavevector
k	wavevector magnitude
n	refractive index
n_2	nonlinear refractive index
P	matrix element in spatial-frequency-temporal domain
q	beam propagation parameter
Q	element of spatiotemporal field matrix
R	radius of curvature of beam, red color, spatiospectral matrix element
S	spectral intensity, or matrix element in spatial-frequency-spectral domain
t	time
t_0	time offset

T	delay
v	frequency
w_{lp}	LP mode weight
x	displacement
x_0	horizontal displacement offset
x,y,z	Cartesian coordinates

Greek Symbols

α, β	crossing angle
Δ	width, range or duration
λ	wavelength
λ_0	central wavelength
ω	angular frequency
ω_0	central angular frequency
Ω	angular frequency corresponds to relative delay
ϕ	temporal phase
φ	spectral phase
τ	relative delay
θ	angle

Subscripts/Superscripts

0	center value or offset amount
eff	effective
i	index, imaginary unit
in	input beam

out	output beam
ref	reference pulse
sig	signal pulse
unk	unknown pulse
x,y,z	spatial coordinates

LIST OF ABBREVIATIONS

2DFT	two-dimensional Fourier transform
AC	alternating-current
AGD	angular dispersion
ANDF	apodizing neutral density filter
BS	beam splitter
DOE	diffractive optical element
FM	flip mirror
FROG	frequency-resolved optical gating
FT	Fourier Transform
FWHM	full width half maximum
IBPF	interference band-pass filter
IFT	inverse Fourier transform
Im	imaginary part
LP	linearly-polarized
MDM	mode-division multiplexing
MIR	mid-infrared
MMF	multimode fiber
NIR	near-infrared
PG	polarization gating
PFT	pulse-front tilt
Re	real part
RGB	red, green, and blue colors

RMS	root mean squared
SD	self diffraction
SF	self-focusing
SHG	second harmonic generation
SMF	single mode fiber
SMS	singlemode-multimode-singlemode
SPC	spatial chirp
SPM	self-phase modulation
STC	spatiotemporal coupling
STRIPED FISH	spatially and temporally resolved intensity and phase evaluation device: full information from a single hologram
TCP	temporal chirp
TG	transient grating
THG	third harmonic generation
WFD	wave-front tilt dispersion
UV	ultraviolet

SUMMARY

The improvement of light measurement techniques has made possible a great list of scientific discoveries in human history. For example, the invention of telescope and microscope broadened horizons of human-beings for astronomy and biology; X-ray crystallography led to the discovery of DNA; atomic spectrum and Michelson interferometer led to breakthroughs in quantum mechanics and the theory of relativity. Today, one of the key frontiers in light measurement is to measure ever more fast and complex light events. Ultrashort pulses (nowadays down to attoseconds) from ultrafast laser systems, as one of the shortest events ever created by human-beings, demonstrate extremely fast variations in time, which are necessarily associated with large spectral bandwidths by Fourier transform. In addition to temporal and spectral structures, ultrashort pulses can also be complex over space, showing beam profiles other than simple plane waves or Gaussian beams. Moreover, pulse temporal and spectral structures can generally depend on space, which requires the field to be characterized over space and time simultaneously rather than separately. Therefore, a complete measurement is needed for pulse spatiotemporal information, which can facilitate many applications such as chirped pulse amplification, pulse shaping and manipulation, laser material processing, and so on.

Being an important field of study, measurement of ultrashort pulses has never been a trivial problem. Pulses from most (mode-locked) ultrafast lasers today, have temporal variations faster than the detectable speed of electronics, so they can only be

characterized by nonlinear-optical approaches. For example, Frequency Resolved Optical Gating (FROG), as the first accurate temporal pulse measurement method, has been developed for many different pulse durations and wavelengths, using different optical nonlinearities. However, FROG requires spatially simple pulses to work with, and it yields almost only the temporal and spectral field information. As stated, nevertheless, many pulses of interest are spatially complex, and can contain significant spatiotemporal couplings. Therefore, many methods have been proposed over the years for spatiotemporal measurement. Most of them though, only yield partial information: methods which can measure pulse temporal profile with a one-dimensional trace, such as Spectral Interferometry, can be extended to include one spatial dimension, yielding $E(x,t)$ or $E(x,\omega)$ by using a two-dimensional camera. The resulting measurements are incomplete over space, either cropping or averaging over the missed spatial dimension. Otherwise, assumptions are required about spatial homogeneity or certain symmetry, which may not be valid in practice. To obtain the full information, naturally, there have been trials to perform scans over space, time, or frequency. Some scanning-based methods could yield complete spatiotemporal pulse information, such as SEA TADPOLE, but they require many shots, which sets requirements on laser source stability, optomechanical accuracy, the complexity to operate, and the length of time to measure. Using them to measure potentially unstable pulses or low-repetition-rate system would therefore be practically very difficult. Therefore, an easy-to-operate, single-frame pulse measurement method is needed, for potential spatiotemporal structures in pulses.

In this work, we demonstrate our study on measuring complex ultrashort pulses

with spatiotemporal structures by development of a method called Spatially and Temporally Resolved Intensity and Phase Evaluation Device: Full Information from a Single Hologram (STRIPED FISH). Based on digital holography, this simple single-frame method can measure the complete spatiotemporal intensity $I(x,y,t)$ and the phase $\phi(x,y,t)$ of arbitrary ultrashort pulses at a particular z-plane (the measurement plane). From the recorded frame (also known as the "STRIPED FISH trace"), we can inspect and retrieve the unknown pulse information, and then we can calculate diffraction integral to propagate the measured pulse over z, yielding a complete spatiotemporal characterization. In order to display the measured pairs of high-dimensional intensity-and-phase data, we also developed a method to generate intuitive movies over time and space, showing the measured spectral components varying over time at all spatial locations. In apparatus, we have improved the STRIPED FISH device by increasing the number of holograms and measurable bandwidth, improving the hologram intensity homogeneity, and eliminating most optical aberrations. We demonstrate our measurement capability by investigating complex pulses, including sub-picosecond crossed and chirped double pulses (the "Chirped Pulse Beating"), output pulses from multimode optical fiber, pulses with ultrafast lighthouse effect, and so on. Also, we perform numerical simulations on STRIPED FISH traces to understand the effects of different spatiotemporal pulse structures. With these developments and understandings, we believe that STRIPED FISH, together with its processing algorithm and display method, is an excellent candidate to inspect, measure, and demonstrate spatiotemporal pulse structures.

CHAPTER 1

INTRODUCTION

The birth of laser in 1960s opened up a new era for optics. Many interesting scientific applications have ever since emerged in subjects like nonlinear optics, holography, spectroscopy, and quantum optics [1-4]. Among these, ultrafast optics is a fast-developing, fascinating area that frequently draws people's attention. Ultrafast optics deals with short pulses in time scale ranging from nanosecond (10^{-9}s) to attosecond (10^{-18}s), generated from a variety of pulsed laser systems by approaches like Q-switching and mode-locking. Pulses with their ultrashort temporal duration, relatively broad spectral bandwidth, and extremely high peak intensity, lead to special academic interests in ultrafast phenomena, broadband spectroscopy, nonlinear optical effects, and so on [5, 6].

1.1 Temporal Pulse Measurement

For better manipulation, after their generation, ultrashort pulses need to be characterized, to know their detailed pulse shape, or at least, to be proven ultrashort. However, as ultrashort pulses vary a lot faster (typically on order of $\sim < 10^{-13}$s) than electronics detection speed (typically ~>10^{-10}s), getting knowledge of pulse temporal information keeps being challenging. Moreover, as the intensity vs. time only represents half of the pulse temporal information, the other half information, the phase, is generally blind to electronic devices. Phase information, however, is in many cases more important than the intensity: the temporal phase tells us how fast the electrical field is oscillating,

and the spectral phase tells the frequency evolution in the pulse. As a result, people have been developing techniques to capture both intensity and phase information, temporally or spectrally by:

$$E(t) = \mathrm{Re}\{\sqrt{I(t)}\exp[i(\omega_0 t - \phi(t))]\} \quad (1.1)$$

$$\tilde{E}(\omega) = \sqrt{S(\omega)}\exp[-i\varphi(\omega)] \quad (1.2)$$

$$\tilde{E}(\omega) = FT\{E(t)\} \quad (1.3)$$

$$E(t) = IFT\{\tilde{E}(\omega)\} \quad (1.4)$$

where $I(t)$ and $\phi(t)$ are the temporal intensity and temporal phase, and $S(\omega)$ and $\varphi(\omega)$ are the spectral intensity (also known as spectrum) and spectral phase. The temporal and spectral fields, $E(t)$ and $\tilde{E}(\omega)$, are related by Fourier transform and Inverse Fourier transform.

Two decades ago, our research group developed the first technique to completely determine the temporal profile of ultrashort laser pulses, called Frequency-Resolved Optical Gating (FROG) [7, 8], which measures the pulse intensity and phase vs. time or frequency without the need for a previously characterized reference pulse. FROG is now in use for pulse measurement in many ultrafast-optics labs around the world. It can measure pulses of many wavelengths from UV to MIR [9-11] and durations from nanoseconds [12] down to attoseconds [13].

FROG, however, is designed for measuring spatially fairly simple, uniform pulses, without obtaining much information on their spatial profile. However in fact, as most objects in nature are also spatially complex, light emerging from them must also necessarily be. Therefore, both temporal and spatial properties of pulses can be important to contain vast information, which calls for techniques that can simultaneously

characterize them.

1.2 Spatiotemporal Pulse Characterization

Over centuries, many efforts have been devoted to measure spatial intensity of light, but they almost always average over the fast temporal variation. Great achievements have attested by photography, by recording time-integrated intensity distribution. Also, spatial phase information can be measured by performing holography, usually with narrowband coherent laser sources. However, for ultrashort laser pulses, the situation is more complex, in that their temporal profiles are rarely the same from location to location, or equivalently their spatial profiles are varying from time to time. These field couplings are called spatiotemporal couplings (STC) or spatiotemporal distortions, depending on whether they are useful or detrimental for certain applications. Though very essential structures, unfortunately, spatial measurements that average over time, or temporal measurements that average over space do not measure STCs. Therefore, STCs almost always get ignored and unmeasured, except for very slowly varying cases.

We hope to develop a technique to completely measure an arbitrary laser pulse, preferably with no assumptions. By incorporating also the spatial dimensions, the complete pulse electric field E is expressed by temporal intensity I and phase ϕ over space x, y, z and time t:

$$E(x,y,z,t) = \mathrm{Re}\{\sqrt{I(x,y,z,t)}\exp\big[i\big(\omega_0 t - \phi(x,y,z,t)\big)\big]\} \tag{1.5}$$

or, equivalently, spatiospectral quantities vs. x, y, z and angular frequency ω:

$$\tilde{E}(x,y,z,\omega) = \sqrt{S(x,y,z,\omega)}\exp[-i\varphi(x,y,z,\omega)] \tag{1.6}$$

Note that, in both expressions here, the spatial field dependence and temporal (or spectral) field dependence are not separable, i.e. $E(x,y,z,t) \neq E(x,y,z) \times E(t)$ or $\tilde{E}(x,y,z,\omega) \neq \tilde{E}(x,y,z) \times \tilde{E}(\omega)$. For each position (x,y,z), similar as before, field temporal and spectral expressions are related by Fourier transform and Inverse Fourier transform:

$$\tilde{E}(x,y,z,\omega) = FT\{E(x,y,z,t)\} \tag{1.7}$$

$$E(x,y,z,t) = IFT\{\tilde{E}(x,y,z,\omega)\} \tag{1.8}$$

Once at a certain z-plane, the electric field vs. x, y, and t (or ω) is determined, the field z-dependence can always be obtained by propagating the field diffraction integrals [2]. As a result, the z-dependence of most quantities are ignored in expressions of this thesis.

1.3 Spatiotemporal Measurement Techniques

As mentioned above, ultrashort laser pulses can have many applications, and most such applications operate best with pulses that have stable and simple (or at least known) intensity and phase profile over time and space. Unfortunately, there are an abundance of spatiotemporal couplings that ultrafast lasers can suffer from. Some of them can be useful in applications like coherent control, pulse compression, and nonlinear optics [14-18], but most are not. For example, in Kerr-lens mode-locked lasers, the output mode size can depend on frequency [19]. Since dispersive and focusing optics are ubiquitous in ultrafast laser systems, numerous spatiotemporal distortions can occur, such as radial dispersion and chromatic aberration [20-23]. Moreover, ultrashort pulses, especially amplified ones, have extremely high intensities, so significant intensity-related nonlinear-optical effects

can distort pulses as they propagate through optics [24-28]. These distortions can be problematic, because they vary from shot to shot when intensity fluctuates, especially in high-intensity low-rep-rate amplification systems, where the shot-to-shot variation can be significant. As a result, a technique that can measure the complete spatiotemporal profile of pulses (intensity and phase) can be very helpful, and a simple, single-frame method is preferred for operation, especially for low-rep-rate, or potentially unstable pulses.

Unfortunately, complete spatiotemporal characterization of ultrashort laser pulses remains very challenging. As discussed above, simple temporally averaged spatial measurements by camera, or spatially averaged temporal measurements by using techniques like FROG are not sufficient to characterize the entire field. A single-shot version of FROG and its simplified cousin GRENOUILLE [29, 30], have been shown to characterize some distortions, but they are very simple ones [31, 32]. For practical usage, a more powerful technique is needed to characterize more complex laser pulse spatiotemporal structures.

Recently, to resolve the spatiotemporal measurement problem, a number of techniques that yield partial solutions have been proposed and demonstrated [33, 34]. Beginning with methods that measure pulse temporal profile $E(t)$ by using a recorded one-dimensional trace (such as Spectral Interferometry, which also requires a temporally known reference pulse), it is straightforward to extend the measurement by using a two-dimensional camera to also include a spatial dimension, i.e. $E(x,t)$ or $E(x,\omega)$ [35-41]. The resulting measurement, however, remains incomplete over space (either cropping or averaging over the missed spatial dimension). And assumptions can be made about spatial homogeneity or spatial symmetry, which may not be valid in practice. To obtain

the additional dimension, one must spatially scan over it.

There are also some techniques which combine spatial measurements with temporal measurements. Shackled FROG [42, 43] and HAMSTER [44] are based on combining a Shack-Hartmann spatial sensor with a FROG apparatus. The Shack-Hartmann sensor yields the spatial wave-front and spatial amplitude information, and a FROG measurement of the central part (or anywhere else that contains all the frequency components) stitches the results together. These methods are limited, however, because they must assume the same spatial phase for each monochromatic component [42] or must scan over all frequencies [45]; otherwise, the obtained information is spatially incomplete [43].

It is helpful to generate a spatiotemporally known reference pulse or reference train of pulses to assist the measurement. This can be accomplished by spatially filtering the pulse to achieve a spatially simple (and known) beam profile and then measuring the resulting spatially simple pulse over time [46, 47]. Most such reference-pulse-assisted methods still involve scan over spatial dimensions, among which the most popular ones include SEA TADPOLE [48] and STARFISH [49]. These methods can measure pulses over space and time completely, i.e. yielding $E(x, y, t)$. As both SEA TADPOLE and STARFISH scan fibers to probe pulses, they can have very high spatial resolutions, usually defined by fiber facet size. As with all spatial or spectral scanning techniques [50-53], however, these methods require many shots (finer the resolution, more shots will be required) and long operation time (up to ~>30mins per measurement), rendering them inapplicable for potentially unstable laser sources or low-repetition-rate pulse systems. Therefore we need a more convenient, faster, and preferably single-frame method to

measure spatiotemporal structures of pulses, especially those from complex optics that incur spatiotemporal couplings can be of greater interest.

1.4 STRIPED FISH

To solve the problem, we recently introduced a single-frame technique for complete spatiotemporal pulse measurement (intensity and phase, over x, y, z, t and ω). It is called Spatially and Temporally Resolved Intensity and Phase Evaluation Device: Full Information from a Single Hologram (STRIPED FISH) [54, 55]. It comprises of a simple setup, and uses a spatially filtered known reference pulse to complete the measurement. The information of the unknown pulse (to be measured) can be fully retrieved from multiple holograms imaged onto a single camera frame. For the details of STRIPED FISH apparatus and retrieval algorithm, please see Chapters 3.

In its proof-of-principle demonstration [56], the initial device of STRIPED FISH measured some simple basic pulse distortions, such as temporal chirp and spatial chirp. But, as with any new device, the initial implementation had many limitations to overcome. For the limitations and improvements about the device, please also see Chapter 3, and possible future development is discussed in Chapter 8.

1.5 Outline

The thesis is divided into 8 Chapters. Chapter 1 is an overall introduction. Chapter 2 is the background of ultrafast optical measurement, containing an introduction to FROG, spatiotemporal field and propagation formulism, and fundamentals in digital holography. Chapter 3 covers the STRIPED FISH apparatus and algorithm, previous

device limitations and apparatus improvement, and discusses the display and propagation methods for STRIPED FISH measured results. Chapter 4 presents the simulation of STRIPED FISH traces for pulses with typical spatiotemporal structures. Chapter 5 is an experimental study of the chirped pulse beating phenomenon, showing the measurement capability of STRIPED FISH. Chapter 6 studies the propagation modes in multimode optical fibers, by measuring the output pulses from several different fibers. Chapter 7 investigates pulse with ultrafast lighthouse effect and its propagation, generated by focusing a pulse with pulse-front tilt. Finally, Chapter 8 gives the conclusion of this work and potentials for future developments.

CHAPTER 2

THEORETICAL BACKGROUND

This chapter contains an introduction to ultrashort pulse measurement, fundamentals in spatiotemporal pulse-field formulism, and digital holography model to retrieve pulses over space and time. In Section 2.1, the nonlinear optical methods to measure ultrashort pulse temporal profile are discussed. In Section 2.2, propagation properties of pulses, such as the beam displacement and direction in free space and dispersive optical media, are discussed based on conventional ABCD matrix and Kostenbauder matrix; and the first-order Gaussian theory of spatiotemporal pulse field couplings is introduced. Finally, in Section 2.3, holographic method to measure coherent spatial light is reviewed. When holograms are formed by interference between reference and unknown pulses at multiple different frequencies, the holographic model to measure ultrashort laser pulses is discussed.

2.1 Nonlinear Optical Methods for Temporal Pulse Measurement

As we have mentioned briefly before, the electronic detection methods (photodiodes, oscilloscopes, etc.) are too slow to detect pulse temporal profile variation which can typically be on a time scale of femtosecond. As a result, over the years people have developed nonlinear optical methods for measurement. For the first several decades of research in this field, researchers made do with quite rough estimates of pulse duration available from autocorrelation methods [57-59], which missed pulse phase information, and had to work under assumptions (otherwise with ambiguity). It was not until the early

1990s that a technique was invented to first measure the actual pulse temporal intensity $I(t)$ and phase $\phi(t)$ [7, 8, 60]. This method, Frequency-Resolved Optical Gating (FROG), has been adapted with several different optical nonlinearities.

The principle of FROG to work is as follows. Firstly, a spectrogram $I_{FROG}(\omega,\tau)$ is recorded from experiment as an FROG trace of the pulse field $E(t)$, under a certain optical nonlinearity. In other words, the FROG trace is equivalent a spectrally resolved version of pulse field correlation function, in which the pulse temporally gates itself. For example, the polarization-gating (PG) FROG:

$$I_{FROG}^{PG}(\omega,\tau) = |\int_{-\infty}^{\infty} E(t)|E(t-\tau)|^2 \exp(-i\omega t)dt\,|^2 \tag{2.1}$$

where I_{FROG}^{PG} is the intensity measured on camera, τ is the relative delay between the pulse field $E(t)$ and the polarization gating $|E(t)|^2$.

If we write the signal field $E_{sig}(t,\tau) = E(t)|E(t-\tau)|^2$ by Fourier transform with respect to τ, we get:

$$E_{sig}(t,\tau) = \int_{-\infty}^{\infty} \bar{E}_{sig}(t,\Omega)\exp(-i\Omega\tau)d\Omega \tag{2.2}$$

Note that if we know the form of either $E_{sig}(t,\tau)$ or $\bar{E}_{sig}(t,\Omega)$, the pulse field could be easily retrieved. $\bar{E}_{sig}(t,\Omega)$ is by Fourier transform equivalent to $E_{sig}(t,\tau)$. Just by substituting $t=\tau$, we can get $E_{sig}(t,t) = E(t)|E(0)|^2$, which is proportional to $E(t)$. Once the form of $E(t)$ is known, we can determine the absolute pulse amplitude by normalizing the field to the measured integrated power.

Now we can write the spectrogram $I_{FROG}^{PG}(\omega,\tau)$ in terms of $\bar{E}_{sig}(t,\Omega)$ as:

$$I_{FROG}^{PG}(\omega,\tau) = |\int_{-\infty}^{\infty}\int_{-\infty}^{\infty} \bar{E}_{sig}(t,\Omega)\exp(-i\omega t - i\Omega\tau)dt\,d\Omega\,|^2 \tag{2.3}$$

within the magnitude square is a two dimensional Fourier transform of field $\bar{E}_{sig}(t,\Omega)$ with respect to t and Ω. Now our goal to retrieve the pulse field $E(t)$ turns to know the

overall phase of this two dimensional Fourier transform, which is the so-called two-dimensional phase-retrieval problem.

Luckily, this two-dimensional phase-retrieval problem has an essentially unique solution [7], when it has the finite support that a finite range of t and Ω values are surrounded by zeros outside. Further, depending on the type of optical nonlinearity, different mathematical form constraints can be applied to the retrieved field. Generally, the FROG trace $I_{FROG}(\omega,\tau)$ on camera is,

$$I_{FROG}(\omega,\tau) = |\int_{-\infty}^{\infty} E_{sig}(t,\tau)\exp(-i\omega t)dt\,|^2 = |\tilde{E}_{sig}(\omega,\tau)|^2 \qquad (2.4)$$

with the signal field $E_{sig}(t,\tau)$ dependent on the used nonlinearity:

$$E_{sig}(t,\tau) = \begin{cases} E(t)E(t-\tau) & SHG\ FROG \\ E(t)^2E(t-\tau) & THG\ FROG \\ E(t)|E(t-\tau)|^2 & PG\ FROG \\ \dots & \dots \end{cases}. \qquad (2.5)$$

The FROG trace $I_{FROG}(\omega,\tau)$ is treated as the measured data constraint. To retrieve the pulse, as in Figure 2.1, first we start from an initial guess for $E(t)$ and generate $E_{sig}(t,\tau)$ following the above forms. Then $E_{sig}(t,\tau)$ is Fourier transformed with respect to t to get the signal field $\tilde{E}_{sig}(\omega,\tau)$ in spectral domain. Since magnitude of $\tilde{E}_{sig}(\omega,\tau)$ should always be equal to the square root of the measured FROG trace $I_{FROG}(\omega,\tau)$, as shown by Equation (2.4), we can generate an improved field $\tilde{E}'_{sig}(\omega,\tau)$, and then Fourier transform it into time domain to get $E'_{sig}(t,\tau)$. Then a next new guess is generated on $E(t)$, which starts another iteration toward the accurate solution.

Eventually, using algorithms like the Vanilla algorithm or the generalized projections algorithm [7], this two-dimensional phase retrieval problem can be solved, with the retrieved trace in good agreement with the measured trace from experiment. In

reality, due to presence of noise and other measurement errors (such as quantization, digitization, instability, etc.), typically the retrieved result is considered trustable when the retrieved trace and the measured trace are agreed within a small RMS error [7].

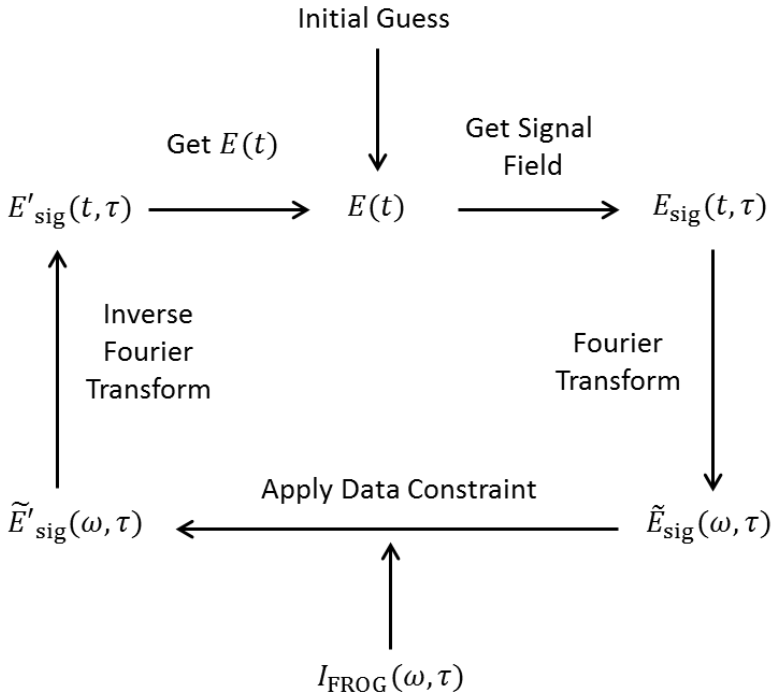

Figure 2.1. The iteration process in FROG retrieval algorithm, to solve the two-dimensional phase retrieval problem, by using the measured data constraint and mathematical form constraint. The process starts from an initial guess of $E(t)$, which can be random noise, approaches the essentially unique solution by each iteration, and finally converges to the accurate solution when the retrieved and measured FROG traces match within a small RMS error. Figure as in Ref. [7].

In addition to the FROG family (SHG-FROG, THG-FROG, TG-FROG, PG-FROG, SD-FROG, etc.), there are also interferometric nonlinear optical methods that can carry out direct retrieval and sensitive measurements of the pulse temporal or spectral profile. For example, Spectral Phase Interferometry for Direct Electric-field Reconstruction (SPIDER) [61, 62] uses the spectral shearing interferometry and retrieves the pulse field from an interferometric trace obtained from two spectrally-sheared pulse copies, separated by a certain delay. However, even if the pulse retrieval in SPIDER is

more direct, SPIDER needs a comprehensively complex apparatus, which can be vulnerable to noises and many kinds of errors. More severely, SPIDER and other interferometric pulse measurement techniques could suffer measuring the coherent artifact, and yield erroneous retrieval on unstable pulse trains [63, 64]. Some specific cases, such as unstable multi-pulsing of ultrafast lasers, and fluctuating pulses from high energy pulse amplifiers, can also be problematic for such methods in retrieval, and they require single-shot operations to achieve accurate results.

As we will see in the next chapter, based on digital holography, a simple single-frame measurement technique has been developed for complete spatiotemporal pulse profile, which remedies the above-mentioned problems.

2.2 Formulism of Pulse Profiles and Propagation

In laser optics and ultrafast optics, there are electric field formulism used to describe beam and pulse formation and propagation. Following a conventional way to describe laser beam, the ABCD matrix (or ray matrix) models as:

$$\begin{pmatrix} x_{out} \\ \theta_{out} \end{pmatrix} = \begin{pmatrix} A & B \\ C & D \end{pmatrix} \begin{pmatrix} x_{in} \\ \theta_{in} \end{pmatrix}. \tag{2.6}$$

where the beam displacements x_{in} and x_{out}, and angles θ_{in} and θ_{out} are assumed to be small; the coefficients A and D represent spatial and angular magnifications respectively, and B and C represent couplings of space and angle. Using this formulism, laser beam propagation in free space, optical medium, and curved-interface optics (such as lens and mirrors) can all be modeled. The Gaussian beam propagation can be easily calculated by using the q-parameter, defined by:

$$\frac{1}{q(z)} = \frac{1}{R(z)} - i\frac{\lambda}{\pi w^2(z)} \tag{2.7}$$

where R is the radius of curvature at a certain z location, λ is the beam wavelength, and w is the beam radius, representing the beam size at a certain z location.

The q-parameter algebra is, where q_{in} is the input parameter to optical system, q_{out} is the output parameter:

$$q_{out} = \frac{Aq_{in}+B}{Cq_{in}+D} \tag{2.8}$$

Based on the ABCD matrix, to adjust for the needs to model ultrashort pulses, Kostenbauder et al. expanded the matrix to also include time and frequency dimensions, which can describe pulse propagation over space and time [65]. The Kostenbauder matrix goes as:

$$\begin{pmatrix} x_{out} \\ \theta_{out} \\ t_{out} \\ v_{out} \end{pmatrix} = \begin{pmatrix} A & B & 0 & E \\ C & D & 0 & F \\ G & H & 1 & I \\ 0 & 0 & 0 & 1 \end{pmatrix} \begin{pmatrix} x_{in} \\ \theta_{in} \\ t_{in} \\ v_{in} \end{pmatrix} \tag{2.9}$$

where the $ABCD$ components are as before in the conventional form, E, F, I, G, H represent the effects of spatial chirp, angular dispersion, group delay dispersion, pulse-front tilt, and time vs. angle respectively. This 4×4 matrix can therefore be used conveniently to model the spatiotemporal pulse effects. Also, propagation of pulses through optics can be calculated by using the Kostenbauder matrix and a 2×2 Q-matrix (in analogy to the complex q-parameter before),

$$Q = \begin{pmatrix} Q_{11} & Q_{12} \\ Q_{21} & Q_{22} \end{pmatrix} = i\frac{\lambda_0}{\pi} \begin{pmatrix} \tilde{Q}_{xx} & \tilde{Q}_{xt} \\ -\tilde{Q}_{xt} & \tilde{Q}_{tt} \end{pmatrix}^{-1} \tag{2.10}$$

where Q_{11}, Q_{12}, Q_{21} and Q_{22} are elements of Q-matrix, and $Q_{21} = -Q_{12}$; λ_0 is the central wavelength of the pulse, and coefficients $\tilde{Q}_{xx}$, $\tilde{Q}_{xt}$, and $\tilde{Q}_{tt}$ are as presented in Equation (2.14) below. The diagonal elements are:

$$\tilde{Q}_{xx} = -i\frac{\pi}{\lambda_0 R(z)} - \frac{1}{w^2(z)} \tag{2.11}$$

$$\tilde{Q}_{tt} = -i\beta + \frac{1}{\tau^2} \tag{2.12}$$

The propagation rule of Q-matrix is

$$Q_{out} = \frac{\begin{pmatrix} A & 0 \\ G & 1 \end{pmatrix} Q_{in} + \begin{pmatrix} B & E/\lambda_0 \\ H & I/\lambda_0 \end{pmatrix}}{\begin{pmatrix} C & 0 \\ 0 & 0 \end{pmatrix} Q_{in} + \begin{pmatrix} D & F/\lambda_0 \\ 0 & 1 \end{pmatrix}} \tag{2.13}$$

where Q_{in} and Q_{out} are the Q-matrix before and after optical system.

To more accurately describe pulse spatiotemporal couplings, and their formation and relation, Akturk et al. [66] developed a general theory on first-order spatiotemporal distortions of Gaussian pulses and beams. This theory is used later in our work, thus being introduced here.

When a pulse shows spatiotemporal coupling, it at least contains a coupling term between space (or spatial frequency) and time (or frequency). The simplest case is when the coupling term is first-order in the Gaussian expression. Specifically, if we start from the spatiotemporal domain, we have the pulse field $E(x,t)$:

$$E(x,t) \propto \exp\{Q_{xx}x^2 + 2Q_{xt}xt - Q_{tt}t^2\} \tag{2.14}$$

the coupling coefficient Q_{xt} is complex. The real part $Re\{Q_{xt}\}$ represents the pulse amplitude coupling between space x and time t, therefore it represents the pulse-front tilt. The imaginary part $Im\{Q_{xt}\}$ is an indication of wave-front rotation, which is a phase coupling effect between space and time--the pulse wave-front will change its direction as time goes on.

If we take Fourier transform of $E(x,t)$ with respect to time t, we can get an expression in a similar form, as a Gaussian expression will always transform to a Gaussian. The new spatiospectral domain field $E(x,\omega)$ is:

$$E(x,\omega) \propto \exp\{R_{xx}x^2 + 2R_{x\omega}x\omega - R_{\omega\omega}\omega^2\} \tag{2.15}$$

Now, the real part of coupling coefficient $R_{x\omega}$ represents the spatial chirp, which means the spectral component of the pulse at ω will change as a function of spatial coordinate x. On the other hand, the imaginary part of coefficient $R_{x\omega}$ denotes the wave-front tilt dispersion, which describes the wave-front direction change with respect to frequency ω. We will see more effects of these two coupling terms in the following chapters. These amplitude and phase couplings are important because STRIPED FISH works in the spatiospectral domain—from multiple holograms, the unknown pulse spatial field is retrieved at multiple different frequencies.

Further, if we then take Fourier transform of $E(x,t)$ over space x, we can get field expression for the spatial-frequency-time (k,t) domain:

$$E(k,t) \propto \exp\{P_{kk}k^2 + 2P_{kt}kt - P_{tt}t^2\}. \tag{2.16}$$

This expression turns to be of vital importance for measuring the ultrafast lighthouse effect, which we will cover in more details in Chapter 7. The amplitude coupling term $Re\{P_{kt}\}$ represents ultrafast lighthouse effect, also named as time vs. angle. The phase coupling term $Im\{P_{kt}\}$ is called angular temporal chirp.

Lastly, for completeness, we also list the field expression for spatial-frequency-spectral (k,ω) domain, which can be obtained by either Fourier transform over time t from $E(k,t)$, or over space x from $E(x,\omega)$:

$$E(k,\omega) \propto \exp\{S_{kk}k^2 + 2S_{k\omega}k\omega - S_{\omega\omega}\omega^2\}. \tag{2.17}$$

Now the amplitude coupling term $Re\{S_{k\omega}\}$ describes the angular dispersion, which is an important effect used in every grating to separate colors into different angles. The phase coupling term $Im\{S_{k\omega}\}$ is named angular spectral chirp, but this term is not causing much attention in practice.

So far we have covered the Kostenbauder matrix method, Q-matrix propagation, and first-order spatiotemporal coupling theory in four Fourier transform domains. Using these pulse field and propagation formulism, one can well describe the pulse behaviors and distortions under paraxial approximation (where the beam displacement and angle are small and sufficient to be modeled by linear terms).

2.3 Digital Holography with Ultrashort Pulses

Basic principles of digital holography have been developed decades ago, and are presented in many textbooks. Typically, a hologram $I(x,y)$ is recorded over space at a certain frequency ω_0:

$$I(x,y) = |E_{unk}(x,y)|^2 + \left|E_{ref}(x,y)\right|^2 + 2|E_{unk}(x,y)E_{ref}(x,y)|\cos(\varphi_{unk}(x,y) - \varphi_{ref}(x,y) + \frac{y\omega_0}{c}\theta) \quad (2.18)$$

where θ is the beam crossing angle between the unknown light field $E_{unk}(x,y)$ and the reference light field $E_{ref}(x,y)$, $\varphi_{unk}(x,y)$ and $\varphi_{ref}(x,y)$ are their corresponding phases, and c is the speed of light.

To retrieve the unknown field information $E_{unk}(x,y)$, from the recorded intensity $I(x,y)$ on camera, one can perform the Fourier filtering algorithm [67] to obtain the oscillating term (cosine term in Equation (2.18)) which contains the complex field of our interest. Equivalently, this oscillating term can be written as:

$$\begin{aligned} &2|E_{unk}(x,y)E_{ref}(x,y)|\cos(\varphi_{unk}(x,y) - \varphi_{ref}(x,y) + \frac{y\omega_0}{c}\theta) \\ &= E_{unk}(x,y){E_{ref}}^*(x,y)\exp(+i\frac{y\omega_0}{c}\theta) \\ &+E_{ref}(x,y){E_{unk}}^*(x,y)\exp(-i\frac{y\omega_0}{c}\theta) \end{aligned} \quad (2.19)$$

Firstly, we take a two-dimensional Fourier transform of $I(x,y)$ over space x and y. Then, in the k_x and k_y domain, one selects the oscillating term in the upper $k_y$domain which corresponds to the first term in Equation (2.19), and then Inverse Fourier transform it back into x and y domain, to yield an envelope term $E_{unk}(x,y){E_{ref}}^*(x,y)$. Afterwards, since the reference field $E_{ref}(x,y)$ is previously measured and known (so is its conjugate), we can yield the complex unknown spatial field $E_{unk}(x,y)$.

Likewise, for ultrashort pulses with considerable bandwidths, spectrally-resolved digital holography has been applied to achieve the spatiospectral (or equivalently spatiotemporal) field of light [68, 69]. Specifically, to obtain the full spatiospectral information, holograms $I(x,y,\omega)$ are recorded between the unknown pulse field $E_{unk}(x,y,\omega)$ and a known reference pulse field $E_{ref}(x,y,\omega)$ at multiple different frequencies. Then, for each hologram (off-axis holography at angle θ), the unknown spatiospectral field $E_{unk}(x,y,\omega_i)$ at a particular frequency ω_i is encoded in the integrated intensity $I(x,y,\omega_i)$ by

$$\begin{aligned} I(x,y,\omega_i) &= |E_{unk}(x,y,\omega_i)|^2 + \left|E_{ref}(x,y,\omega_i)\right|^2 \\ &+E_{unk}(x,y,\omega_i){E_{ref}}^*(x,y,\omega_i)\exp\left(+i\tfrac{y\omega_i}{c}\sin(\theta)\right) \\ &+{E_{unk}}^*(x,y,\omega_i)E_{ref}(x,y,\omega_i)\exp(-i\tfrac{y\omega_i}{c}\sin(\theta)) \end{aligned} \quad (2.20)$$

where the oscillating term $E_{unk}(x,y,\omega_i){E_{ref}}^*(x,y,\omega_i)\exp\left(+i\frac{y\omega_i}{c}\sin(\theta)\right)$ can be extracted by a Fourier filtering [67] similar as described before, where the unknown field $E_{unk}(x,y,\omega_i)$ can be obtained with the knowledge of reference field $E_{ref}(x,y,\omega_i)$ [55]. By applying the same procedures for multiple digital holograms at different frequencies, the spatiospectral information of the unknown pulse $E_{unk}(x,y,\omega)$ can be obtained.

Afterwards, the spatiotemporal field $E_{unk}(x, y, t)$ can be calculated by inverse Fourier transform:

$$E_{unk}(x, y, t) = \frac{1}{2\pi}\int_{-\infty}^{+\infty} E_{unk}(x, y, \omega)\exp(i\omega t)d\omega$$

$$\approx \frac{1}{2\pi}\sum_i E_{unk}(x, y, \omega_i)\exp(i\omega_i t)\,\delta\omega. \quad (2.21)$$

In experiment, to determine the reference pulse field $E_{ref}(x, y, \omega)$, part of the laser beam can be sent through a spatial filter and then characterized by a FROG device, such as a GRENOUILLE [29, 30]. Using part of the same laser beam helps guarantee that the spectrum of reference pulse is coherent with and contains the spectrum of unknown pulse, so all frequency components can be measured. The spatial filter eliminates high spatial-frequency components in the beam, yielding a spatially smooth output pulse, for which the temporal profile can be easily measured by FROG. As a result, the reference pulse field can be completely determined over space and time (or frequency). And, the reference field at frequency ω_i can have the form $E_{ref}(x, y, \omega_i) = E_{ref}(x, y)\big|_{\omega_i} E_{ref}(\omega_i)$ and can be considered STC-free.

CHAPTER 3

PULSE CHARACTERIZATION TECHNIQUE STRIPED FISH

This chapter presents the apparatus, retrieval algorithm, preliminary proof-of-principle pulse measurements, previous device limitations, and the improved equipment of STRIPED FISH, used to measure spatiotemporal information of ultrashort pulses. Also, in order to intuitively display and calculate the field spatiotemporal properties, a spectrogram-based plotting method and pulse propagation method based on diffraction integral are discussed for STRIPED FISH measured results.

3.1 STRIPED FISH Fundamentals

As stated in the previous chapter, spectrally-resolved digital holography can be used to measure ultrashort pulses. The unknown field $E_{unk}(x, y, \omega)$ information is recorded among multiple two-dimensional holograms. By using digital cameras with small pixel size and high pixel count, it is possible to illuminate different regions of the imaging sensor with digital holograms at different frequencies. So, instead of wavelength scanning [68-70], a simple single-shot device is possible to measure the pulse spatiotemporal profile [54]. In this section, principles of operation are discussed for such a device, named STRIPED FISH (Spatially and Temporally Resolved Intensity and Phase Evaluation Device: Full Information from a Single Hologram).

3.1.1 Apparatus

STRIPED FISH apparatus is shown in the Figure 3.1. It comprises a very simple

setup of only a coarse two-dimensional diffractive optical element (DOE), an interference band-pass filter (IBPF), imaging optics and a camera. It uses a previously spatially smoothed and temporally characterized reference pulse, accomplished at an earlier point with a spatial filter and a FROG measurement. The pulse to be measured and the known reference pulse cross at a small vertical angle on the DOE, which simultaneously generates multiple pairs of beams, divergent at different angles. The DOE is also slightly rotated, so each beam pair has a different horizontal propagation angle. Because for a certain polarization the IBPF's transmission wavelength varies with incidence angle (for p-polarized laser, it primarily depends on horizontal angle), the IBPF then wavelength-filters each beam pair into different wavelengths. The beam pairs overlap on the camera, generating an array of quasi-monochromatic holograms, each at a different wavelength. As stated in the previous chapter, the spatiotemporal information of unknown pulse is contained within these holograms, which can be recorded on a single camera frame.

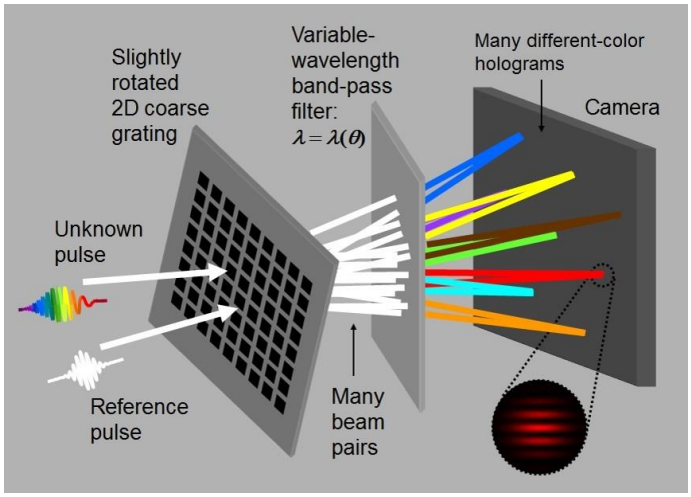

Figure 3.1. The conceptual schematic of STRIPED FISH apparatus. In reality, we also need imaging optics (not shown) to get all holograms onto the small camera chip. A simple known reference pulse is obtained before by spatial filtering and FROG measurement. The reference pulse and the spatiotemporally unknown pulse are combined into STRIPED FISH and finally interfere on the camera frame by crossing at a small vertical angle, to yield multiple holograms at different frequencies.

3.1.2 Retrieving Pulse from STRIPED FISH Trace

In the recorded camera frame (the "STRIPED FISH trace"), for each hologram on the camera, a Fourier filtering algorithm (as described before) can be applied, to obtain the unknown field $E_{unk}(x, y, \omega)$ at that particular frequency. Once the fields at all frequencies are obtained, an inverse Fourier transform over frequency can convert the spatiospectral unknown field $E_{unk}(x, y, \omega)$ into spatiotemporal domain expression $E_{unk}(x, y, t)$. The detailed retrieval process is illustrated in Figure 3.2.

In fact, the STRIPED FISH trace itself is quite informative. As the reference pulse is simple and contains no spatiotemporal coupling information (the STC is eliminated by spatial filtering), the spatiospectral information $E_{unk}(x, y, \omega)$ of the unknown pulse is encoded in STRIPED FISH traces. Therefore, it is possible to identify unknown pulse field structures by directly inspecting the recorded STRIPED FISH trace. We will discuss more details in Chapter 4.

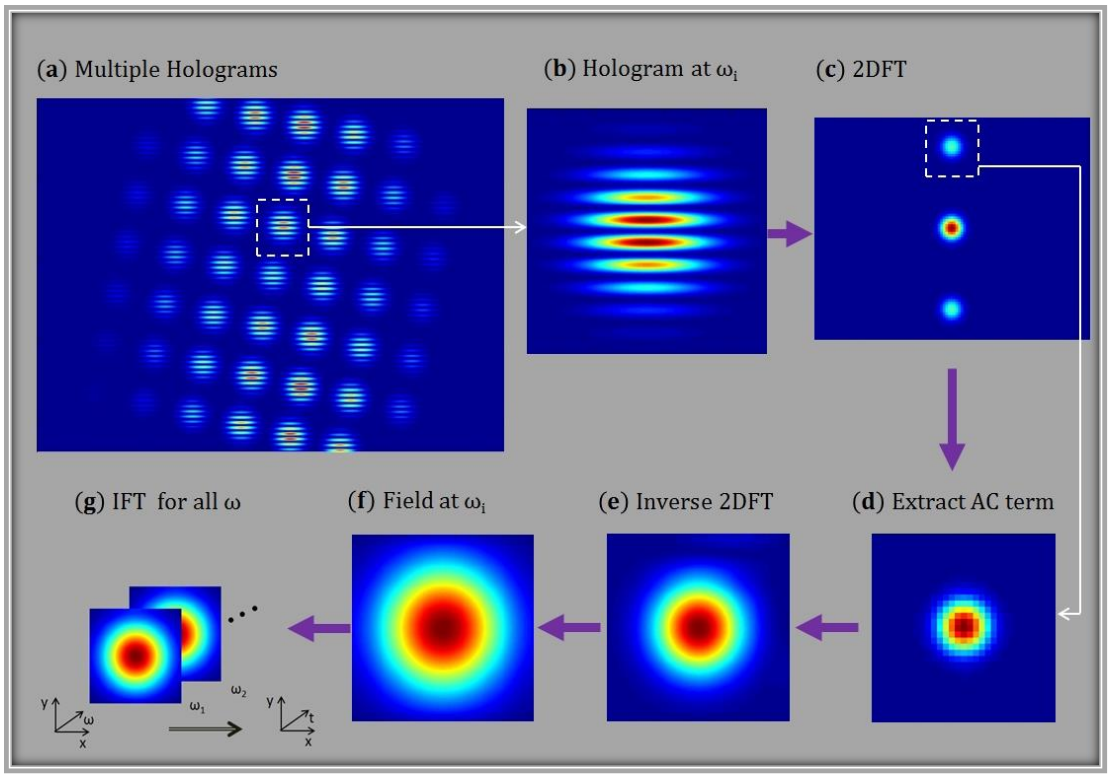

Figure 3.2. Illustration of the STRIPED FISH retrieval algorithm. Amplitudes are plotted for complex quantities. (a) Multiple holograms of different frequencies are recorded on the camera, yielding the intensity function $I(x, y, \omega_i)$ for each hologram. (b) Hologram at a certain frequency ω_i is selected. (c) The two dimensional Fourier transform (2DFT) of $I(x, y, \omega_i)$ is taken over spatial dimensions x and y. (d) The oscillating alternating-current (AC) term is extracted. (e) Inverse 2DFT of the extracted term into spatial domain (x, y), obtaining a product envelope term $E_{unk}(x, y, \omega_i)E_{ref}{}^*(x, y, \omega_i)$. (f) Dividing the reference field conjugate $E_{ref}{}^*(x, y, \omega_i)$ to obtain the unknown spatial field at ω_i, $E_{unk}(x, y, \omega_i)$. (g) Performing (a)-(f) for every hologram yields $E_{unk}(x, y, \omega)$, then $E_{unk}(x, y, t)$ by an inverse Fourier transform (IFT) into spatiotemporal domain.

3.2 Proof-of-principle Spatiotemporal Measurements

Previously, STRIPED FISH has been demonstrated to measure simple spatiotemporal structures in ultrashort pulses, such as temporal delay and temporal chirp. As an example, we show the measurement of a pulse with spatial chirp by Gabolde et al. [56]. As in Figure 3.3, the measured pulse intensity is plotted over $x - t$ in (a) and $y - t$ in (b). The height and brightness of the peak in plot scale with the pulse intensity, and the plotted color represents instantaneous wavelength. From the figures, it is clear that the

pulse shows a frequency chirp along x direction, and essentially no frequency chirp along y direction.

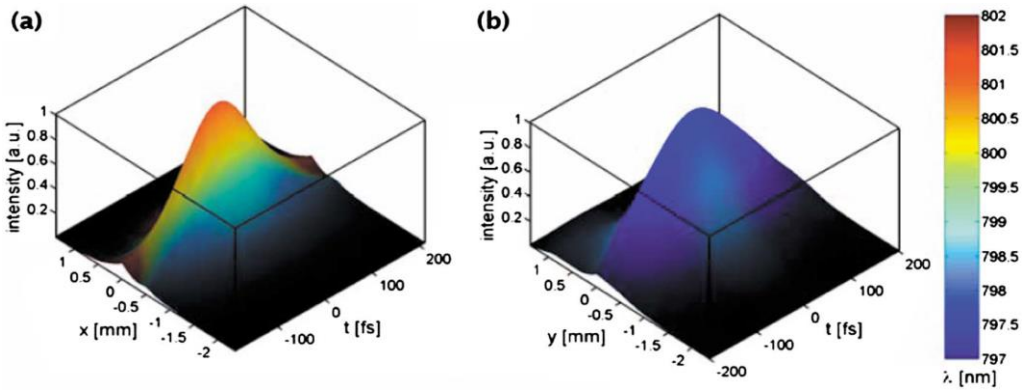

Figure 3.3. STRIPED FISH measurement of a spatially chirped pulse. (a) Measured intensity and wavelength over x and t. (b) Measured intensity and wavelength over y and t. Plots are from Ref. [56]. In both plots, the height and brightness scale with the pulse intensity and color represents instantaneous wavelength.

In addition to this type of space-time plot, from STRIPED FISH measurement, it is possible to plot a movie based on the instantaneous frequency from the retrieved spatiotemporal field $E_{unk}(x, y, t)$, to display the measured intensity and phase variations over x, y, and t. In such movie, the brightness will scale with pulse intensity, and color will be representing the instantaneous frequency value. Our group had tried this movie with previous measurements, but it showed severe drawbacks. To make STRIPED FISH a better candidate to monitor, measure and display pulses, we need to first be clear about its limitations and remedy them.

3.3 Improved STRIPED FISH Device

3.3.1 Limitations

In its initial demonstration [56], STRIPED FISH successfully measured simple

pulses with temporal chirp and spatial chirp. But, as with any new device, the initial implementation had limitations.

Spectral range: The transmitted central wavelength of an IBPF depends approximately linearly (when the angle range is small) on the beam incidence angle. As a result, a STRIPED FISH device's spectral range is limited by the range of beam angles impinging on the IBPF, which itself is limited by the range of angles generated by the DOE. In order to increase the device spectral range, for a given IBPF, a smaller feature size of the DOE, thus larger range of beam angles emerging from it, is required.

Aberrations: When the pairs of beams emerging from the DOE diverge more, severe aberrations (such as pincushion distortion and coma) arise due to the off-axis propagation through optics.

Order inequality: The various holograms had inherently highly unequal intensities (low diffractive orders were more intense) due to the order-dependent diffraction efficiency from the DOE. When the beam was attenuated enough that the central holograms did not saturate the camera, the peripheral holograms were very dim and had a low signal-to-noise ratio.

Very bright central zero-order artifact: The useful holograms were accompanied by a strong and useless central artifact, which overwhelmed adjacent holograms. This zero-order central-spike artifact [56] was due to the reflection from substrate of the DOE, which consisted of mostly transparent regions with small, square reflective coatings. An attempt to eliminate this artifact involved operating in reflection at Brewster's incidence of the substrate. It effectively removed the central-spike artifact, but it also, unfortunately, introduced a weak "ghost" reflection from the back surface of the substrate

[56]. Moreover, operating the subsequent imaging system at such an oblique angle (Brewster's angle) was vulnerable to off-axis misalignment and suffered from astigmatism.

Display method for the measured pulse: Finally, even the seemingly simple task of plotting the measured pulse proved quite challenging, due to the inherent data volume of both the intensity and phase over x, y, and t (i.e., two four-dimensional graphs). Previously, to show the time evolution, we either suppressed a dimension, or made movies by plotting the intensity and instantaneous frequency as a function of x and y and time (slowed). While these movies displayed simple chirped pulses well, the instantaneous frequency can, in practice, be highly unnatural in appearance: white regions of pulses (where all frequencies are present) are displayed as green—a fundamental plotting artifact of instantaneous-frequency based method.

3.3.2 Improvements

To address the problems, improvements are made. Firstly, we have converted to a normal incidence "negative DOE", whose transmission function is equal to the reflection function of the previous DOE. Therefore, this new grating has the same diffraction pattern in transmission, as before in reflection. But, as it works in a transmission manner, it has a no zero-order central-spike artifact or "ghost" reflection.

Secondly, we added an apodizing neutral density filter (ANDF), placed near the focal plane of the first lens (see Figure 3.4(a)). Its radially decreasing optical density significantly attenuates central beams (low diffraction orders) relative to peripheral ones (high orders). As a result, it better balances the intensities of the various diffracted orders,

effect as observed from Figure 3.4(b) and 3.4(d).

Thirdly, to collect the highly divergent beams and direct them to the camera without aberrations, we added an imaging system comprising two highly aberration-corrected commercial photographic lenses. Such lenses are designed for large incidence angles, as are common in photography. These lenses successfully image the divergent beams with minimal aberrations, allowing a greater range of angles at the IBPF and therefore a larger wavelength range (see Figure 3.4(c) and 3.4(d)). Although these multi-element lenses contain significant amounts of glass, they can be used in our ultrafast-optical device because the resulting group-delay dispersion is experienced by both the unknown and reference pulses and cancels out of the holographic measurement.

With these improvements, up to 40 holograms could be imaged onto a 10.5mm×7.73mm camera chip with negligible aberrations. It increased the spectral range and also allowed the device to use the full dynamic range of the camera (8 bits, 0 - 255) with a reasonable signal-to-noise ratio.

As a side note, although we use the holograms to obtain the intensity and phase of the pulse here, also note that, if the reference beam is absent and only the unknown beam is incident, STRIPED FISH behaves exactly as a single-frame 3D imaging spectrometer (see Figure 3.4(a)), yielding at the camera the spatially dependent spectrum $I(x, y, \omega)$. This may be of interest for spectroscopic applications [71, 72].

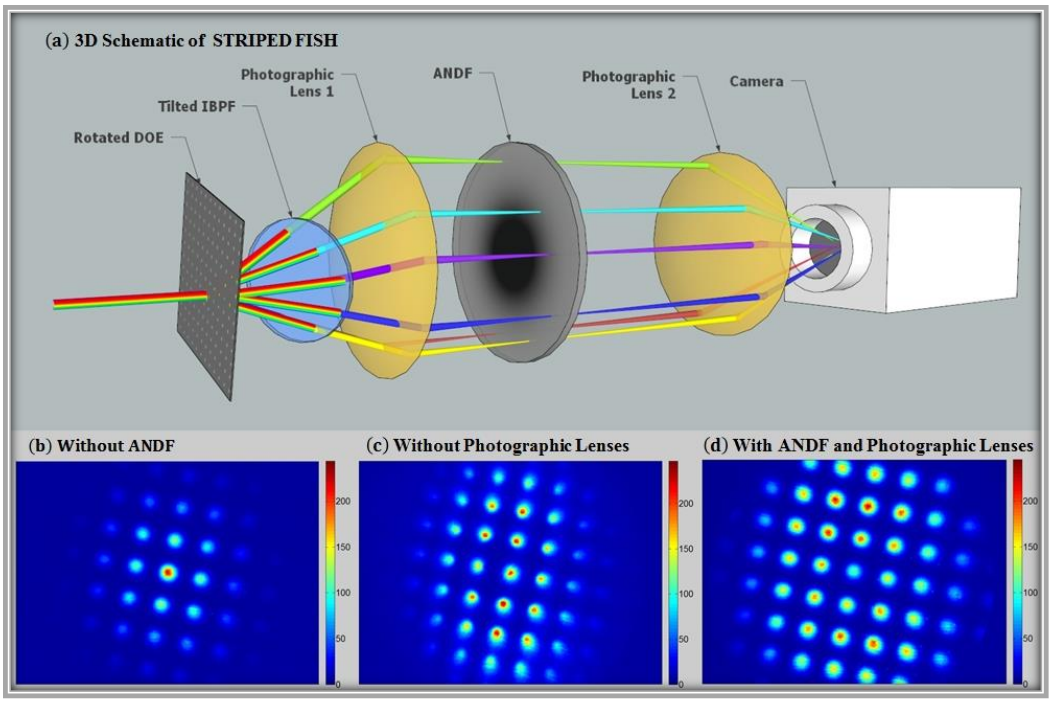

Figure 3.4. The improved STRIPED FISH apparatus and camera shots, showing the effect of the ANDF and photographic lenses, when only one beam is incident. (a) 3D schematic of the STRIPED FISH apparatus. The input broadband beam is split into multiple quasi-monochromatic beams and then imaged onto the camera. (b) Camera shot without the ANDF. Note that, due to the diffraction efficiencies and pulse spectrum, the central spot appears much brighter than the peripheral ones (27.3 times difference in peak intensity). (c) Camera shot imaged by using two simple convex lenses. Note the aberrations introduced by the diverging beams. Most obvious aberrations are barrel distortion and coma. (d) Camera shot after applying the ANDF and photographic lenses. Note the increased peripheral visibility (5.7 times peak intensity difference) and suppressed aberrations, resulting in a good signal-to-noise ratio for a wider range of wavelengths.

To more intuitively display the measured intensity and phase over x, y, and t, we no longer use the instantaneous frequency and now instead compute numerical spectrograms of the retrieved pulse $E_{unk}(x, y, t)$ at each point in space using a variably delayed numerically-generated gate pulse (a fraction of a pulse length long). The expression for these spectrograms is:

$$Sp(x, y, T, \omega) = \left| \int_{-\infty}^{\infty} E_{unk}(x, y, t) \mathrm{g}(t - T) \exp(-\mathrm{i}\omega t)\, dt \right|^2 \qquad (3.1)$$

where $g(t - T)$ is the numerical gate function with variable delay T.

We then compute overlap integrals of each spectrogram with red, green, and blue response functions. For the red color,

$$R(x,y,T) = \int_{-\infty}^{\infty} Sp(x,y,T,\omega)R(\omega)d\omega \qquad (3.2)$$

where $R(\omega)$ is the red response function. This function is a simple Gaussian centered at a red frequency if true color is desired. If false color is desired, then this function is centered on the redder wavelengths of the pulse spectrum. Similar response functions are used to compute the green (or center for false color) and blue (or bluer) overlap integrals. The resulting color functions then serve as RGB values (vs. x, y and t), ensuring that a pixel appears white at places and times when the whole spectrum is present, and red/blue biased when longer/shorter wavelengths dominate. In other words, color saturation in this method shows the pulse spectral bandwidth information. Also, we normalize the total color contents, so that the brightness (weight of color) represents the relative intensity (vs. x, y and t). Since the color of the pixels represents phase, both the intensity and phase information is contained in the RGB functions. This allows us to generate color movies as the human eye would perceive the pulse if the eye actually had the temporal resolution to do so.

As examples of this plotting method, we show several pulses of simulation, plotted using the spectrogram-based color movies. First we show the distortion case of cubic spectral phase. Cubic spectral phase is often observed in pulse compression when the quadratic spectral phase has been compensated out. It can play a significant role in pulse shaping and pulse amplification, as it is a usual cause of satellite pulses in time. The pulse implemented in simulation has 70fs duration and $5 \times 10^4 fs^3$ cubic spectral phase, and zero quadratic spectral phase.

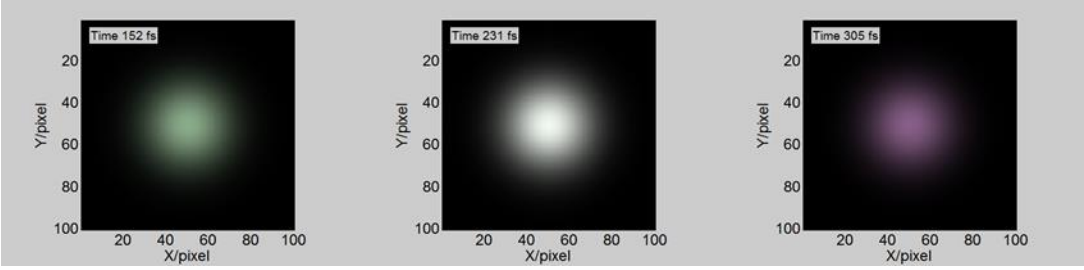

Figure 3.5. Pulse movie of cubic spectral phase. Pulse in simulation has 70fs duration, zero spectral phase, and a cubic spectral phase of $5 \times 10^4 fs^3$. In the movie (Media 3.1.avi, 161KB), the pulse first shows green, then white, finally purple in time.

As shown in Figure 3.5, as time goes on, the pulse first appears green, then white in the middle of time, and then turns purple. This is because, for such cubic spectral phase, the green frequency component of the pulse travels faster than the blue and red components. When the RGB colors balance in time, they together show the white color. And when red and blue dominate, the pulse shows purple as the superposition. On the other hand, the instantaneous frequency value of the pulse is constant at all time, so the instantaneous-frequency-based movie would always be green in this case, which omits important spectral phase information.

A second case is a commonly used STC, the pulse-front tilt. In Figure 3.6, we show the movie of a pulse with pulse-front tilt (40fs/mm) and zero temporal/spectral chirp. As expected, because of no chirp, the pulse does not change color over time. The pulse-front tilt is shown by consecutive arrival time of the white pulse over x. As the frequency component of the pulse contains all the spectrum and is unchanged over time, the current movie is always white. However, the instantaneous-frequency plot would be green, which is counter-intuitive.

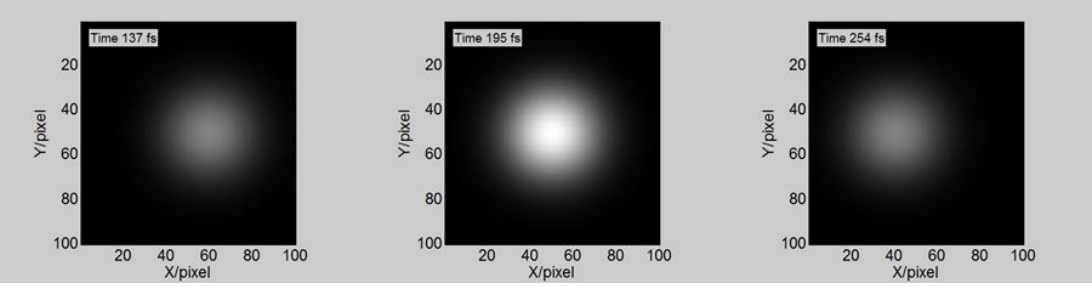

Figure 3.6. Simulation of pulse with pulse-front tilt (40fs/mm) and zero temporal/spectral chirp. The pulse movie (Media 3.2.avi, 160KB) shows horizontal position shift with respect to arrival time, and is always in white color.

A third case is on another STC that is often investigated, the spatial chirp. We have implemented a pulse with 21fs/mm spatial chirp, and no temporal/spectral chirp. The movie of the pulse is in Figure 3.7. As observed, the pulse appears reddish on the left and blueish on the right. In the middle, where the pulse RGB contents overlap, the pulse looks white. Note that the pulse shape remains similar at all time, because of no temporal/spectral chirp. This movie shows the effect of spatially-dependent frequency components, as well as the pulse bandwidth information, therefore a proper display for spatial chirp.

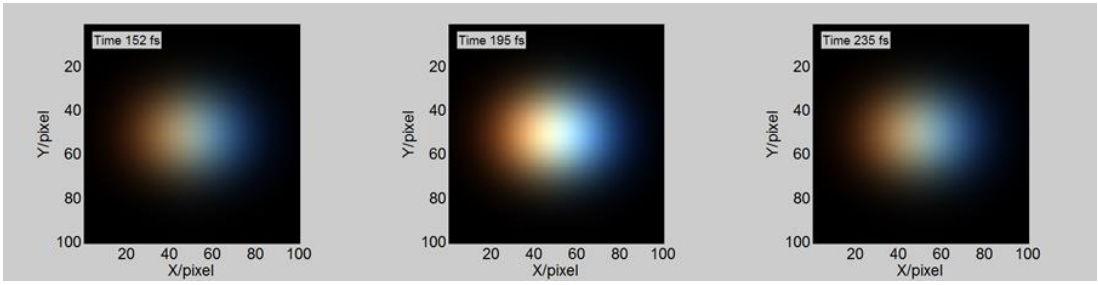

Figure 3.7. Simulation of a pulse with spatial chirp (21fs/mm) and zero temporal/spectral chirp. In the movie (Movie 3.3.avi, 164KB), the pulse shows red-biased color on left and blue-biased color on right. When the RGB color contents overlap in the middle, the pulse appears white. This way the pulse frequency bias and bandwidth information are both well displayed.

Note that the magnetic field can be completely determined from the electric field,

to further display the light field over space (x, y, z) and time (t), we need to determine the z-dependence of the field by calculating diffraction integrals. From the measured field $E(x, y, t)$ at a particular z-plane, we can propagate or back-propagate the field onto any other z-planes of interest, and get the volumetric information on the measured field. Using the spectrogram-based plotting, over space and time, the brightness indicates the pulse's intensity and color represents the pulse's phase variation. Like above, plotting a movie to display the field evolution is a good choice. In Chapter 7, we will show our method to propagate and plot the pulse with ultrafast lighthouse effect, as an experimental example for complete spatiotemporal measurement.

CHAPTER 4

STRIPED FISH TRACE CATALOG

This chapter describes the investigation of STRIPED FISH trace properties obtained on camera frame, featured in the spatiospectral domain. Typical spatiotemporal structures are studied by modifying the Gaussian pulse fields in respective domains (e.g. spatiotemporal domain, or spatiospectral domain) by using the first-order Gaussian coupling theory introduced before. Ultrashort pulses with 70fs duration, wavelength ranging from 775nm to 825 nm were simulated. The Fourier-transform related terms which represent pulse-field amplitude or phase couplings are also analyzed on their spatial and spectral effects on STRIPED FISH trace. By inspection of experimentally recorded traces and comparison with the simulated ones, one may monitor the unknown pulse field properties even before the retrieval algorithm has been carried out. Finally a numerical simulation on spatially chirped pulses with wave-front curvature was analyzed on its features and confirmed with experimental recordings.

To understand the effects of various spatiotemporal distortions on STRIPED FISH traces, we numerically investigate STRIPED FISH trace features for a catalog of pulses, including the spatially and temporally transform-limited pulse, temporal and spatial double pulses, spherically focusing and diverging pulses, self-phase modulated and self-focusing pulses, spatiotemporally coupled pulses and pulses with complex structures. Overall, we find that, from STRIPED FISH's informative trace, significant spatiotemporal characteristics of the unknown pulse can be immediately recognized from the camera frame. This, coupled with its simple pulse-retrieval algorithm, make

STRIPED FISH an excellent technique for measuring and monitoring ultrafast laser sources.

4.1 Assumptions and Discussions

To intuitively show the effects of STCs on the STRIPED FISH trace, we have made a few assumptions for our numerical simulations. First, we assume that, if only the STC-free reference pulse is recorded by STRIPED FISH (that is, when the unknown pulse is blocked), all of the diffraction orders in the STRIEPD FISH trace would have the same intensity, as shown in Figure 4.1(a). This effectively means that the trace is normalized to the spectrum of the reference pulse. Under this assumption, if an unknown pulse with the same spectrum is measured, all the holograms will still show the same peak intensity. Experimentally, the imaging optics and apodizing filter attempt to make this a reality [55]. Even if the intensities of all diffracted orders are not ideally equal, one can always numerically normalize the recorded values afterwards. By making this assumption, however, the intensity variation effects brought up by the spatiotemporal structures of the unknown pulse on the STRIPED FISH trace can be clearly shown. In each STRIPED FISH trace we assume 25 holograms, forming a 5×5 matrix, each with a different monochromatic wavelength evenly ranging over 25nm, with the central wavelength λ_0 being 800nm.

As a STRIPED FISH trace is generated by spatially interfering an unknown pulse with a reference pulse at each frequency, the trace itself reveals the spatiospectral characteristics of the unknown pulse. As summarized in Table 4.1, the unknown pulse spatial structure is contained within each hologram: the spatial intensity is represented by

the intensity distribution and the spatial phase is indicated by the fringe shape within one hologram. Likewise, the spectral information is reflected by multiple holograms: the spectral intensity is represented by the intensity variations and the spectral phase is indicated by the fringe shifts among different holograms. When STC exists in the unknown pulse, the STRIPED FISH trace shows correlations between these spatial and spectral effects, which we will investigate later specifically.

Table 4.1. The spatial and spectral effects of the unknown pulse on STRIPED FISH traces.

Spatial	Amplitude	Intensity distribution within one hologram
	Phase	Fringe shape within one hologram
Spectral	Amplitude	Intensity among multiple holograms
	Phase	Fringe shift among multiple holograms

4.2 Pulse Trace Simulations

4.2.1 Transform-limited Pulse

First we investigate the simplest case when the unknown pulse is a transform-limited Gaussian pulse in both space and time. The expression for such spatiotemporal field is:

$$E(x,y,t) = E(x,y)E(t) = \exp(-ax^2 - by^2) \times \exp(-ct^2) \qquad (4.1)$$

where the parameters a, b, and c are related to the pulse's intensity FWHM spatial widths Δx, Δy and temporal width Δt by $\Delta x = \sqrt{\frac{2\ln(2)}{a}}$, $\Delta y = \sqrt{\frac{2\ln(2)}{b}}$ and $\Delta t = \sqrt{\frac{2\ln(2)}{c}}$. And note that we omit the optical carrier-frequency term for all electric fields. We also omit the

subscript indicating the unknown field, as all fields henceforth will refer to the unknown field (to be measured).

Fourier transform over t of the above equation gives us the spatiospectral field:

$$E(x,y,\omega) = E(x,y)E(\omega) = \sqrt{\frac{\pi}{c}}\exp(-ax^2 - by^2) \times \exp(-\frac{\omega^2}{4c}) \qquad (4.2)$$

In this case, a, b and c are all defined to be real quantities (1mm^{-2}, 1mm^{-2} and 2.04×10^{-4} fs^{-2} =1/(70fs)^2; $\Delta x = 1.18mm$, $\Delta y = 1.18mm$ and $\Delta t = 82.4fs$), so the pulse is collimated and transform-limited, with no temporal chirp or STC. To emphasize the effects of the unknown pulse, we use the above assumptions to plot the simulated traces. A spatiospectral-intensity trace of the transform-limited pulse is plotted in Figure 4.1(a), which is also the camera trace when no reference pulse is incident. Figure 4.2(b) shows the equal-intensity STRIPED FISH holograms. In the pictures, color denotes the wavelength and brightness denotes the intensity.

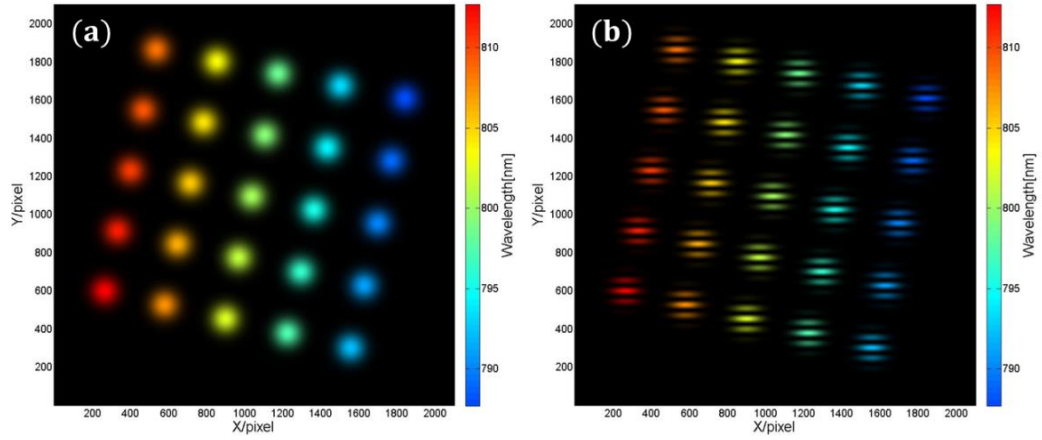

Figure 4.1. Spatiospectral-intensity trace (without reference pulse) and STRIPED FISH trace (with reference pulse), for a Gaussian-shaped transform-limited pulse in space and time. Note that the holograms have equal intensities at all wavelengths, indicated by their brightness and colors. The x and y axes are in 10μm pixel increments. (a) Spatiospectral-intensity trace. (b) The STRIPED FISH holograms.

4.2.2 Temporal and Spatial Double Pulses

To better illustrate the effects in Table 4.1, we now simulate the cases of collinear temporal double pulses and synchronized spatial double pulses. The STRIPED FISH traces are shown in Figure 4.2.

The temporal double pulses, each of which is transform-limited, share the same intensity. One pulse is delayed by τ (136fs) from the other, with a π phase jump in between. To show the spectral-phase variation, we set their arrival time to be t_0 (209fs), so that they have a linearly varying spectral phase. The expression for the unknown pulse field is:

$$E(x,y,t) = \exp(-ax^2 - by^2)\exp[-\mathrm{c}(t+t_0)^2]$$
$$+\exp(i\pi)\exp(-ax^2 - by^2)\exp[-\mathrm{c}(t+t_0+\tau)^2] \qquad (4.3)$$

From Figure 4.2(a), we can see the variation in the spectral intensity of the double pulse. And from Figure 4.2(b), we can clearly see the corresponding spectral intensity variations among the different-color holograms. Also, the fringe positions vary from hologram to hologram in Figure 4.2(b) (compared with Figure 4.1(b)), indicating that the spectral phase of the unknown pulse changes with frequency.

Similarly, we demonstrate the spatial effects in STRIPED FISH traces by simulating a pair of synchronized and spatially separated pulses. Two beams are assumed to propagate in the same direction, the left of which has half of the amplitude (and therefore a quarter of the intensity) of the right one. To show the spatial phase variation, we incorporate a π phase jump between the two component pulses. The expression is:

$$E(x,y,t) = \exp[-a'(x-x_0)^2 - b'y^2]\exp(-ct^2)$$
$$+0.5\times\exp(i\pi)\exp[-a'(x+x_0)^2 - b'y^2]\exp(-ct^2) \qquad (4.4)$$

where $a' = b' = 2.04mm^{-2}$, and $x_0 = 0.7mm$. Figures 4.2(c) and 4.2(d) show that the

left pulse is dimmer than the right one. Also, in the middle of each hologram in Figure 4.2(d), we can clearly observe a fringe discontinuity due to the spatial phase jump.

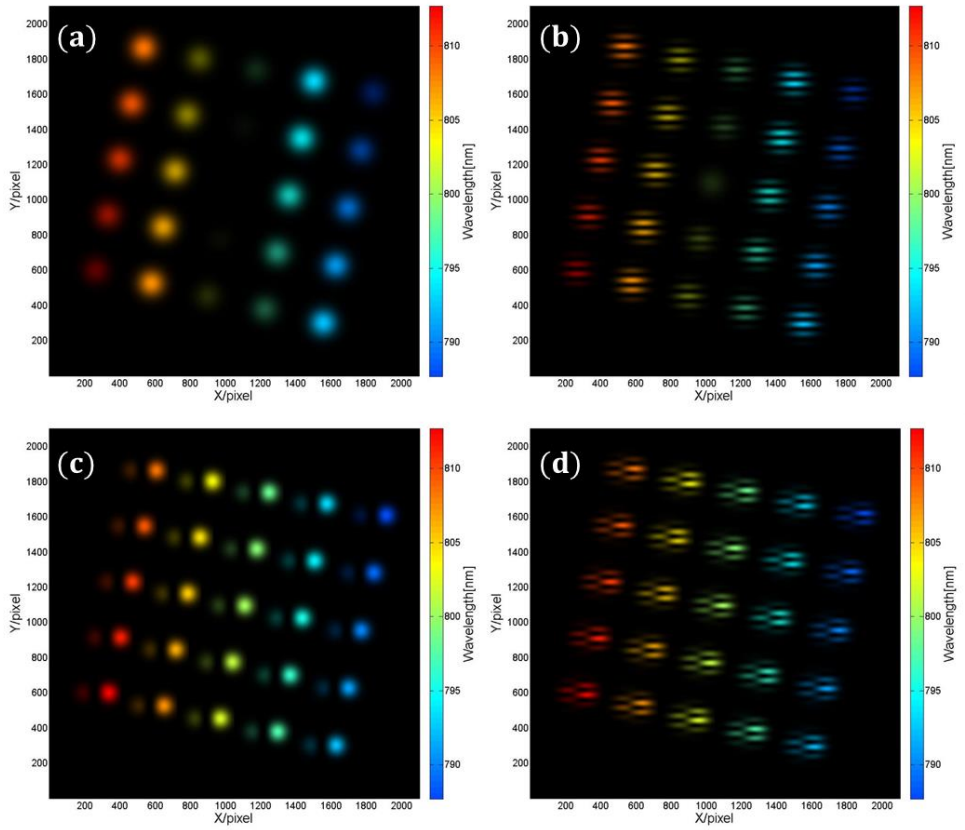

Figure 4.2. Spatiospectral-intensity traces (without reference pulses) and STRIPED FISH traces (with reference pulses) for double pulses. (a) Spatiospectral-intensity trace of a temporal double pulse with equal-intensity individual pulses and a π phase jump between them. (b) The STRIPED FISH trace of the temporal double pulse in (a). (c) Spatiospectral-intensity trace of a spatial double pulse, with the left pulse of one fourth the intensity of the right pulse. A π phase jump occurs between the two pulses. (d) The STRIPED FISH trace of the spatial double pulses shown in (c).

4.2.3 Spherically Focusing or Diverging Pulses

Another interesting case is the focusing or diverging pulse. Focusing or diverging pulses, respectively, correspond to a spatial quadratic phase function with radius $R < 0$ or $R > 0$. Note that in our simulations, the unknown pulse propagates on axis and the

reference pulse crosses it from above. The field expression for a pulse with radius of curvature R is:

$$E(x, y, \omega) = exp\left(-ax^2 - by^2 - \frac{\omega^2}{4c} - \frac{i\omega}{2cR}(x^2 + y^2)\right) \tag{4.5}$$

As shown in Figure 4.3, the curvature of the interference fringes indicates the wave-front curvature of the unknown pulse. The rings are not concentric because the unknown and reference beams also cross at a small vertical angle θ. The smaller value the focusing radius R is, the more tightly the pulse is focused, the more curved the fringes will be (see Figure 4.3(b)). In the opposite R case, when the pulse is diverging, the hologram fringes will be a vertically-flipped version of Figures 4.3(a) and 4.3(b) (thus not shown).

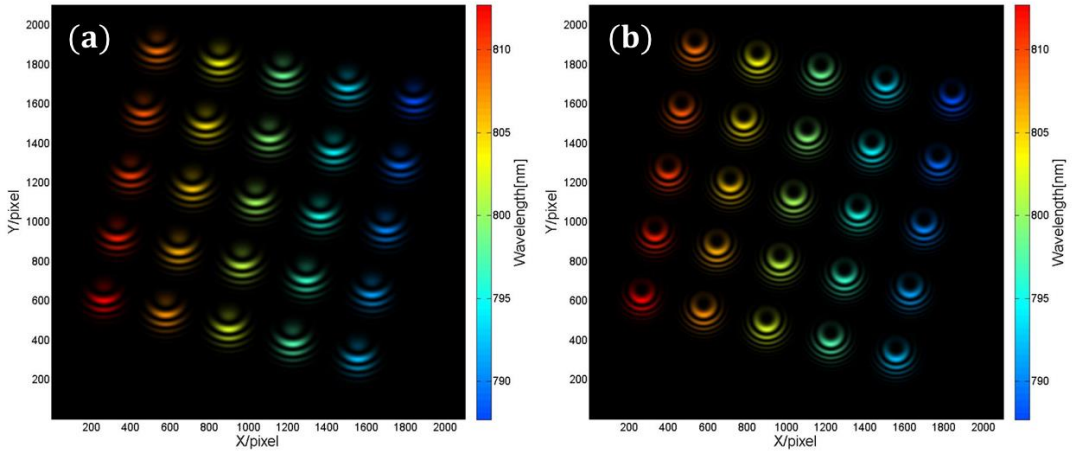

Figure 4.3. STRIPED FISH traces for focusing pulses. (a) The STRIPED FISH holograms for a loosely focusing pulse, with R = -816mm. (b) The STRIPED FISH holograms for a tightly focusing pulse, with R = -408mm.

4.2.4 Self-Phase Modulated and Self-Focused Pulse

Next, to investigate pulses with modifications in both the spatial and spectral profiles, we look at a pulse with one typical nonlinear-optical effect, the intensity-

dependent phase. When an intense pulse passes through an optical-Kerr medium [73], self-phase modulation (SPM) can be observed in time domain. The spatial counterpart, the self-focusing (SF), can also happen for ultrashort pulses with sufficient energy in their propagation through bulk solids, liquids and gases [1]. Such a pulse with SPM and SF has an approximate expression:

$$E(x, y, t) = \exp(-ax^2 - by^2 - ct^2)\exp(-in_2 I) \tag{4.6}$$

where the intensity term $I = |\exp(-ax^2 - by^2 - ct^2)|^2$. Note that, for simulation purposes, we have used normalized field amplitude and (therefore) intensity, with dimensionless and unity peak values. Also, we use a numerical index n_2 to characterize the amount of introduced phase modulation. The resulting spatiospectral and STRIPED FISH traces are shown in Figure 4.4, for 1.5 radians peak phase modulation. Note that the spectral intensity in the picture is dimmer in the middle orders than the side ones. This shows a spectral-broadening effect caused by SPM: due to intensity-dependent temporal phase, the pulse energy has been redistributed toward the edges of the spectrum, so central spectrum appears dimmer after normalization. The slight fringe curvature inside each hologram in Figure 4.4(b) indicates the spatial self-focusing, and effect is more evident again in side orders than the middle ones, as a result of the intensity-dependent phase modulation.

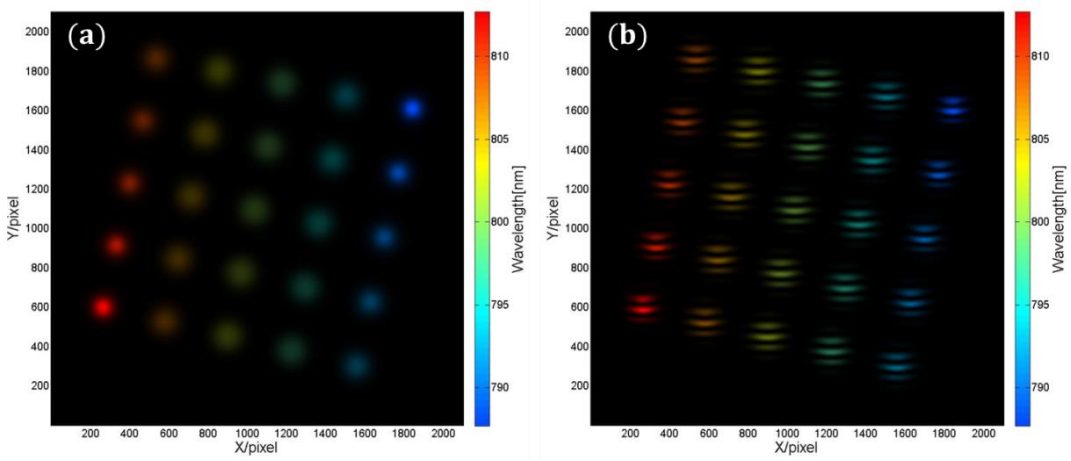

Figure 4.4. Spatiospectral-intensity trace (without reference pulse) and STRIPED FISH trace (with reference pulse) for the pulse with SPM and SF ($n_2 = 1.5$). (a) Spatiospectral intensity of the unknown pulse. The intensity is normalized so the brightness shows the relevant intensities. Note that the bluest and reddest orders have the highest intensity due to SPM. (b) The STRIPED FISH holograms. Note the SF effect is indicated by the curvature of fringes in each hologram, which is the most evident on side orders.

4.2.5 Spatiotemporally Coupled Pulses

Now we discuss the effects of first-order STCs on STRIPED FISH traces. To begin with, because the STRIPED FISH trace comprises holograms in the spatiospectral domain, we first look at spatial chirp (SPC) and wave-front tilt dispersion (WFD), which correspond to the real and imaginary STC terms in the spatiospectral field [66]. The effect of SPC along x and y directions are similar, therefore we only show the SPC along x in Figure 4.5. The corresponding expression is:

$$E(x, y, \omega) = \exp(-ax^2 - by^2)\ \exp(2x\omega\mathrm{SPC})\ \exp\left(-\frac{\omega^2}{4\times(-i\mathrm{TCP}+c)}\right) \qquad (4.7)$$

where a, b and c are defined as before, SPC and TCP are the spatial chirp and temporal chirp (14 fs/mm and 1×10^{-4} fs^{-2} respectively). As expected, the spatial chirp causes holograms of different frequencies to shift linearly in space with their corresponding frequencies.

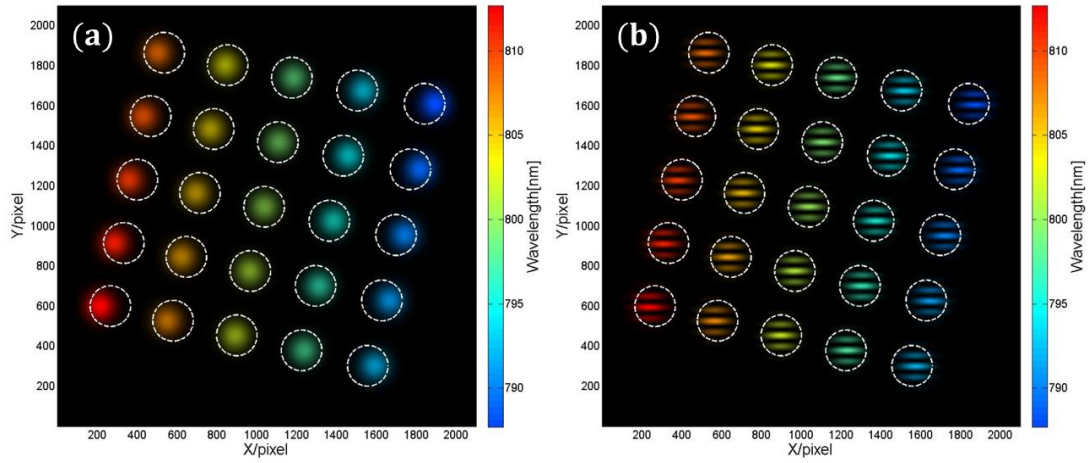

Figure 4.5. Spatiospectral-intensity trace (without reference pulse) and STRIPED FISH trace (with reference pulse) for the spatially chirped pulse. The white circular contours indicate the central positions of the holograms in the transform-limited case (no SPC) or effectively the central positions of the reference pulse. (a) Spatiospectral-intensity of the pulse with SPC along x direction. (b) The STRIPED FISH holograms.

Shown in Figures 4.6(a) and 4.6(b) are traces for WFD (-35 fs/mm) along x and y, respectively. Only STRIPED FISH traces (holograms) are plotted, because WFD is a phase term not visible in the unknown pulse spatiospectral intensity. Thus, the center positions of the holograms are not shifted. The WFD along x causes the fringes to rotate, changing their orientations; however, the WFD along the y direction causes the spacing between fringes to vary, decreasing monotonically from red to blue. Note also that, for collimated beams, WFD is related to angular dispersion (AGD) [66]. The expressions for the WFD pulses are as below:

$$E(x,y,\omega) = \exp(-ax^2 - by^2)\exp(2ix\omega\ \mathrm{WFD})\exp(-\frac{\omega^2}{4\times(-i\mathrm{TCP}+c)}) \qquad (4.8)$$

$$E(x,y,\omega) = \exp(-ax^2 - by^2)\exp(2iy\omega\ \mathrm{WFD})\ \exp(-\frac{\omega^2}{4\times(-i\mathrm{TCP}+c)}) \qquad (4.9)$$

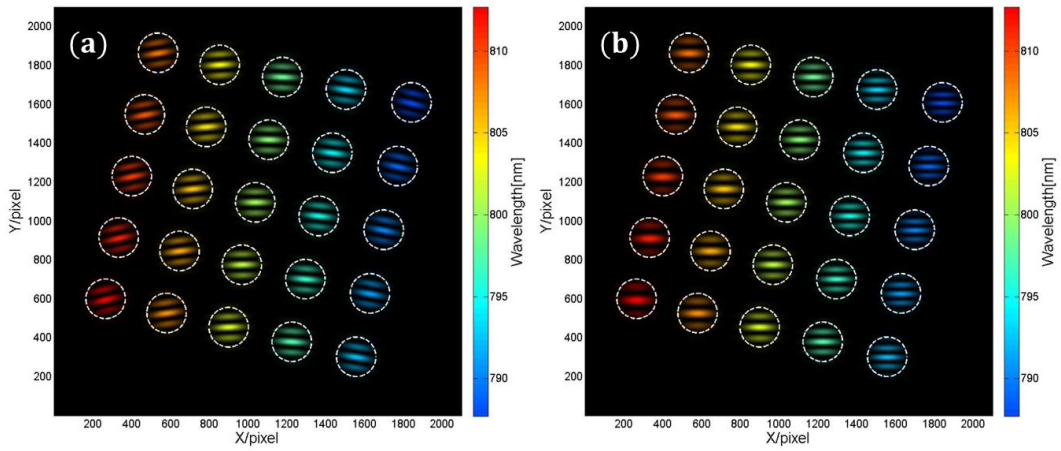

Figure 4.6. STRIPED FISH traces for the wave-front-tilt-dispersed pulse. The white circular contours indicate the central positions of the transform-limited case (no WFD). (a) STRIPED FISH holograms of a pulse with WFD along x. (b) STRIPED FISH holograms of a pulse with WFD along y.

Now, we note that, to first order, all STCs in all four domains (temporal, spectral, spatial and spatial frequency domains) are interrelated by Fourier transforms [66]. Given the beam parameters and STC terms in one particular domain, the STC values in all other FT-related domains can be uniquely determined. In our case, as the STRIPED FISH trace exists in the spatiospectral (x, ω) domain, the parameters that can sufficiently define the pulse are: beam spot size, wave-front curvature, bandwidth and frequency chirp, and the coupling terms SPC and WFD. Therefore, from another perspective, the presence of STCs in other FT-related domains (spatiotemporal (x, t), spatial-frequency-temporal (k, t), and spatial-frequency-spectral domains (k, ω)) will be visible in the spatiospectral domain, and thus be recorded by the STRIPED FISH trace. As an example, we investigate a common STC, pulse-front tilt (PFT). The traces of PFT (50fs/mm, normalized by the pulse width) along x and y are shown in Figure 4.7(a) and 4.7(b), respectively. Specifically, their expressions are:

$$E(x, y, t) = \exp(-ax^2 - by^2)\exp(2xt\text{PFT})\exp(-ct^2 + i\text{TCP}t^2) \qquad (4.10)$$

$$E(x, y, t) = \exp(-ax^2 - by^2)\exp(2yt\text{PFT})\exp(-ct^2 + i\text{TCP}t^2) \quad (4.11)$$

Applied along the x direction, the effect of PFT shows the combination of the two "fundamental" effects of SPC and WFD above. That is, central positions of holograms shift and their fringe orientations vary with frequency. Likewise, when applied along y, PFT shifts the central y positions of holograms and also varies the fringe spacing. This is in accordance with the discussions in Ref. [74]: PFT can result from AGD or simultaneous SPC and TCP.

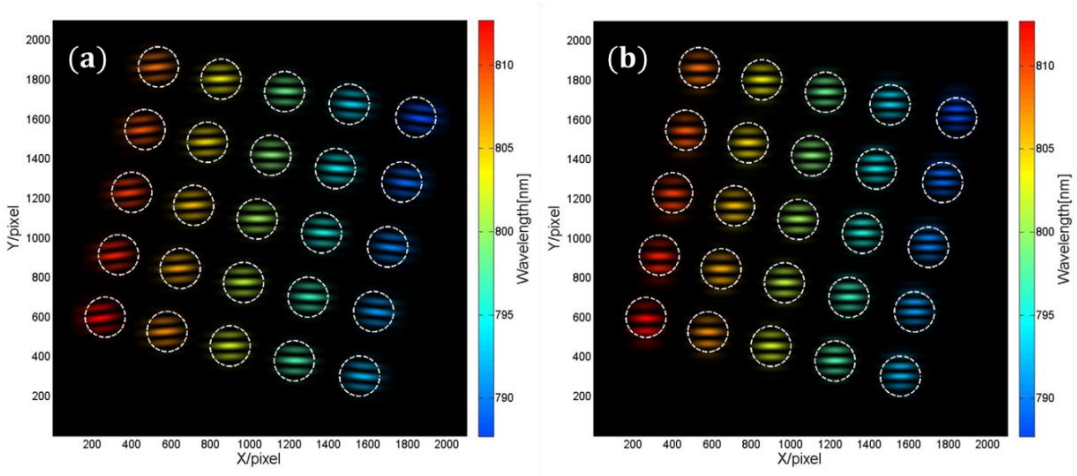

Figure 4.7. STRIPED FISH traces for pulse-front tilted pulses. (a) The STRIPED FISH holograms of a pulse with PFT along x. (b) The STRIPED FISH holograms of a pulse with PFT along y.

4.3 Simultaneous Cases: Focusing Pulses with STCs

Lenses or focusing mirrors are often used to focus pulses with STCs. For instance, in the typical pulse-shaping geometry, focusing lenses are used to convert angular dispersion to spatial chirp; after passing through the spatial light modulator, the beam propagates through a reverse geometry to undo the effects of the earlier optics [75, 76]. So, we now investigate the STRIPED FISH traces for focusing STCs. We use the same values as before for STCs, and $R = -1632mm$ for pulse focusing. Figures 4.8(a) and

4.8(b) show the STRIPED FISH traces for focusing SPC, along x and y directions respectively. Due to the SPC, central positions of the holograms shift with frequencies. Also, the fringes are curved, indicating that the unknown pulse is focusing. Note that in Figure 4.8(a), the fringe orientations have seemingly rotated, due to visual artifacts caused by the horizontally shifted intensities. In Figures 4.8(c) and 4.8(d), STRIPED FISH traces for focusing pulses with WFD along x or y are shown. Central positions of these holograms are not shifted. The fringes, either changing their orientations or spacing with respect to frequency, all present curved patterns, which indicates the curved wave front.

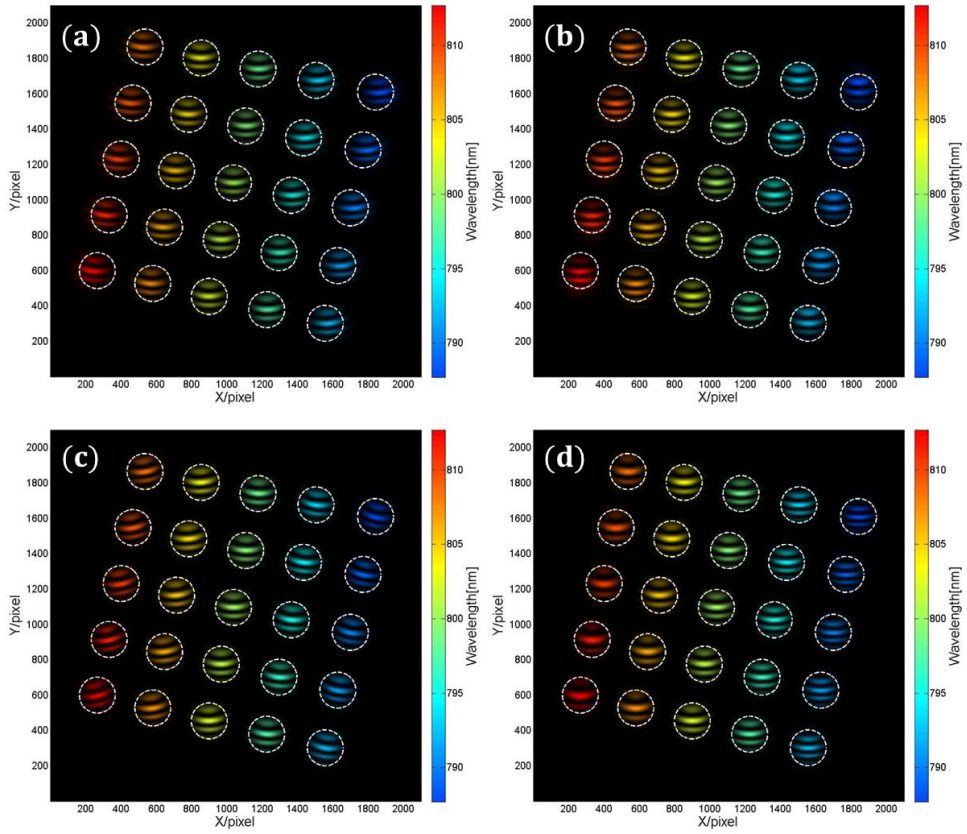

Figure 4.8. STRIPED FISH traces for a focusing pulse with STCs. (a) The STRIPED FISH holograms of a focusing pulse with SPC along x. The rotation of fringe orientations is due to the shifting of the central position of the unknown pulse. (b) The STRIPED FISH holograms of a focusing pulse with SPC along y. (c) The STRIPED FISH holograms of a focusing pulse with WFD along x. (d) The STRIPED FISH holograms of a focusing pulse with WFD along y.

4.4 Pulses with Complex Structures

To show an example of complex intensity and phase variations, we incorporate a pulse with hypothetical third-order distortions in the spatiospectral domain. The resulted STRIPED FISH trace in Figure 4.9 shows the complexity of the pulse, clearly different from any pulse investigated above. The mathematical expression of the unknown pulse is:

$$E(x, y, \omega) = \exp(-ay^2 - bx^2 + iC_0\omega(x^2 + y^2)\ )\ \exp(-\frac{\omega^2}{4c}) \qquad (4.12)$$

where a, b, c and C_0 are defined to be 1mm^{-2}, 4mm^{-2}, 2.04×10^{-4} fs^{-2} and 0.1 respectively. Although complicated, the hologram structures can still be analyzed following the rules stated before. In Figure 4.9, both the spatiospectral intensity trace and the STRIPED FISH hologram trace show beam patterns with a wider span in y than in x direction, indicating different beam widths. Although the spatiospectral intensity trace shows the same pattern for all wavelengths (which indicates an identical spectral intensity profile as the Fourier-transform limited reference pulse), the STRIPED FISH holograms show fringes that vary from order to order. The middle-frequency hologram (green) shows essentially no curvature, therefore is close to collimation. The low-frequency hologram (red) shows downward curvature which corresponds to a diverging wave front, and the high-frequency (blue) a focusing wave front. So mainly, the quadratic spatial phase depends on frequency, which is a (at least) third-order phase effect. The center positions of the holograms are not shifted and their fringe orientations are not tilted, indicating no SPC or WFD along x. However, it is hard to tell if the unknown pulse contains WFD along y from the trace.

In this manner, a measured STRIPED FISH trace can be interpreted for the unknown pulse's spatiospectral information. Of course, as the STRIPED FISH trace contains the complete information about the unknown pulse, we can run the full retrieval algorithm to yield values for arbitrarily high order terms (over x, y and t or ω) by polynomial fitting the resulting field.

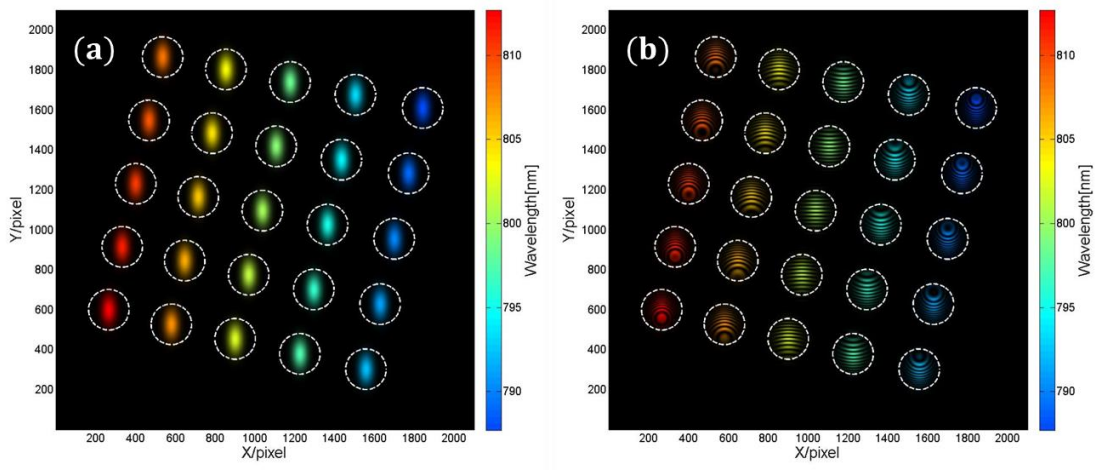

Figure 4.9. Spatiospectral-intensity trace (without reference pulse) and STRIPED FISH trace (with reference pulse) of a pulse with hypothetical third-order distortions. Note that the fringes are distorted in an unprecedented manner. (a) Spatiospectral-intensity of the unknown pulse. (b) The STRIPED FISH holograms.

4.5 Experimental Example

We now demonstrate an example of experimentally recorded STRIPED FISH trace. The trace is associated with a focusing pulse with SPC along x. Such a pulse profile is introduced by a prism pair and followed by a focusing lens. In the STRIPED FISH trace (Figure 4.10), we can see the STC effects. The intensity of the holograms is fairly even across the trace, suggesting no evident modifications to the reference spectrum. Curved and nearly circular fringes mean that the pulse presents a focusing quadratic spatial phase. Central positions of holograms have small hologram-dependent

shifting, and therefore the fringes show slight rotations from the left side to the right side. This agrees with our introduction of spatial chirp into the beam. Thus, the experimental trace matches our expectations from the experimental setup. Moreover, we have performed numerical simulations for the trace, based on the parameters obtained from the experiment, which show also good agreement.

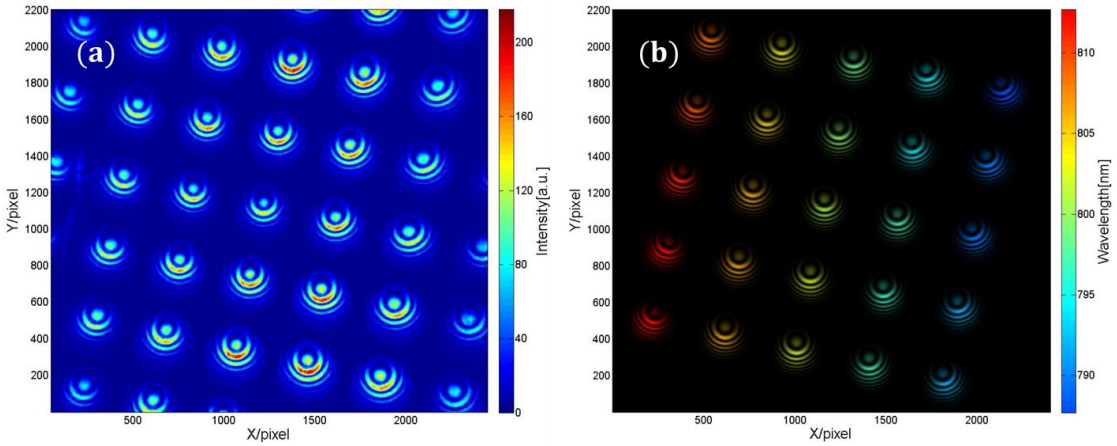

Figure 4.10. STRIPED FISH trace experiment example. (a) Recorded STRIPED FISH holograms for a focusing pulse with SPC along x. The color scale indicates intensity on the camera. (b) Simulated STRIPED FISH holograms. The color scale indicates wavelengths recorded from experiment.

4.6 Summary

With its simple and compact apparatus, STRIPED FISH is a convenient single-shot technique for measuring the complete spatiotemporal field of pulses. Its spatiospectral experimental trace, a set of holograms generated at various frequencies by spatially crossing the reference beam with the unknown beam, is highly informative and need to be understood. Though a robust pulse-retrieval algorithm can easily extract the complete field information from the STRIPED FISH trace, one can gain much insight immediately about the unknown pulse profile simply by visual inspecting the STRIPED

FISH trace on the camera. The STRIPED FISH trace contains (for each frequency) the spatial information of the unknown pulse in one particular hologram, and it records (for each location) the spectral profiles of the unknown pulse among multiple holograms. To help determine the spatiotemporal profile of the unknown pulse, we have simulated STRIPED FISH traces for typical pulse species, where considerably different holographic traces are analyzed in details. We also show hypothetical and experimental pulse traces to demonstrate what to look for if the pulse contains spatiotemporal complexity. Because the STRIPED FISH trace can be inspected in real time, STRIPED FISH can thus be very useful for measuring or monitoring spatiotemporal profiles of ultrashort pulses.

CHAPTER 5

COMPLETE SPATIOTEMPORAL MEASUREMENT OF CHIRPED PULSE BEATING PHENOMENON

In this chapter, we demonstrate the measurement power of the improved STRIPED FISH apparatus by making single camera frame measurements of spatiotemporally complex sub-picosecond pulses—a phenomenon called chirped pulse beating. The beating structures formed by the crossed and chirped pulses from a Ti:Sapphire oscillator can be captured and intuitively displayed by STRIPED FISH.

5.1 Experimental Setup

To demonstrate spatiotemporal measurements, we performed experiment using the improved STRIPED FISH device. We used a high-rep-rate Ti:Sapphire oscillator as the laser source, so our measurements were not single-shot. But we used single camera frames, to yield a proof of principle that true single-shot measurement is possible. As shown in Figure 5.1, the output pulse from a Ti:Sapphire oscillator (KMLabs, 800nm center wavelength, 20nm in FWHM) propagated through a pulse compressor (Swamp Optics BOA Compressor), and then traveled through a spatial filter made of two convex lenses (first 300mm, second 100mm) and a pinhole (PH, 75μm). A flip mirror (FP) was then used to switch the beam path into GRENOUILLE (Swamp Optics, model 8-50). When the flip mirror was out of the beam, the beam propagated into two sets of beam-splitters (BS) that divided it into three replicas. One acted as the reference pulse, and the other two were combined at different angles with varying amounts of chirp and delay,

creating a double-pulse with chirped-pulse beating that varied with spatial position. Two delay stages were used to synchronize the two unknown pulses and the reference. These three beams were combined into STRIPED FISH.

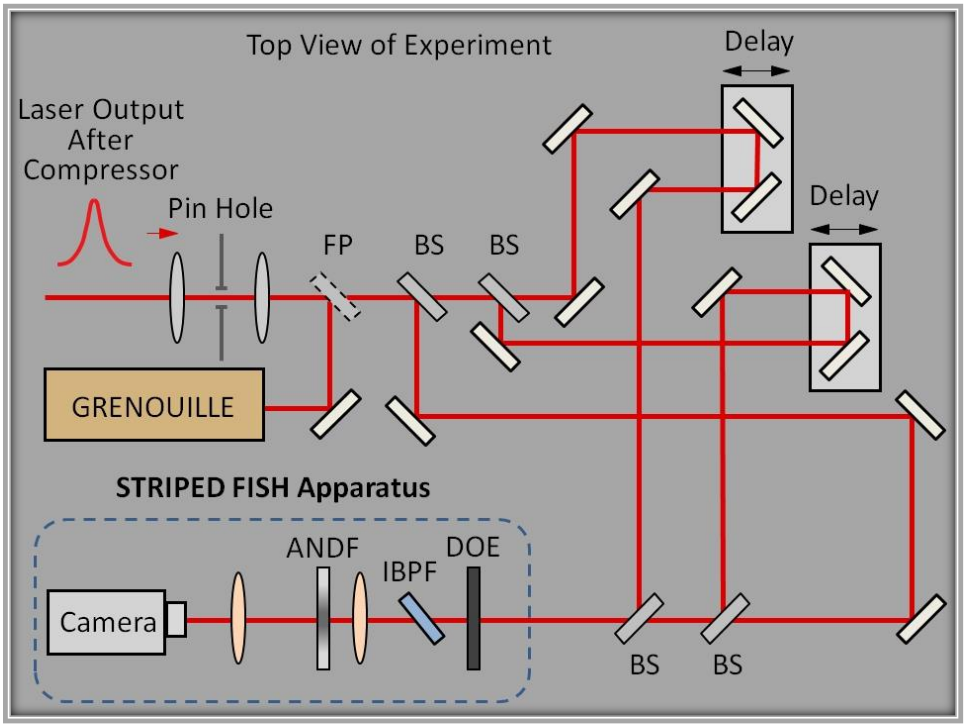

Figure 5.1. Top view of the current experiment for generating and measuring a complex unknown pulse consisting of two crossed, delayed, and chirped pulses. Chirp was controlled by the pulse compressor. A flip mirror (FP) was used to switch the beam to the GRENOUILLE. Three beam splitters (BS) provided the reference and double pulse to be measured. The STRIPED FISH device is shown within the dashed blue frame.

In the STRIPED FISH device, the coarse DOE was made by photo-masking a soda lime substrate with a dark-field chrome coating, which comprised an array of transparent square windows (3μm×3μm, 15μm spacing) that diffracted the beams into highly divergent (~30°) beam arrays. The DOE was rotated slightly (~10°) in the vertical plane to ensure that different beam replicas propagated at different horizontal angles. Then the beams were spectrally resolved by an IBPF (Semrock LL01-852, 3.2nm bandwidth, tilted by ~40°), with their center wavelength determined by their incidence

angle. In this way, the whole spectrum of interest (~775 to ~825nm) could be measured, with all frequencies calibrated by a fiber-coupled spectrometer (Ocean Optics HR4000). The imaging system consisted of two photographic lenses (lens 1: Computar c-mount 50mm, f1.8; lens 2: Computar c-mount 75mm, f1.4) and an ANDF (Edmund Optics 64386). After the imaging system, the unknown double pulses interfered with the reference pulses on the camera screen (PixeLINK PL-A781, 3000×2208 pixels, 3.5μm pixel pitch), forming ~40 quasi-monochromatic (~5nm bandwidth) holograms at different frequencies.

5.2 Results and Simulations

Using the above setup, we measured spatiotemporally complex pulses consisting of double pulses crossed at various angles and with varying amounts of delay and chirp. Figure 5.2(a) shows the resulting camera frame containing the multiple holograms generated by interference of the unknown and reference beams at different frequencies. Figure 5.2(b) shows a camera image of only the unknown double pulse (with the reference beam blocked), yielding the spatial intensities for various frequencies $I_{unk}(x, y, \omega)$. Figure 5.2(c) and 5.2(d) show simulated camera frames, respectively for Figure 5.2(a) and 5.2(b), assuming Gaussian beams with the actual known beam-crossing angle, relative delay, pulse chirp, and spectral response parameters of camera. A comparison shows that the measured camera frames agree well with what is expected based on our knowledge of the electric field.

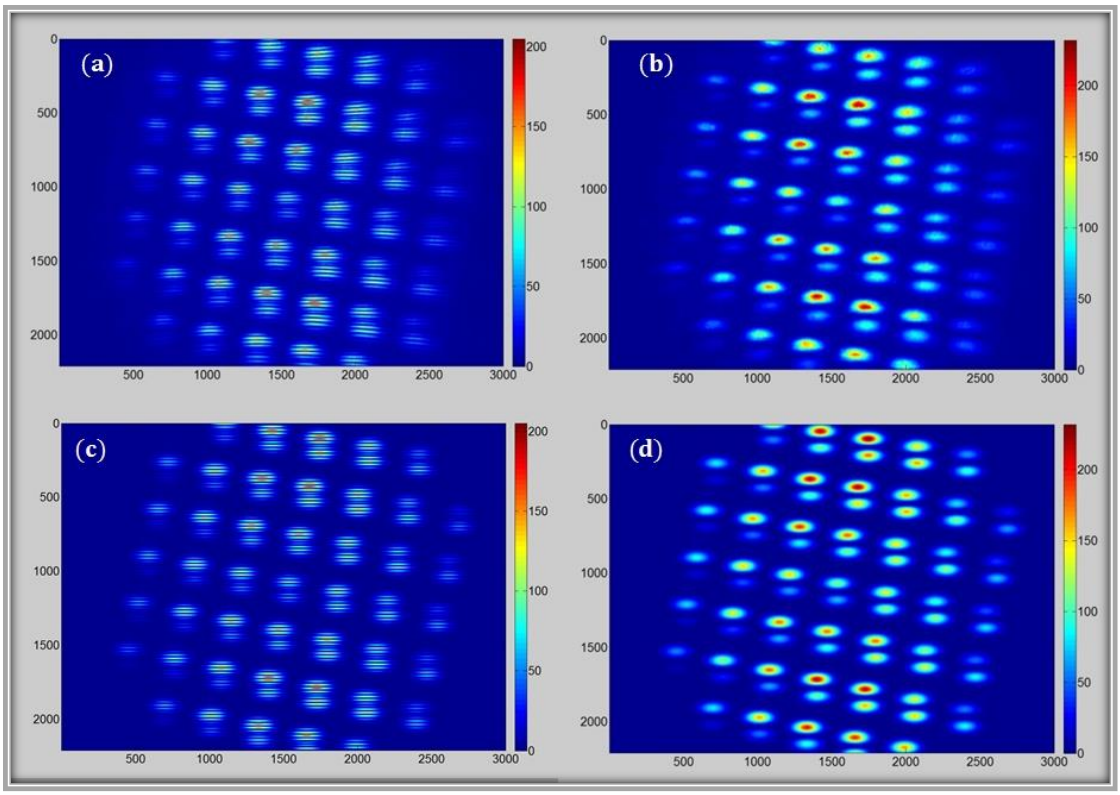

Figure 5.2. The STRIPED FISH traces and unknown pulse spectra for 28.9fs-spaced, 122.1fs-long positively chirped double pulses crossing at a small angle (~0.1º). x and y axes are in pixels. (a) Holograms created by interfering the reference and unknown double pulses on the camera screen. (b) Blocking the reference pulse yields the unknown pulse spatial profiles for each frequency, $I_{unk}(x, y, \omega)$. (c) Simulated STRIPED FISH trace. (d) Simulated unknown-pulse spatial profiles for each frequency, $I_{unk}(x, y, \omega)$.

For each measurement, we generated a false-color STRIPED-FISH-measured movie of $E_{unk}(x, y, t)$. The movie shows the spatially and temporally complex brightness and color patterns for the unknown crossing double pulses. Also, to ensure the credibility of our measured results, we have performed two crosschecks. The first check was a STRIPED FISH internal check: a STRIPED FISH measurement was performed for each individual pulse that made up the unknown double pulse, and then their retrieved electric fields were added numerically, using the known crossing angle and delay, to yield the unknown field. The double-pulse field (movie) obtained this way should be the same as

the direct measurement of both pulses at once. A second check was to perform a theoretical simulation of the STRIPED FISH trace assuming simple Gaussian pulse and beam shapes and their known crossing angles and delays. Again, the simulated movie is expected to have features similar to the directly measured one.

For demonstration, we first show the movies of crossing chirped pulses with zero relative delay. In this case, we expect the spatial fringes to be consistent with crossing pulses, and the color of pulse should only change with time. Figure 5.3 shows movies of positively chirped crossing pulses, and Figure 5.4 shows negatively chirped pulses.

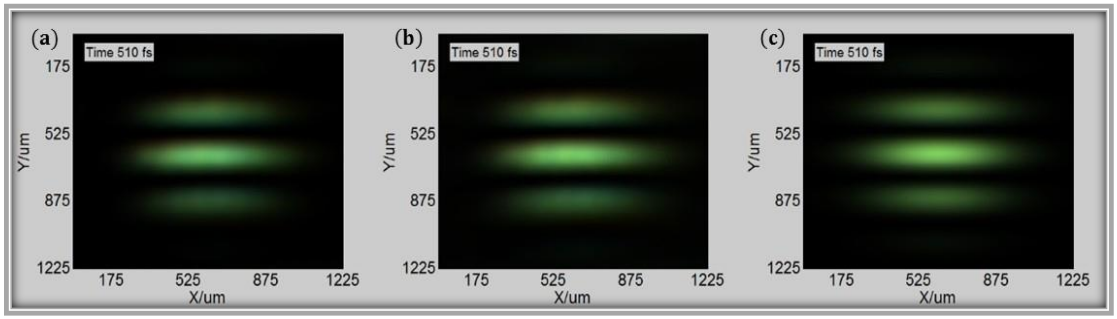

Figure 5.3. Movie shots of STRIPED FISH-measured double-pulses comprising two 122.1fs-long positively chirped pulses with a 2.3fs separation and crossing at a small angle (~0.1º). Relative time is shown in the upper left corner. (a) STRIPED FISH-measured result (Media 5.1.avi, 488KB). (b) Internal check result (Media 5.2.avi, 505KB). (c) Simulation result (Media 5.3.avi, 501KB).

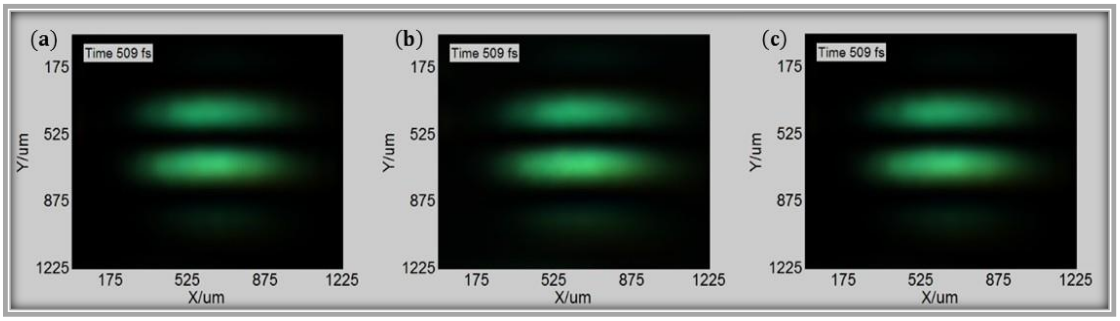

Figure 5.4. Movie shots of STRIPED FISH-measured double-pulses comprising two 122.7fs-long negatively chirped pulses with a 0.8fs separation and crossing at a small angle (~0.1º). Relative time is shown in the upper left corner. (a) STRIPED FISH-measured result (Media 5.4.avi, 505KB). (b) Internal check result (Media 5.5.avi, 518KB). (c) Simulation result (Media 5.6, 501KB).

Next, the relative delay between two pulses in the unknown double-pulse was adjusted from ~0fs to ~30fs by a high-precision motorized translation stage (Newport ESP UE16PP, 0.074μm resolution). As expected, adding a delay between the pulses causes chirped-pulse beating. Since the exact delay between the pulses varies with spatial position due to the crossing angle, different colors experience constructive interference at different positions. As a result, the fringes move and change colors with time in interesting ways. Figure 5.5 shows the movie results for positively chirped pulses, and Figure 5.6 shows the results for negatively chirped pulses.

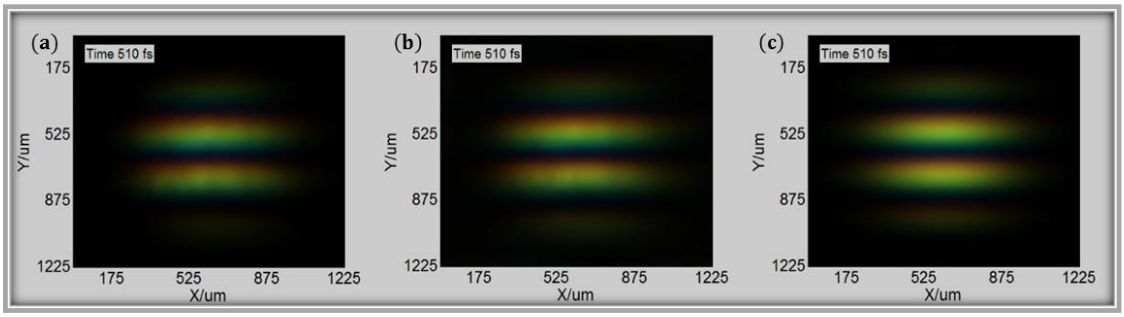

Figure 5.5. Movie shots of STRIPED FISH-measured double-pulses comprising two 122.1fs-long positively chirped pulses with a 39.6fs separation and crossing at a small angle (~0.1º). Relative time is shown in the upper left corner. (a) Measured result (Media 5.7.avi, 492KB). (b) Internal check result (Media 5.8.avi, 505KB). (c) Simulation result (Media 5.9.avi, 507KB).

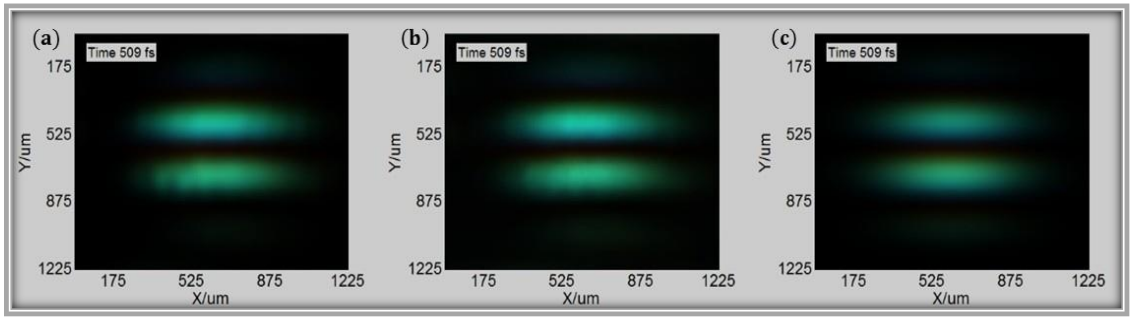

Figure 5.6. Movie shots of STRIPED FISH-measured double-pulses comprising two 122.7fs-long negatively chirped pulses with a 28.1fs separation and crossing at a small angle (~0.1º). Relative time is shown in the upper left corner. (a) Measured result (Media 5.10.avi, 508KB). (b) Internal check result (Media 5.11.avi, 522KB). (c) Simulation result (Media 5.12.avi, 504KB).

Then, in a second set of measurements, the angle between the pulses was decreased in order to vary the spatial interference pattern. Figure 5.7 shows the result for pulses that are essentially coincident in time. As expected, decreasing the angle between the beams results in an interference pattern with broader fringes. The transverse variation in delay between the beams is smaller, so, when a ~30fs delay is added between the pulses, the chirped-pulse-beating pattern varies more slowly as a function of position (see Figure 5.8).

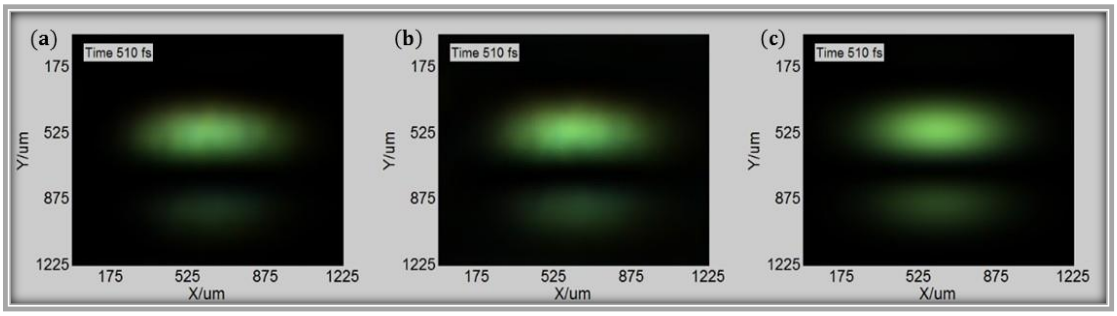

Figure 5.7. Movie shots of STRIPED FISH-measured interference between 2.3fs spaced, 122.1fs-long positively chirped double pulses crossing at a smaller angle. Relative time is shown in the upper left corner. (a) Measured result (Media 5.13.avi, 481KB). (b) Internal check result (Media 5.14.avi, 496KB). (c) Simulation result (Media 5.15.avi, 492KB).

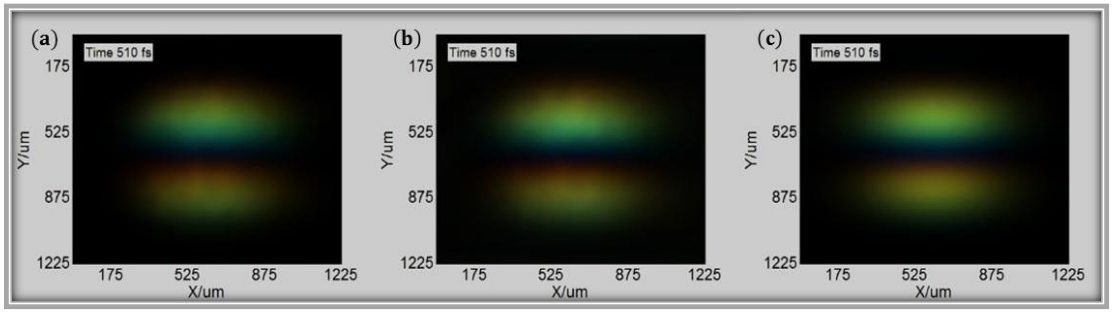

Figure 5.8. Movies of STRIPED FISH-measured interference between 28.9fs spaced, 122.1fs-long positively chirped double pulses crossing at a smaller angle. Relative time is shown in the upper left corner. (a) Measured result (Media 5.16.avi, 488KB). (b) Internal check result (Media 5.17.avi, 501KB). (c) Simulation result (Media 5.18.avi, 498KB).

5.3 Discussion

Our measured and simulated results show that STRIPED FISH can accurately measures pulses with complex spatiotemporal structures. For crossing pulses, STRIPED FISH was able to retrieve the intensity and phase correctly, even for the low-intensity regions between fringes. Megapixels of data were used for retrieval (350×350×35 pixels) from a single camera frame, together with the FROG measurement, ensuring relatively high resolutions in space and time (frequency). Nevertheless, not all details in the retrieved traces and movies achieved perfect agreement with the simulations. For example, there are some intensity discrepancies in the traces, and the simulated movies appear spatially smoother than the measured ones. Possible reasons for these discrepancies derive from the Gaussian profile used for the reference pulse and the finite filter bandwidth.

5.4 Summary

We demonstrated measurements using an improved STRIPED FISH device for sub-picosecond complex pulses. STRIPED FISH, as the first apparatus to yield complete spatiotemporal electric field in all three dimensions (x, y, and t) (z information is not needed, as it can then be obtained using the diffraction integral) for an ultrashort pulse on a single camera frame, should be able to measure complex pulses using its compact optics without complicated alignment or scanning issues typically experienced by other methods. The DOE, IBPF, and imaging optics work together to increase the spectral range by generating a larger divergence angle among the beams with negligible

aberrations. Also, as seen in the traces, the apodizing filter improved the intensity uniformity for the numerous holograms generated in the device. The intensity and phase behavior of crossing chirped double pulses are shown as examples, with various delays, chirps, and crossing angles. We performed cross-checks to test the retrieval robustness, which agreed well with our measured results.

CHAPTER 6

COMPLETE MEASUREMENT OF PULSES FROM MULTIMODE OPTICAL FIBERS

In this chapter, we demonstrate complete spatiotemporal field measurement of ultrafast pulses emerging from multimode optical fibers, using the simple non-scan STRIPED FISH pulse characterization. Again, pulse information can be obtained from holograms recorded on a single camera frame. Different modes in multimode fiber form a complex field to characterize, due to their different spatial fields, propagation velocities, and dispersions inside fibers. Using femtosecond pulses from a Ti:Sapphire laser near 800nm, we investigated the first few modes, LP_{01}, LP_{11}, LP_{02} and LP_{21} propagation in several different fibers. We measured from STRIPED FISH the entire spatiotemporal fields $E(x,y,t)$, or equivalently $E(x,y,\omega)$ by Fourier transform, and generated movies showing modal field structures over space, frequency and time.

6.1 Introduction: Spatiotemporal Field from Multimode Fibers

With recent developments in optical fiber technology, multimode fiber (MMF) has found many important applications. In optical communication, MMFs with larger core diameters have been used for mode-division multiplexing (MDM) to increase the number of data channels [77]. Data transmissions by the first few linearly-polarized (LP) modes have been reported [78] and terabit-scale rates are achievable with modes that conserve orbital angular momentum, both in free-space [79] and in optical fiber [80]. Sensors based on MMFs have been developed to measure refractive index, temperature,

strain, displacement and other physical properties. These sensors are attractive because of their high sensitivity, easy fabrication and low cost, which are typically constructed with transitional structures, such as singlemode-multimode-singlemode (SMS) [81]. As one type of disordered medium, MMFs have been used in waveform control [82], microendoscopic imaging [83] and biophotonics manipulation [84]. The large core areas of MMFs provide high damage thresholds of fibers, which is a usable advantage to scale up energy in laser amplification [85], pulse delivery [86], supercontinuum generation [87] and other nonlinear optical phenomena [88, 89]. All these applications operate best with a reliable knowledge of the optical field inside MMFs, but such measurements can be very difficult, especially for ultrashort pulses, as they are necessarily associated with large bandwidths and temporal complexity.

As we have discussed, characterization of ultrashort laser pulses has never been a trivial problem. Ultrashort pulses typically show field variations faster than the detection speed of electronics, so that they can only be characterized by nonlinear-optical methods. An accurate temporal pulse measurement method Frequency Resolved Optical Gating (FROG) [8] was developed for various pulse durations and wavelength ranges, but it requires a spatially uniform beam to operate with. However, many pulses of interest are not only spatially complex but also contain severe temporal or spectral field dependence on space (that is, possess spatiotemporal coupling). As in Figure 6.1, due to the multiple fiber modes in propagation, ultrashort laser pulses from MMFs necessarily contain complex spatiotemporal field structures. Specifically, different modal fields are, by definition, spatially distinct and they propagate at different velocities so to acquire a non-zero modal delay difference over certain length of fiber. Moreover, due to the possibly

large pulse bandwidths and the frequency dependence of both spatial fields and modal velocities, the dispersions of various fiber modes can also cause quite significant complexity. To characterize ultrashort pulses from MMFs, it is thus necessary to perform measurements of the complete spatiotemporal optical field, preferably with a simple, quick and compact solution.

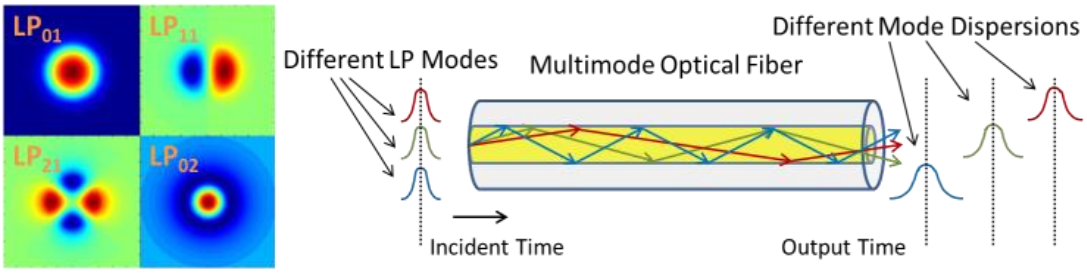

Figure 6.1. The spatial, temporal and frequency pulse field complexity due to various LP modes in propagation inside multimode optical fibers.

Over the years, many pulse-characterization techniques have been proposed to characterize output light fields emerging from MMFs. Some examples are spatially and spectrally resolved (S2) imaging [90], cross-correlation (C2) imaging [91], fast camera [87], and time-gated spatial heterodyne interferometry [92]. These methods extract some very useful information regarding the field, e.g. the multi-path interference. However, in operation they typically require a scanning stage to capture field signals over space, wavelength, or time, which requires high laser-source stability, opto-mechanical accuracy and considerable time to measure. Also, some methods only yield partial information about the complete spatiotemporal field and require assumptions regarding the modal content. Other methods, like computer generated holographic correlation filtering [93] and intensity profile based mode-decomposition analysis algorithm [94], have also been proposed to measure fiber emerging optical fields, but these field measurements can be

complex, require mode stability, and be adaptable only to a certain set of modes previously known to be present. A general, complete and non-scan method for measuring MMF pulses would therefore be beneficial.

To measure the complete spatiotemporal field of pulses of arbitrary waveforms, we recently developed a simple single-shot technique STRIPED FISH. Because STRIPED FISH collects all its holograms of different frequencies simultaneously, its apparatus can operate without scan and measure arbitrary pulses by retrieving the recorded holograms. For high-rep-rate laser systems commonly used in MMF optics, STRIPED FISH averages over as many pulses to generate a trace, depending on the camera shutter speed. But in fact the number of pulses needed could be very low, even to achieve single shot measurement if desired, for low-rep-rate system, such as multi-pass amplifier systems. In this chapter, we demonstrate STRIPED FISH measurements of optical fields from MMFs. We reconstructed the pulse field, and plotted movies from the measured data to intuitively display the pulse field evolutions—modal spatial, temporal and frequency structures.

6.2 Apparatus

Our apparatus for MMF output-pulse measurement is shown in Figure 6.2. Pulses from a Ti:Sapphire laser with ~60fs duration (~23 nm FWHM) centered at 800nm are sent through a spatial filter consisting of two lenses (200mm, 100mm) and a pinhole (75μm). When the flip mirror (FM) is in the beam, the filtered pulse is characterized by a FROG device GRENOUILLE (Swamp Optics, model 8-50). When the flip mirror is out of the beam, a beam splitter (BS) sends part of pulse energy (~10%) to act as the

reference pulse, which is then synchronized by a translation delay stage with the unknown pulse. The remainder of the beam passes through a single-prism pulse compressor (Swamp Optics, BOA) [95], which pre-chirps the pulse before entering MMF to yield short fiber output pulses. Dispersion compensation makes it easier to separate and identify the different modes in fiber. Pulses are sent into and out of MMFs by objective lenses (Newport, M-60X; Japan 20X 0.40), with fiber laid on a home-made 6-axis fiber mount. Small changes on fiber alignment, on the order of microns in displacement, influence greatly the light coupling efficiency into each mode. An example of on-axis and off-axis alignments of dual mode fiber is given as inset in Figure 6.2. After beam collimation, the unknown pulse output from MMF and reference pulse are recombined by BS and sent into the STRIPED FISH device.

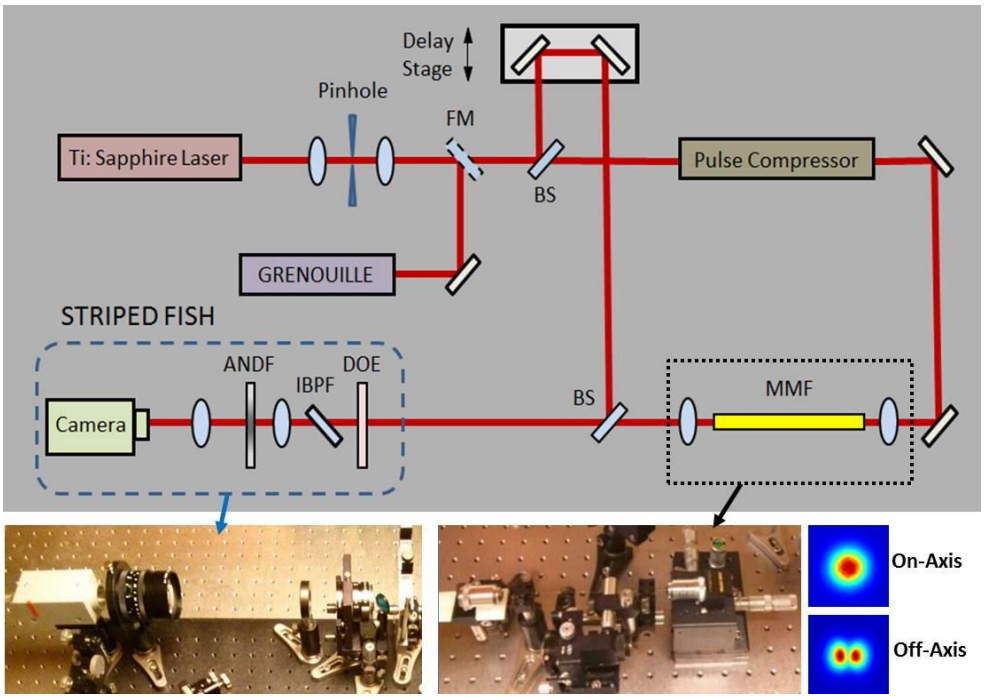

Figure 6.2. The self-referenced experimental setup to measure MMF pulses. A spatial filter (two lenses and a pinhole) and a FROG device GRENOUILLE yield the reference pulse. A pulse compressor introduces negative chirp to compensate fiber dispersion for better mode discrimination. Alignment of fiber coupling optics controls the mode coupling efficiencies. The inset shows, in on-axis and off-axis alignment cases, the measured integrated intensities of different modes for SMF980 fiber. STRIPED FISH device is shown in the bottom-left figure.

6.3 Results and Analysis

For simplicity, we study MMFs that support the first few linearly polarized (LP) modes, under weakly-guiding circumstances. To study the LP_{01} and LP_{11} modes, we use single-mode fibers designed for 980nm (Thorlabs, 980HP and SMF980-5.8-125) to operate as dual-mode fibers for our 800nm pulses. We also use telecom fiber designed for 1550nm (Thorlabs, SMF28) to study the four modes (LP_{01}, LP_{11}, LP_{21} and LP_{02}) propagation case. The pulse compressor is adjusted to give negative group-delay dispersion (-8500fs^2~-12000 fs^2) to approximately compensate the dispersion of fiber material, so the fundamental mode LP_{01} shows essentially zero chirp. The exact amount of negative dispersion introduced is determined by performing another FROG measurement after MMF and collimation lens, when only LP_{01} mode (Gaussian shape) is present and when it shows zero chirp.

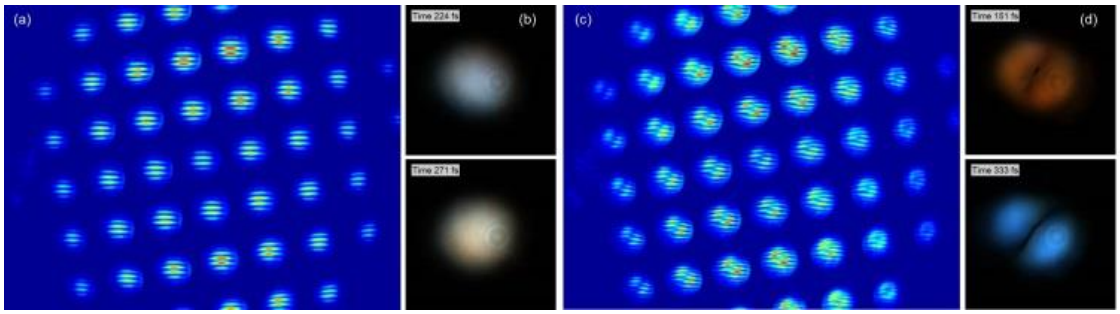

Figure 6.3. (a) STRIPED FISH trace of the LP_{01} mode from SMF980. (b) Reconstructed movie of the LP_{01} mode (Media 6.1.avi, 159KB). (c) STRIPED FISH trace of the LP_{11} mode from SMF980. (d) Reconstructed movie of the LP_{11} mode (Media 6.2.avi, 178KB).

Figure 6.3(a) and 6.3(c) show the STRIPED FISH traces of $LP_{01}$and LP_{11}modes, respectively. They are from the same fiber (SMF980, 235mm), excited by changing coupling conditions, one mode over the other. When only the fundamental mode LP_{01} is

present, as expected the measured trace is similar to the trace of a Fourier transform-limited Gaussian [96]. On the contrary, when the secondary LP_{11} mode occupies most energy, STRIPED FISH holograms show two intensity lobes and discontinuous fringes across the middle, which reflects the phase jump in the LP_{11} modal field. Two time frames are displayed in Figure 6.3(b) and 6.3(d), from movie snapshots of pulses measured from Figure 6.3(a) and 6.3(c). In each movie, pulse propagates out of screen, with color denoting frequency variation over time. As expected, the pulse in LP_{01} mode is in a Gaussian shape and has nearly no color (frequency) change over time; and the pulse in LP_{11} mode shows a double-lobe intensity with color variations over time (frequency dispersion) and a much elongated pulse length.

We investigate another MMF (SMF28, 106mm) which supports four LP modes (LP_{01}, LP_{11}, LP_{21}, and LP_{02}) for 800nm. We show the resulting STRIPED FISH trace and the retrieved pulse movie in Figure 6.4(a) and 6.4(b). The trace differs from Figure 6.3(a) of a Gaussian pulse, and it displays an intensity mixture of the different modes in each hologram. The central part of each hologram is considerably bright due to the presence of LP_{01} mode, and the relatively dim peripheral part shows intensity beating due to higher-order modes. From the movie, it is clear that different fiber modes are present, which arrive consecutively in time. Each mode, being almost white, shows little chirp in the pulse, which means the modes have different propagation velocities but similar dispersions. The coloring of the LP_{02} "doughnut" mode is likely due to the temporal interference between itself and the trailing edge of the LP_{21} "clover leaf" mode. In this particular measurement, energy in three (LP_{01}, LP_{21}, LP_{02}) modes are quite observable, but the LP_{11} mode can hardly be seen due to a very low coupling efficiency. In other

cases of off-axis fiber mount alignment, the LP_{11} mode can get much higher light coupling efficiency and have been observed in measurements.

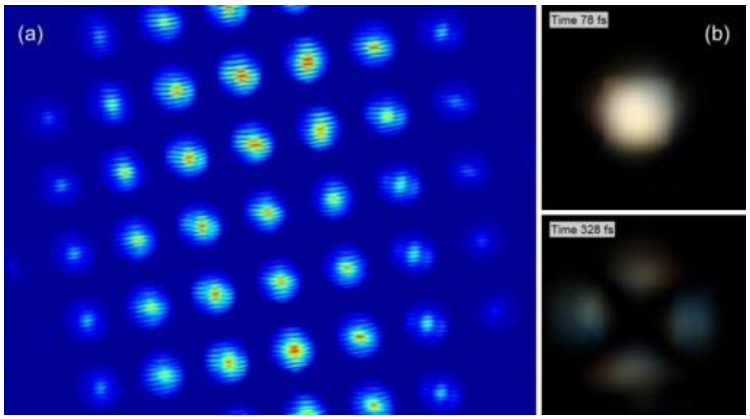

Figure 6.4. (a) STRIPED FISH trace from a four-mode fiber SMF28. (b) Reconstructed pulse movie (Media 6.3.avi, 187KB).

In addition to the above cases, mode separability can also be very important. To investigate this, we measure a pulse with simultaneous LP_{01} and LP_{11} modes excited in a two-mode fiber (980HP, 238mm). Shown in Figure 6.5(a), the STRIPED FISH trace of the measured pulse shows an "intermediate" holographic pattern between those of LP_{01} and LP_{11}, indicating the presence of both modes. Specifically, hologram intensity is in superposition form of LP_{01} and LP_{11} pattern, and the hologram fringes vary more gradually across the middle than Figure 6.3(c). In addition, lobes on the left and right show intensity beating from hologram to hologram, which indicates spectral beating between LP_{01} and LP_{11} modes. In Figure 6.5(b), the pulse movie shows two temporally overlapping modes. The chirped LP_{11} mode is significantly longer than the unchirped LP_{01} mode which only shows briefly in the middle. In fact, no matter how long fiber the pulse travels through, the temporally overlapping modes cannot be separated, as they propagate at similar velocities.

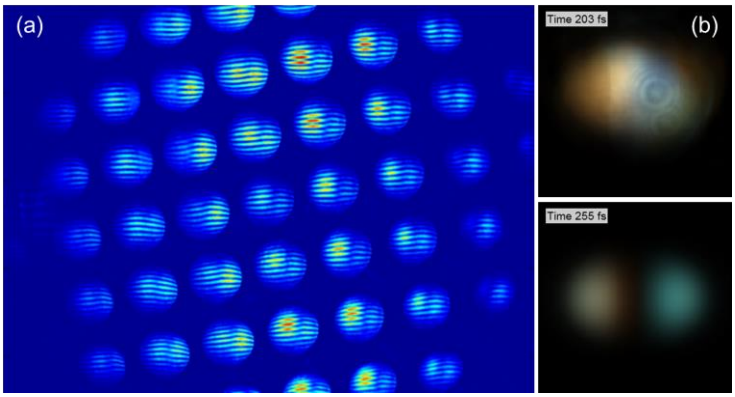

Figure 6.5. (a) STRIPED FISH trace for LP_{01} and LP_{11} modes from 980HP. (b). Retrieved pulse movie of 980HP (Media 6.4.avi, 185KB).

On the other hand, for another type of fiber (SMF980, 148mm), the modes are separable in time. As shown in Figure 6.6(a), the trace of pulse from SMF980 is also of a superposition form of LP_{01} and LP_{11}. However, the retrieved pulse movie in Figure 6.6(b) shows time-separated LP_{01} and LP_{11} modes. Therefore, depending on different fiber structures, the mode propagation velocities can be different.

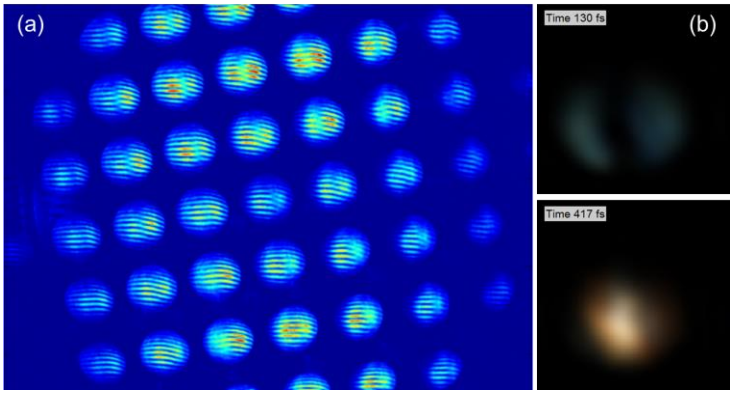

Figure 6.6. (a) STRIPED FISH trace for LP_{01} and LP_{11} modes from SMF980. (b). Retrieved pulse movie of SMF980 (Media 6.5.avi, 167KB).

The facts can be better understood if we look at pulse spectrograms. Shown in Figure 6.7(a) is the averaged spectrogram measured for a pulse from 980HP, and Figure 6.7(b) for SMF980. The averaged spectrogram is obtained by averaging all spectrograms

as in Equation (3.1) over space (x, y). As a result, the averaged spectrogram gets rid of spatial dependence, and only shows the pulse temporal and spectral profile. As we can observe, the 980HP pulse has two overlapping LP_{01} and LP_{11} modes, corresponding to the "vertical" and "tilting" parts of energy in the spectrogram. For SMF980 pulse, the "vertical" and "tilting" parts (two modes) are separate in time. The velocities of different LP modes are dependent on fiber structure parameters and also the frequency in consideration, as studied in Ref. [97].

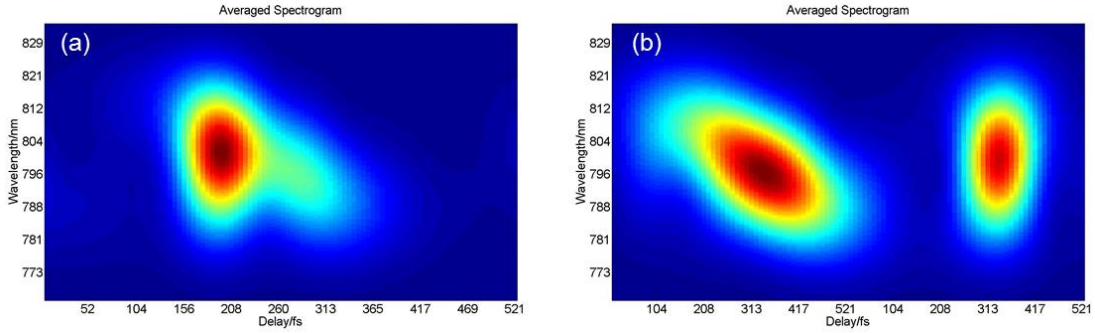

Figure 6.7. (a) Averaged spectrogram of a pulse measured from 980HP fiber. (b) Averaged spectrogram of a pulse measured from SMF980 fiber.

When the modes cannot be separated in time and space, determining how much content each mode accounts for in the field becomes important and potentially useful. From measurement, STRIPED FISH yields the complete electric field $E(x, y, t)$ or $E(x, y, \omega)$, equivalent by Fourier transform. Linearly polarized modal fields from the fiber $E_{lp}(x, y, \omega)$ form an orthogonal set, onto which an arbitrary field $E_{arb}(x, y, \omega)$ can be decomposed, by calculating overlap integrals, yielding the modal weight coefficients w_{lp}.

$$w_{lp}(\omega) = \frac{|\iint E_{arb} E_{lp}^{*}\, dx\, dy\,|^2}{\iint |E_{arb}|^2\, dx\, dy \iint |E_{lp}|^2\, dx\, dy}$$

These modal weight coefficients therefore depend on frequency, or equivalently on time, by Fourier transform. As a result, even when modes are mixed in time, it is still possible to determine the modal weights.

6.4 Summary

STRIPED FISH offers a compact solution for measuring MMF pulses. Using various fibers, under different coupling conditions, multiple spatiotemporal pulses were excited, measured, and displayed. To measure more pulse modes separated in time, a narrower-band filter would be needed in STRIPED FISH, or a delay scan can be implemented to increase the temporal coherence window. It is possible to extract information of modes from the measured complete pulse field, e.g. by calculating field overlapping integrals. After compensating fiber material dispersion, pulses of different fiber modes can be distinguished by spatial field patterns, temporal arrival time, and spectral dispersion properties.

CHAPTER 7

GENERATION, ANALYSIS AND MEASUREMENT OF ULTRAFAST LIGHTHOUSE EFFECT

In this chapter, we demonstrate the experimental measurement of ultrashort pulses with the spatial-frequency-temporal (k, t) domain amplitude coupling. This (k, t) domain coupling, known as ultrafast lighthouse effect or time-vs-angle, is the only one missed of good understanding and manipulation, among the four first-order spatiotemporal pulse amplitude couplings (the other three are pulse-front tilt, spatial chirp, and angular dispersion). Scientific values of ultrafast lighthouse effect have been proven by applications, such as attosecond pulse generation to angularly steer the sub-cycle high harmonics into isolated pulses. Here, we generated ultrafast lighthouse effect, and characterized it by using the complete pulse measurement technique STRIPED FISH. From the measurement, we observed the couplings in (k, t) and other Fourier related domains, and we demonstrate the lighthouse propagation by dynamic plots over time and space, generated from the measured pulse profile.

7.1 Introduction: Ultrafast Lighthouse Effect

In research frontiers of ultrafast optics, many attentions have been drawn to spatiotemporal field couplings these years. Benign spatiotemporal couplings lead to possible applications such as pulse shaping [98], waveform manipulating [82] and simultaneous spatial and temporal focusing [99]. At the same time, unwanted or uncharacterized pulse-field couplings can arise from misalignment [100], optical

aberration [20] or strong laser-matter interactions [24, 28], which can possibly cause issues in experiments.

There have been efforts in understanding spatiotemporal field couplings of ultrashort pulses. For example, pulse-front tilt, as a commonly observed pulse coupling in spatiotemporal domain, is usually generated by using angularly dispersive elements, such as gratings or prisms, which project different frequencies into different directions [101, 102]. However, it is also shown that [74], pulse-front tilt can also be obtained from simultaneous temporal chirp and spatial chirp, even in the absence of angular dispersion. More generally, as time and frequency are Fourier transform conjugates, and so are space coordinate and spatial frequency, any pulse-field expression in one certain domain (e.g. spatiotemporal (x, t) domain) can be translated into other domains (e.g. spatiospectral (x, ω) domain) by Fourier transform. In the theory of first-order spatiotemporal couplings [66], any coupled field can be described by a set of Gaussian expressions, where Gaussian fields in spatiotemporal (x, t), spatiospectral (x, ω), spatial-frequency-temporal (k, t) and spatial-frequency-spectral (k, ω) domains form Fourier transform pairs, and the Gaussian coefficients are interrelated. Of special interest are the four coupling terms, one in each domain, which relates a pair of different dimensions. Then, for each coupling term, its real part and imaginary part present different amplitude and phase effects in pulse, respectively.

As discussed in Chapter 2, a real amplitude coupling term and an imaginary phase coupling term exist, in each of the above four Fourier-related domains. Among these terms, in the spatial-frequency-temporal (k, t) domain, the amplitude term is named "ultrafast lighthouse effect" [66], or "time vs. angle" [65], which describes the pulse

amplitude propagation direction change as a function of time. The name "lighthouse" refers to a phenomenon that light emanates off center at different angles at different time, in vivid analogy to the ultrashort pulse propagation. Another way to understand this lighthouse effect is, as the spatial frequency vector $\vec{k}$ (directional derivative of the spatial phase) is in the same direction as the wave propagation (always perpendicular to the phase front for monochromatic field component), the (k, t) domain amplitude coupling relates the wave propagation direction to time *t*.

Although spatiotemporal couplings have many useful applications, ultrafast lighthouse effect has been extremely lack of study. Among the four amplitude couplings, spatial chirp in spatiospectral (x, ω) domain and angular dispersion in spatial-frequency-spectral (k, ω) domain are studied well and widely applied in pulse compressors [17] and pulse shapers [75]. Pulse-front tilt from spatiotemporal (x, t) domain has also been found useful in numerous applications, such as laser material processing [103, 104] and pulse measurement [12, 16, 105]. Ultrafast lighthouse effect, equally important, has been used in attosecond pulse research. By introducing couplings through slightly rotated prism wedges [106-108], thin wedge [109] or gratings [110] and a focusing mirror, lighthouse effect in the intense few-cycle exciting pulse will interact with medium such as plasma mirror, to generate a high-harmonic attosecond pulse train, with each pulse diverging at a different angle. The attosecond pulses then propagate away from each other, forming a lighthouse spiral shape which eventually lead to spatially isolated attosecond pulses (with help of a spatial gating), ready for use as light source for pump-probe measurements or photonic streaking application [107]. On the other hand, if not aware of its presence or not eliminated properly, ultrafast lighthouse effect may also cause unexpected results,

leading to possible damage or misinterpretation in experiments. However, due to its uniqueness and difficulty to measure, ultrafast lighthouse effect has not caught the deserved attention. Therefore, the characterization of ultrafast lighthouse effect is important.

7.2 Measuring Spatiotemporal Couplings by STRIPED FISH

In presence of spatiotemporal couplings in the field, any integrated measurement method that characterizes separately pulse spatial profile and pulse temporal profile cannot record the complete field information. Therefore, we used the more powerful pulse measurement technique STRIPED FISH to measure the couplings.

STRIPED FISH measurement gives us the unknown pulse transverse field over frequency $E(x, y, \omega)$, or equivalently by Fourier transform over time $E(x, y, t)$, in one certain z plane. So direct retrieval from STRIPED FISH shows the pulse evolution in the measurement plane. To yield the pulse longitudinal profile (at other z coordinates), diffraction integrals of the measured transverse field need to be carried out.

Among all first-order spatiotemporal couplings, using the Gaussian expressions for coupled dimensions, we start from the spatiotemporal (x, t) domain expression:

$$E(x,t) \propto exp\{Q_{xx}x^2 + 2Q_{xt}xt - Q_{tt}t^2\} \tag{7.1}$$

Here we have ignored the y dependence of transverse electric field, and we keep the discussion to coupling between x and t for simplicity. As we have discussed in Chapter 2, the coupling term Q_{xt} bridges the two dimensions: the real part $Re\{Q_{xt}\}$ affects the pulse field amplitude or energy distribution over x and t, therefore the pulse-front tilt; the imaginary part $Im\{Q_{xt}\}$ describes the phase variation over x and t, therefore

the wave-front rotation.

Likewise, in the spatiospectral (x, ω) domain, the Gaussian field expression is:

$$E(x, \omega) \propto \exp\{R_{xx}x^2 + 2R_{x\omega}x\omega - R_{\omega\omega}\omega^2\} \tag{7.2}$$

The amplitude coupling term $Re\{R_{x\omega}\}$ is spatial chirp, which causes frequency components in the pulse to shift in space. The phase coupling term $Im\{R_{x\omega}\}$ is wave-front-tilt dispersion, which describes the phase front direction change with respect to frequency. In STRIPED FISH, the measurement is accomplished by retrieving pulse spatial information at each different frequency. Therefore, the measured STRIPED FISH trace is in spatiospectral (x, ω) domain, and the above-mentioned two coupling terms in this domain (spatial chirp, and wave-front-tilt dispersion) can be directly observed in STRIPED FISH trace [96].

If we take Fourier transform of Equation (7.1) with respect to space, we get an expression in spatial-frequency-temporal (k, t) domain:

$$E(k, t) \propto exp\{P_{kk}k^2 + 2P_{kt}kt - P_{tt}t^2\} \tag{7.3}$$

The amplitude coupling term $Re\{P_{kt}\}$ is ultrafast lighthouse effect, which describes pulse amplitude propagation in different directions at different time. The phase coupling term $Im\{P_{kt}\}$ is named angular temporal chirp.

It is worth noting that all the discussed couplings are related by Fourier transform, so any coupling in one certain domain would generally mean the existence of other couplings in other domains. Given the field values in spatiospectral (x, ω) domain, one can perform Fourier transform to other domains for their values.

Also, as our previously used plotting scheme works in one certain z plane, field structures involving angular variations would not be displayed well. For example,

ultrafast lighthouse effect would be plotted almost the same as pulse-front tilt, given that we view the pulse only in one z plane. Therefore, while STRIPED FISH is capable of measuring spatiotemporal couplings, improvements need to be made in displaying method to also include longitudinal pulse field variations.

7.3 Experiment

To generate ultrafast lighthouse effect, we can manipulate other couplings, as they are all interrelated by Fourier transform. Specifically, from the first-order Gaussian expressions in spatiotemporal (x,t) domain and spatial-frequency-temporal (k,t) domain, we can derive a relation between coupling coefficients:

$$P_{kt} = \frac{i}{2}\frac{Q_{xt}}{Q_{xx}} \tag{7.4}$$

In terms of real and imaginary parts, ultrafast lighthouse effect corresponds to the real part of P_{kt}:

$$Re\{P_{kt}\} = \frac{1}{2}\ \frac{-Im\{Q_{xt}\}Re\{Q_{xx}\}+Re\{Q_{xt}\}Im\{Q_{xx}\}}{|Q_{xx}|^2} \tag{7.5}$$

So, as in Ref. [66], ultrafast lighthouse effect, or time vs. angle (TVA), can be denoted in terms of pulse-front tilt (PFT), wave-front curvature (WFC) and wave-front rotation (WFR) as TVA=-2WFR+2PFT×WFC, corresponding respectively to each term in the above equation. This expression means that, ultrafast lighthouse effect can originate from either wave-front rotation or focusing pulse-front tilt. Wave-front rotation, as a phase coupling effect, is difficult to manipulate by optics. On contrary, fortunately, pulse-front tilt can be easily introduced by gratings or prisms, and wave-front curvature can be controlled by lenses or curved mirrors. Therefore, focusing the pulse-front tilt is an efficient way to generate ultrafast lighthouse effect. A similar discussion in Ref. [111]

offers another interpretation. As in Figure 7.1(a), one pulse with amplitude coupling effect pulse-front tilt, is incident onto a focusing lens. Because of the pulse-front tilt, the uppermost part of the pulse arrives first at $t_0 - \delta$, and the lowest part arrives last at $t_0 + \delta$. Since the focusing lens maps incident beam position to angle at its focus, the uppermost part (with earliest arrival time) will propagate at a downward angle, and the lowest part (with latest arrival time) with propagate at an upward angle. For the beams in between, they propagate at angles closer to optical axis, and their arrival time is between the above two extreme cases. Therefore, around the lens focus, different parts of the beam propagate at different angles, with different arrival time—thus the lighthouse effect.

To measure ultrafast lighthouse effect, we built an experimental apparatus as in Figure 7.1(b). The output pulse from a Ti: Sapphire oscillator, centered at 790nm with 25nm FWHM, was temporally chirped and sent through a spatial filter made of two focusing lenses (100mm, 200mm) and one pinhole (75um). By passing through a beam splitter (BS), part of pulse energy was sent into a FROG device GRENOUILLE (Swamp Optics, model 8-20) [29]. Most energy (~90%) traveled through the first BS and got split by a second BS. The reflected beam then got delayed by a translation stage as the reference pulse, synchronized with the other arm. The transmitted beam passed through a prism pair, which introduced spatial chirp and formed pulse-front tilt with the simultaneous temporal chirp in the pulse [74]. Then the pulse-front tilted pulse got focused horizontally by a cylindrical lens. Finally, the two arms were combined through a third BS into the STRIPED FISH apparatus.

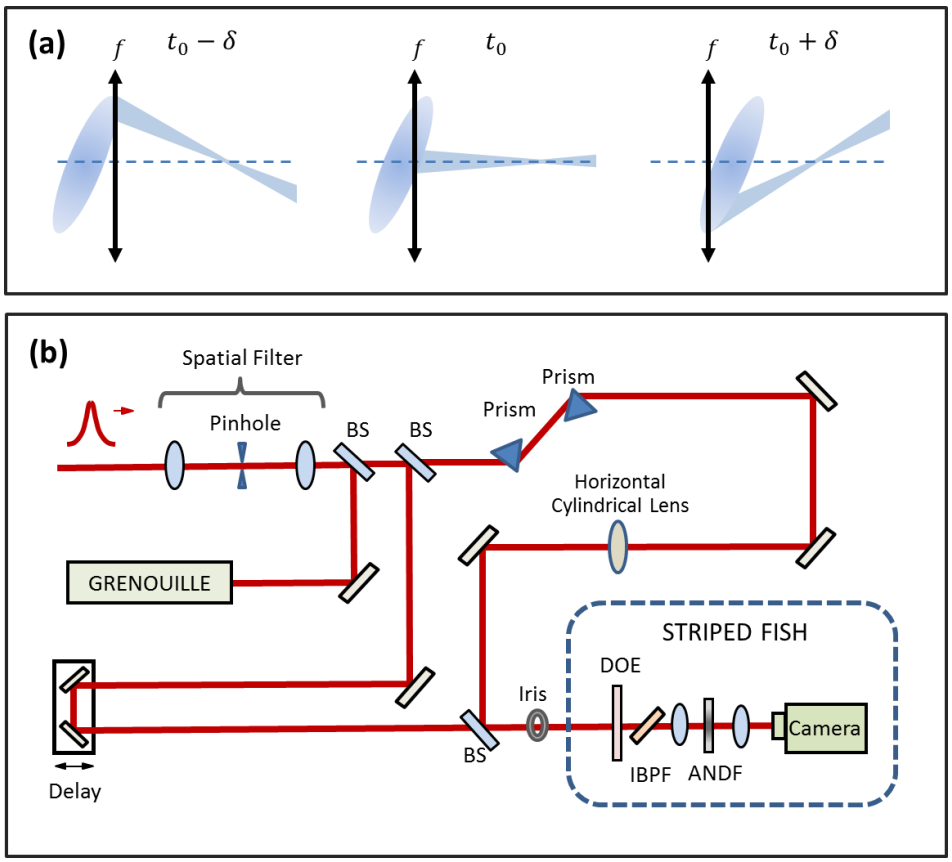

Figure 7.1. (a) Generating ultrafast lighthouse effect by focusing pulse-front tilted pulse, as discussed in Ref. [111], the Figure 2. After introducing pulse-front tilt by prism pairs, a focusing lens can map the incident beam position to angle around its focus, generating the lighthouse effect. (b) Measuring ultrafast lighthouse effect by STRIPED FISH, the experimental apparatus. Pulses from Ti: Sapphire laser traveled through a spatial filter, and got characterized by a FROG device GRENOUILLE. The Mach-Zehnder interferometer contains one arm of reference pulse, and the other arm to generate lighthouse effect by focusing pulse-front tilt. The reference pulse and unknown pulse were finally combined into STRIPED FISH device, shown in the dashed blue frame.

Once we got the result from STRIPED FISH measurement, we took Fourier transform of the measured field $E(x, y, \omega)$ into spatiotemporal domain values $E(x, y, t)$. Also, we could take one more Fourier transform with respect to space, to get into spatial-frequency-temporal (k, t) domain, where the amplitude of lighthouse effect could be observed. Here, we interpreted the presence of lighthouse effect by showing that different

parts of the pulse had different propagation directions and arrived at different time.

7.4 Results

From experiment, we measured STRIPED FISH trace for the pulse with ultrafast lighthouse effect. Then, from the retrieved spatiospectral field $E(x, y, \omega)$, we discuss the phase and amplitude variations over space and frequency. Finally, we display the lighthouse propagation over space and time using a dynamic plot, generated by calculating diffraction integrals of the measured transverse complex field.

Figure 7.2(a) shows the measured STRIPED FISH trace. By using an apodizing neural density filter (ANDF) in STRIPED FISH apparatus, we got uniformly distributed intensities over multiple diffractive orders, best utilizing the camera's range. The STRIPED FISH trace contained holograms obtained from interference of reference pulse with unknown pulse, out of which 35 holograms were used for data retrieval (marked out by white dashed line). In the trace, each hologram showed curved fringes, with steeper fringe slope on left and right. Also, hologram patterns showed a slight horizontal shift with respect to center, when we examined these holograms from low wavelength to high wavelength (left to right in Figure 7.2(a) frame). The horizontal positions of holograms corresponded to frequencies, because the transmitted wavelength of IBPF depended primarily on horizontal incidence angle. This shift of holographic patterns indicated possible spatial chirp and wave-front tilt dispersion [96], as amplitude and phase couplings in the unknown pulse.

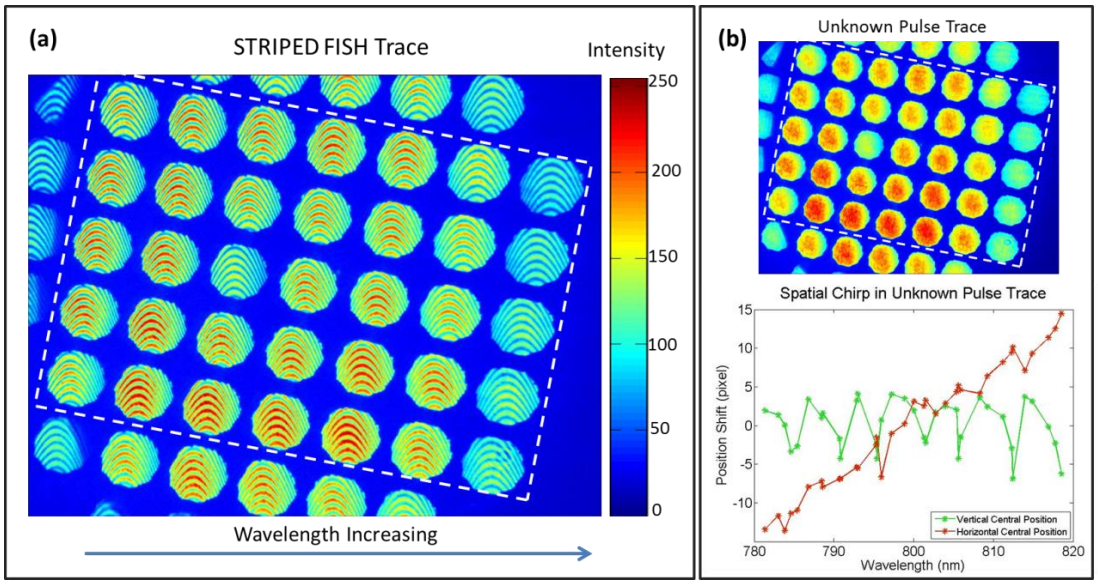

Figure 7.2. The measured STRIPED FISH traces. (a) STRIPED FISH trace from the interference of unknown and reference pulses. Pulse trace profile shows uniformly distributed intensity from order to order. The white dashed line circles out 35 holograms used for unknown pulse retrieval, with increasing wavelengths from left to right of the frame. (b) Unknown pulse trace, recorded by blocking the reference pulse arm. Trace contained diffractive orders with spatial intensity shift in horizontal direction. The intensity-weighted center shift is plotted over wavelength, for both vertical and horizontal directions, which indicates spatial chirp.

By blocking the reference arm, we recorded the pulse trace of unknown beam (Figure 7.2(b)). The unknown pulse trace, from order to order, demonstrated a horizontal intensity shift with respect to center, which indicated the presence of spatial chirp. To better illustrate, below the trace we plotted the intensity-weighted center positions of diffractive orders with respect to wavelength. Along vertical direction, the diffractive orders showed no obvious position shift over wavelength. However, in horizontal direction, they shifted from minus (left) to positive (right) with increasing wavelengths.

Then, once we retrieved the unknown pulse information from holograms, we investigated pulse phase behavior over space and frequency. For each hologram, the retrieved phase information was for one certain frequency. For example, in Figure 7.3(a), we show the measured phase for 800.05nm, from the central hologram in Figure 7.2(a),

with phase values from $-\pi$ to π. When pulse intensity was too low, the pulse phase no longer held physical significance, so corresponding phases were not shown. To get the continuous phase over space and time, we unwrapped the phase, with a code that guarantees two-dimensional phase continuity, and we plotted the unwrapped phase for 800.05nm in Figure 7.3(b). The phase showed a saddle shape along x, and almost invariant values along y, which are more clearly shown from a surface plot in Figure 7.3(c).

To investigate the spatial phase, along the central row of the measured phase matrix, we selected 155 points from each retrieved phase plot. For the 800.05nm phase plot, the selected pointes are denoted by a white dashed line in Figure 7.3(b). The selected phases were then plotted over horizontal spatial coordinates, at different wavelengths, as shown in Figure 7.3(d).

From the phases in Figure 7.3(d), we noticed that each phase showed a parabolic shape over horizontal position. This means that pulse at each wavelength showed wave-front curvature, which indicates the beam's divergence in x direction. Also, from low wavelength to high wavelength, the plotted spatial phases shift their centers (positions with zero slopes) from left to right. Note again that these spatial phases represent wave-front for a certain wavelength, and center shift can be viewed as a superposition of parabolic phase with a linearly tilted phase. Therefore, Figure 7.3(d) shows the wave-front-tilt dispersion in the pulse, which is a fundamental phase coupling effect in spatiospectral (k, ω) domain as we have reviewed.

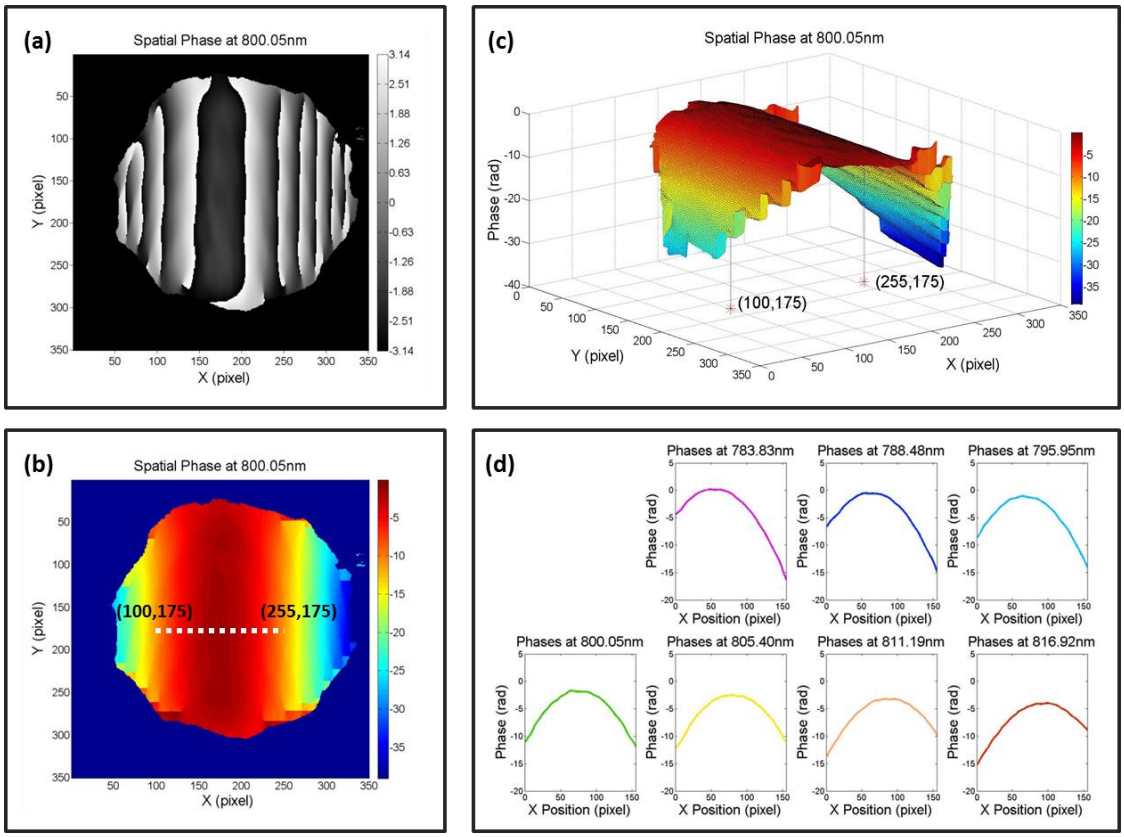

Figure 7.3. The measured phase over space by STRIPED FISH. (a) Spatial phase plot for 800.05nm, retrieved from the central hologram. (b) A two-dimensional phase unwrapping algorithm unwraps the phase over x and y. (c) The unwrapped phase plot in surface shape. (d) Spatial phases at different frequencies, retrieved from different holograms, plotted as the dashed line in (b).

Remind again that any coupling in one certain domain generally means the presence of couplings in other domains. Thus the presence of both spatial chirp and wave-front-tilt dispersion reflected the existence of ultrafast lighthouse effect in the spatial-frequency-temporal (k, t) domain.

Then, we investigated the spectral phase at different positions. Again, from the unwrapped phase we analyzed a subset of points. As in Figure 7.4(a) (reproduced from Fig. 7.3(b)) for 800.08nm, we selected five equally spaced points along the central row of each retrieved phase matrix. We plotted their phases over different frequencies, as in

Figure 7.4(b). The resulting spectral phases showed linear dependence on frequency, which means that the pulse arrives at these positions at different time. By a data fit, we extracted the spectral phase slopes and calculated delays as listed in the bottom of plot. From positions left to right, the arrival time decreased. Combined with what we have observed from Figure 7.3(d), we know that different positions in the pulse showed both spatial beam divergence (with different wave-front or wave propagation directions) and arrival time difference. So, the ultrafast lighthouse effect should be present in the pulse.

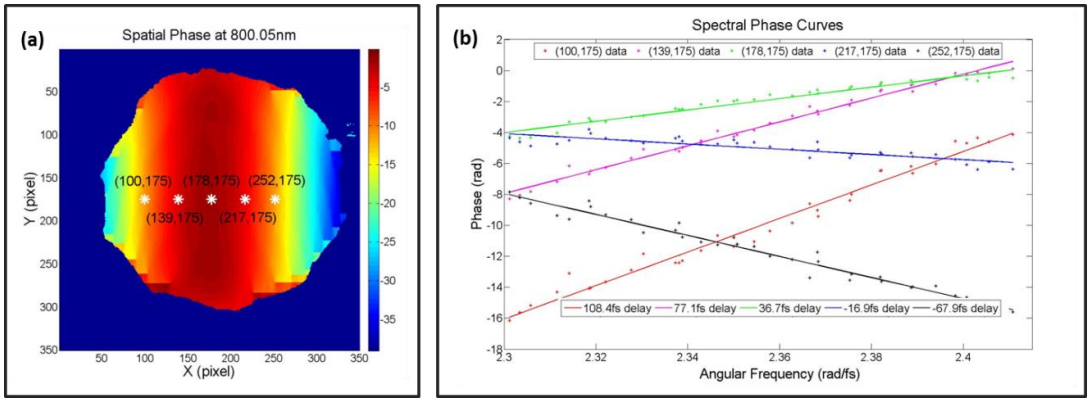

Figure 7.4. Measured spectral phase by STRIPED FISH. (a) Spatial phase plot for 800.05nm. Five points along the central row are selected, to investigate their phase behavior over frequency. (b) Spectral phase curves of all points marked in (a). Phase data points are fit over frequency by linear curves, with their slopes indicating delays as listed on bottom.

Finally, to demonstrate the lighthouse pulse propagation, we developed one type of dynamic plot scheme, based on our previously developed spectrogram RGB plotting [55]. It involves the calculation of diffraction integral for pulse propagation along longitudinal *z* direction. In Figure 7.5, we have included the measurement of pulse with lighthouse effect and simulation.

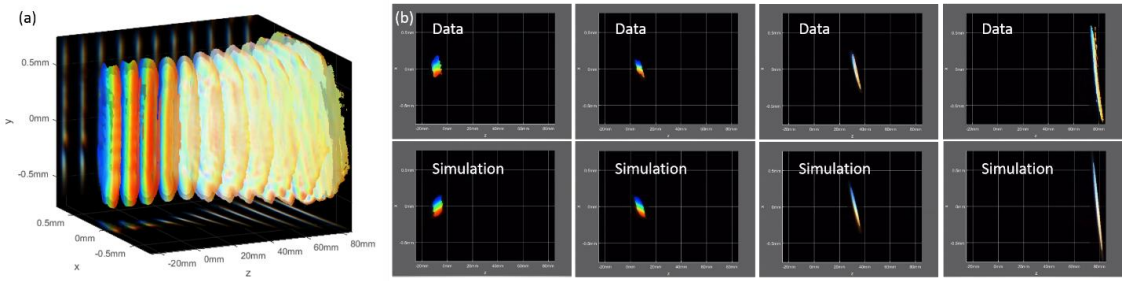

Figure 7.5. Pulse propagation plot of ultrafast lighthouse effect. The longitudinal propagation behavior is determined by calculating diffraction integrals. (a) Pulse propagation in space, at multiple z planes. (b) Lighthouse effect over time in horizontal plane, measurement (Media 7.1.avi, 277KB) and simulation (Media 7.2.avi, 247KB).

7.5 Summary

By the pulse measurement technique STRIPED FISH, we measured for the first time the ultrafast lighthouse effect in laser pulses. As the amplitude coupling term in the spatial-frequency-temporal (k, t) domain, ultrafast lighthouse effect has been generated by focusing a pulse with pulse-front tilt, implemented by a pair of prisms and a focusing cylindrical lens. Using the STRIPED FISH trace and the retrieved results, we discussed the presence of ultrafast lighthouse effect and its relation to other spatiotemporal couplings. To demonstrate lighthouse propagation, we developed a dynamic plot to include both transverse and longitudinal field variations, giving an intuitive view of the lighthouse effect over space and time.

CHAPTER 8

CONCLUSION AND FUTURE WORK

To conclude, STRIPED FISH, including its improved apparatus, pulse retrieval and processing algorithm, display method, and the understanding of its traces, offers a simple and compact solution for the ultrashort pulse spatiotemporal measurement problem. Using a single camera frame measured at one particular z plane, STRIPED FISH proves its capability to obtain full spatiotemporal information of the measured pulse from multiple recorded holograms at different frequencies. To assist the measurement, STRIPED FISH uses a spatial filter and a FROG measurement to generate and characterize a reference pulse. If any pulse train instability is present, it can be reflected by the FROG trace of the reference pulse. STRIPED FISH can work in a self-reference geometry, which guarantees the coherence between the reference pulse and the unknown pulse. Using STRIPED FISH, we should be able to measure or monitor pulses of various types. In this thesis, as examples, we investigated pulses with chirped pulse beating, pulses in multimode optical fiber modes, pulses with ultrafast lighthouse effect, and so on, obtaining large amount of information regarding the pulse fields. We believe that STRIPED FISH can characterize various complex pulse distortions, and hopefully help manipulate them in pulse applications.

To make sure this powerful technique works for certain pulse durations and wavelength ranges, STRIPED FISH requires efforts in designing, building and calibrating the device.

For example, when designing the device, we need to determine the IBPF by the pulse central wavelength and pulse bandwidth. From the angle-wavelength-tuning curve of the filter (usually provided by the vendors), we can calculate the angle range required to cover the whole pulse spectrum. Usually the IBPF is operated at tilted angles to best utilize the linearly varying angle-wavelength-tuning region. Then, once the IBPF and angle range are chosen, we can design the structures on the DOE to give corresponding divergent angles, with a desired number of diffractive orders (which is also the number of holograms later). Depending on different divergent angles, the way to handle possible optical aberration could be different. As with small beam size and divergent angles, singlet lenses could be found sufficient. In building the device, we need to be careful about alignment, optical aberration, the unknown pulse and reference pulse intensity ratio, delay synchronization, and intensity homogeneity among multiple holograms, to make sure that holograms on the camera are well imaged and with great fringe visibility. In calibration, we need to register locations of different holograms, and use the fiber spectrometers to determine frequency values of each diffractive order. Once the device is built and fixed on board, we need to run calibrations to determine the exact imaging condition, including the magnification ratio, the wavelength and spatial orientations. To record holograms properly for pulse retrieval, depending on the laser power and pulse potential complexity, we need to choose the proper shutter speed and exposure time, the right FROG measurement device, beam crossing angle in holograms and so on. STRIPED FISH device would need certain amount of pulse energy to work with, because it uses a FROG device (usually GRENOUILLE) to assist the measurement which involves optical nonlinearity (e.g. SHG). To guarantee a reasonable signal-to-noise ratio,

there should also be sufficient energy for the unknown pulse to travel through the DOE, IBPF and ANDF, to finally form holograms on the camera. Also, we should look into using more sensitive cameras and with more recording digits than the current CMOS ones to record and retrieve holograms with less noise.

Further improvements to the STRIPED FISH device could involve extension to more complex pulses, which would require scaling up the number of holograms, by, for example, using a larger camera sensor. Extension to longer pulses would require increasing the spectral resolution, which could be difficult in view of currently available filter bandwidths, angular dispersion's tendency to spatially smear the resulting holograms, and the resulting aberration due to increasing divergence of the many beams after DOE. So other spectrally resolving approaches such as etalons can be considered.

On the other hand, this device can be easily adapted to other wavelength ranges by selecting proper parameters of DOE and IBPF, and optics for the imaging system. For example, it is possible to get the measurement wavelength range to cover a typical 1053nm Nd: YAG fs laser. For an IBPF with effective refraction index of 2.05 (typical value), the filter central transmission wavelength can be fixed around 1100nm. Then the filter would transmit at about 1053nm at ~30 degrees of tilt incidence. As the design of DOE structures also depend on the pulse bandwidth, and as a typical 1053nm Nd: YAG laser is usually of a narrower bandwidth than 800nm Ti: Sapphire laser, typically less divergence angle (less than ~15 degrees) is need from DOE to cover the whole lasing range, which makes it easier to handle the resulting optical aberrations.

In its current form, STRIPED FISH, as the only single-frame and complete spatiotemporal pulse measurement technique, to our knowledge, should be able to measure many ultrashort pulses from various systems (laser oscillators, chirped pulse amplifiers, multimode fibers, etc.) for their field structures and especially possible pulse distortions.

REFERENCES

1. R. W. Boyd, *Nonlinear optics* (Academic press, 2003).

2. J. W. Goodman, *Introduction to Fourier optics* (Roberts and Company Publishers, 2005).

3. W. Demtröder, *Laser spectroscopy: basic concepts and instrumentation* (Springer Science & Business Media, 2013).

4. R. Loudon, *The quantum theory of light* (OUP Oxford, 2000).

5. A. Weiner, *Ultrafast optics* (John Wiley & Sons, 2011), Vol. 72.

6. P. Hannaford, *Femtosecond laser spectroscopy* (Springer Science & Business Media, 2004).

7. R. Trebino, *Frequency-Resolved Optical Gating: The Measurement of Ultrashort Laser Pulses* (Kluwer Academic Publishers, Boston, 2002).

8. R. Trebino, K. W. DeLong, D. N. Fittinghoff, J. N. Sweetser, M. A. Krumbügel, and D. J. Kane, "Measuring Ultrashort Laser Pulses in the Time-Frequency Domain Using Frequency-Resolved Optical Gating," Review of Scientific Instruments **68**(9), 3277-3295 (1997).

9. F. Quéré, Y. Mairesse, and J. Itatani, "Temporal characterization of attosecond XUV fields," Journal of Modern Optics **52**(2-3), 339-360 (2005).

10. K. Michelmann, T. Feurer, R. Fernsler, and R. Sauerbrey, "Frequency resolved optical gating in the UV using the electronic Kerr effect," Applied Physics B **63**(5), 485-489 (1996).

11. B. A. Richman, M. A. Krumbügel, and R. Trebino, "Temporal Characterization of Mid-IR Free-Electron-Laser Pulses by Frequency-Resolved Optical Gating," Opt. Lett. **22**(10), 721-723 (1997).

12. P. Bowlan and R. Trebino, "Complete single-shot measurement of arbitrary nanosecond laser pulses in time," Opt. Expr. **19**(2), 1367-1377 (2011).

13. Y. Mairesse and F. Quéré, "Frequency-resolved optical gating for complete reconstruction of attosecond bursts," Physical Review A **71**(1), 011401 (2005).

14. J.-C. Chanteloup, E. Salmon, C. Sauteret, A. Migus, P. Zeitoun, A. Klisnick, A. Carillon, S. Hubert, D. Ros, and P. Nickles, "Pulse-front control of 15-TW pulses

with a tilted compressor, and application to the subpicosecond traveling-wave pumping of a soft-x-ray laser," JOSA B **17**(1), 151-157 (2000).

15. B. A. Richman, S. E. Bisson, R. Trebino, E. Sidick, and A. Jacobson, "All-prism achromatic phase matching for tunable second-harmonic generation," Applied Optics **38**(15), 3316-3323 (1999).

16. T. C. Wong and R. Trebino, "Single-frame measurement of complex laser pulses tens of picoseconds long using pulse-front tilt in cross-correlation frequency-resolved optical gating," JOSA B **30**(11), 2781-2786 (2013).

17. V. Chauhan, P. Bowlan, J. Cohen, and R. Trebino, "Single-diffraction-grating and grism pulse compressors," Journal of the Optical Society of America B **27**(4), 619-624 (2010).

18. F. Frei, A. Galler, and T. Feurer, "Space-time coupling in femtosecond pulse shaping and its effects on coherent control," The Journal of chemical physics **130**(3), 034302 (2009).

19. S. Cundiff, E. Ippen, H. Haus, and W. Knox, "Frequency-dependent mode size in broadband Kerr-lens mode locking," Optics Letters **21**(9), 662-664 (1996).

20. Z. Bor, "Distortion of femtosecond laser pulses in lenses and lens systems," Journal of Modern Optics **35**(12), 1907-1918 (1988).

21. P. Bowlan, P. Gabolde, and R. Trebino, "Directly measuring the spatio-temporal electric field of focusing ultrashort pulses," Opt. Expr. **15**, 10219-10230 (2007).

22. M. Kempe and W. Rudolph, "Femtosecond pulses in the focal region of lenses," Physical Review A **48**(6), 4721 (1993).

23. J. Jasapara and W. Rudolph, "Characterization of sub-10-fs pulse focusing with high-numerical-aperture microscope objectives," Optics Letters **24**(11), 777-779 (1999).

24. H. Kumagai, S.-H. Cho, K. Ishikawa, K. Midorikawa, M. Fujimoto, S.-i. Aoshima, and Y. Tsuchiya, "Observation of the complex propagation of a femtosecond laser pulse in a dispersive transparent bulk material," JOSA B **20**(3), 597-602 (2003).

25. A. Matijošius, P. Di Trapani, A. Dubietis, R. Piskarskas, A. Varanavičius, and A. Piskarskas, "Nonlinear space-time dynamics of ultrashort wave packets in water," Optics Letters **29**(10), 1123-1125 (2004).

26. D. Faccio, M. A. Porras, A. Dubietis, F. Bragheri, A. Couairon, and P. Di Trapani, "Conical emission, pulse splitting, and X-wave parametric amplification

in nonlinear dynamics of ultrashort light pulses," Physical Review Letters **96**(19), 193901 (2006).

27. A. Couairon and A. Mysyrowicz, "Femtosecond filamentation in transparent media," Physics reports **441**(2), 47-189 (2007).

28. D. E. Adams, T. A. Planchon, A. Hrin, J. A. Squier, and C. G. Durfee, "Characterization of coupled nonlinear spatiospectral phase following an ultrafast self-focusing interaction," Optics Letters **34**(9), 1294-1296 (2009).

29. P. O'Shea, M. Kimmel, X. Gu, and R. Trebino, "Highly simplified device for ultrashort-pulse measurement," Optics Letters **26**(12), 932-934 (2001).

30. S. Akturk, M. Kimmel, P. O'Shea, and R. Trebino, "Extremely simple device for measuring 20-fs pulses," Opt. Lett. **29**(9), 1025-1027 (2004).

31. S. Akturk, M. Kimmel, P. O'Shea, and R. Trebino, "Measuring spatial chirp in ultrashort pulses using single-shot Frequency-Resolved Optical Gating," Opt. Expr. **11**(1), 68-78 (2003).

32. S. Akturk, M. Kimmel, P. O'Shea, and R. Trebino, "Measuring pulse-front tilt in ultrashort pulses using GRENOUILLE," Opt. Expr. **11**(5), 491-501 (2003).

33. S. Akturk, X. Gu, P. Bowlan, and R. Trebino, "Spatio-temporal couplings in ultrashort laser pulses," Journal of Optics **12**, 093001 (2010).

34. I. A. Walmsley and C. Dorrer, "Characterization of ultrashort electromagnetic pulses," Advances in Optics and Photonics **1**(2), 308-437 (2009).

35. F. Bragheri, D. Faccio, F. Bonaretti, A. Lotti, M. Clerici, O. Jedrkiewicz, C. Liberale, S. Henin, L. Tartara, and V. Degiorgio, "Complete retrieval of the field of ultrashort optical pulses using the angle-frequency spectrum," Optics Letters **33**(24), 2952-2954 (2008).

36. S. Kahaly, S. Monchocé, V. Gallet, O. Gobert, F. Réau, O. Tcherbakoff, P. D'Oliveira, P. Martin, and F. Quéré, "Investigation of amplitude spatio-temporal couplings at the focus of a 100 tw-25 fs laser," Applied Physics Letters **104**(5), 054103 (2014).

37. C. Dorrer, E. Kosik, and I. Walmsley, "Direct space–time characterization of the electric fields of ultrashort optical pulses," Optics Letters **27**(7), 548-550 (2002).

38. C. Dorrer, E. Kosik, and I. Walmsley, "Spatio-temporal characterization of the electric field of ultrashort optical pulses using two-dimensional shearing interferometry," Applied Physics B **74**(1), s209-s217 (2002).

39. L. Gallmann, G. Steinmeyer, D. Sutter, T. Rupp, C. Iaconis, I. Walmsley, and U. Keller, "Spatially resolved amplitude and phase characterization of femtosecond optical pulses," Optics Letters **26**(2), 96-98 (2001).

40. A. S. Wyatt, I. A. Walmsley, G. Stibenz, and G. Steinmeyer, "Sub-10 fs pulse characterization using spatially encoded arrangement for spectral phase interferometry for direct electric field reconstruction," Optics Letters **31**(12), 1914-1916 (2006).

41. E. M. Kosik, A. S. Radunsky, I. A. Walmsley, and C. Dorrer, "Interferometric technique for measuring broadband ultrashort pulses at the sampling limit," Optics Letters **30**(3), 326-328 (2005).

42. F. Bonaretti, D. Faccio, M. Clerici, J. Biegert, and P. Di Trapani, "Spatiotemporal amplitude and phase retrieval of Bessel-X pulses using a Hartmann-Shack sensor," Optics Express **17**(12), 9804-9809 (2009).

43. E. Rubino, D. Faccio, L. Tartara, P. K. Bates, O. Chalus, M. Clerici, F. Bonaretti, J. Biegert, and P. Di Trapani, "Spatiotemporal amplitude and phase retrieval of space-time coupled ultrashort pulses using the Shackled-FROG technique," Optics Letters **34**(24), 3854-3856 (2009).

44. S. L. Cousin, J. M. Bueno, N. Forget, D. R. Austin, and J. Biegert, "Three-dimensional spatiotemporal pulse characterization with an acousto-optic pulse shaper and a Hartmann–Shack wavefront sensor," Optics Letters **37**(15), 3291-3293 (2012).

45. C. Hauri, J. Biegert, U. Keller, B. Schaefer, K. Mann, and G. Marowski, "Validity of wave-front reconstruction and propagation of ultrabroadband pulses measured with a Hartmann–Shack sensor," Optics Letters **30**(12), 1563-1565 (2005).

46. W. Amir, T. A. Planchon, C. G. Durfee, J. A. Squier, P. Gabolde, R. Trebino, and M. Müller, "Simultaneous visualization of spatial and chromatic aberrations by 2D Fourier Transform Spectral Interferometry," Opt. Lett. **31**(19), 2927 (2006).

47. W. Amir, T. Planchon, C. Durfee, and J. Squier, "Complete characterization of a spatiotemporal pulse shaper with two-dimensional Fourier transform spectral interferometry," Optics Letters **32**(8), 939-941 (2007).

48. P. Bowlan, P. Gabolde, A. Shreenath, K. McGresham, R. Trebino, and S. Akturk, "Crossed-beam spectral interferometry: a simple, high-spectral-resolution method for completely characterizing complex ultrashort pulses in real time," Opt. Expr. **14**(24), 11892 (2006).

49. B. Alonso, Í. J. Sola, Ó. Varela, J. Hernández-Toro, C. Méndez, J. San Román, A. Zaïr, and L. Roso, "Spatiotemporal amplitude-and-phase reconstruction by

Fourier-transform of interference spectra of high-complex-beams," JOSA B **27**(5), 933-940 (2010).

50. F. Eilenberger, A. Brown, S. Minardi, and T. Pertsch, "Imaging cross-correlation FROG: measuring ultrashort, complex, spatiotemporal fields," Optics Express **21**(22), 25968-25976 (2013).

51. J. Trull, O. Jedrkiewicz, P. Di Trapani, A. Matijosius, A. Varanavicius, G. Valiulis, R. Danielius, E. Kucinskas, A. Piskarskas, and S. Trillo, "Spatiotemporal three-dimensional mapping of nonlinear X waves," Physical Review E **69**(2), 026607 (2004).

52. B. Alonso, I. Sola, O. Varela, C. Méndez, I. Arias, J. San Román, A. Zaïr, and L. Roso, "Spatio-temporal characterization of laser pulses by spatially resolved spectral interferometry," Opt. Pura Apl **43**(1)(2010).

53. N. Mehta, C. Yang, Y. Xu, and Z. Liu, "Characterization of the spatiotemporal evolution of ultrashort optical pulses using FROG holography," Optics Express **22**(9), 11099-11106 (2014).

54. P. Gabolde and R. Trebino, "Single-shot measurement of the full spatiotemporal field of ultrashort pulses with multispectral digital holography," Opt. Expr. **14**(23), 11460 (2006).

55. Z. Guang, M. Rhodes, M. Davis, and R. Trebino, "Complete characterization of a spatiotemporally complex pulse by an improved single-frame pulse-measurement technique," JOSA B **31**(11), 2736-2743 (2014).

56. P. Gabolde and R. Trebino, "Single-frame measurement of the complete spatio-temporal intensity and phase of ultrashort laser pulse(s) using wavelength-multiplexed digital holography," J. Opt. Soc. Am. B **25**(6), A25-A33 (2008).

57. J. Giordmaine, P. Rentzepis, S. Shapiro, and K. Wecht, "TWO-PHOTON EXCITATION OF FLUORESCENCE BY PICOSECOND LIGHT PULSES," Applied Physics Letters **11**(7), 216-218 (1967).

58. J. Armstrong, "Measurement of picosecond laser pulse widths," Applied Physics Letters **10**(1), 16-18 (1967).

59. K. L. Sala, G. A. Kenney-Wallace, and G. E. Hall, "CW autocorrelation measurements of picosecond laser pulses," Quantum Electronics, IEEE Journal of **16**(9), 990-996 (1980).

60. D. J. Kane and R. Trebino, "Characterization of Arbitrary Femtosecond Pulses Using Frequency Resolved Optical Gating," IEEE Journal of Quantum Electronics **29**(2), 571-579 (1993).

61. C. Iaconis and I. A. Walmsley, "Spectral phase interferometry for direct electric-field reconstruction of ultrashort optical pulses," Optics Letters **23**(10), 792-794 (1998).

62. C. Iaconis and I. A. Walmsley, "Self-referencing spectral interferometry for measuring ultrashort optical pulses," Quantum Electronics, IEEE Journal of **35**(4), 501-509 (1999).

63. J. Ratner, G. Steinmeyer, T. C. Wong, R. Bartels, and R. Trebino, "Coherent artifact in modern pulse measurements," Optics Letters **37**(14), 2874-2876 (2012).

64. M. Rhodes, G. Steinmeyer, J. Ratner, and R. Trebino, "Pulse-shape instabilities and their measurement," Laser & Photonics Reviews **7**(4), 557-565 (2013).

65. A. Kostenbauder, "Ray-pulse matrices: a rational treatment for dispersive optical systems," Quantum Electronics, IEEE Journal of **26**(6), 1148-1157 (1990).

66. S. Akturk, X. Gu, P. Gabolde, and R. Trebino, "The general theory of first-order spatio-temporal distortions of Gaussian pulses and beams," Opt. Expr. **13**(21), 8642-8661 (2005).

67. M. Takeda, H. Ina, and S. Kobayashi, "Fourier-transform method of fringe-pattern analysis for computer-based topography and interferometry," JOSA **72**(1), 156-160 (1982).

68. P. Gabolde and R. Trebino, "Self-referenced measurement of the complete electric field of ultrashort pulses," Opt. Expr. **12**(19), 4423 - 4429 (2004).

69. L. Yu and M. K. Kim, "Wavelength-scanning digital interference holography for tomographic three-dimensional imaging by use of the angular spectrum method," Optics Letters **30**(16), 2092-2094 (2005).

70. E. Arons, D. Dilworth, M. Shih, and P. Sun, "Use of Fourier synthesis holography to image through inhomogeneities," Optics Letters **18**(21), 1852-1854 (1993).

71. Y. Garini, I. T. Young, and G. McNamara, "Spectral imaging: principles and applications," Cytometry Part A **69**(8), 735-747 (2006).

72. N. Gat, "Imaging spectroscopy using tunable filters: a review," presented at the AeroSense 2000, 2000.

73. G. P. Agrawal, *Nonlinear fiber optics* (Academic press, 2007).

74. S. Akturk, X. Gu, E. Zeek, and R. Trebino, "Pulse-front tilt caused by spatial and temporal chirp " Opt. Expr. **12**(19), 4399 - 4410 (2004).

75. A. M. Weiner, "Femtosecond pulse shaping using spatial light modulators," Review of Scientific Instruments **71**(5), 1929-1960 (2000).

76. P. Bowlan, U. Fuchs, R. Trebino, and U. D. Zeitner, "Measuring the spatiotemporal electric field of tightly focused ultrashort pulses with sub-micron spatial resolution," Optics Express **16**(18), 13663-13675 (2008).

77. W. D. Mark, "Spectral analysis of the convolution and filtering of non-stationary stochastic processes," Journal of sound and vibration **11**(1), 19-63 (1970).

78. R. Ryf, S. Randel, A. H. Gnauck, C. Bolle, A. Sierra, S. Mumtaz, M. Esmaeelpour, E. C. Burrows, R.-J. Essiambre, and P. J. Winzer, "Mode-division multiplexing over 96 km of few-mode fiber using coherent 6 6 MIMO processing," Lightwave Technology, Journal of **30**(4), 521-531 (2012).

79. P. Lissberger and W. Wilcock, "Properties of all-dielectric interference filters. II. Filters in parallel beams of light incident obliquely and in convergent beams," JOSA **49**(2), 126-128 (1959).

80. M. Bass, E. W. Van Stryland, D. R. Williams, and W. L. Wolfe, *Handbook of optics* (McGraw-Hill, 2001), Vol. 2.

81. Q. Wu, Y. Semenova, P. Wang, and G. Farrell, "High sensitivity SMS fiber structure based refractometer–analysis and experiment," Optics Express **19**(9), 7937-7944 (2011).

82. O. Katz, E. Small, Y. Bromberg, and Y. Silberberg, "Focusing and compression of ultrashort pulses through scattering media," Nature Photonics **5**(6), 372-377 (2011).

83. I. N. Papadopoulos, S. Farahi, C. Moser, and D. Psaltis, "High-resolution, lensless endoscope based on digital scanning through a multimode optical fiber," Biomedical optics express **4**(2), 260-270 (2013).

84. T. Čižmár and K. Dholakia, "Shaping the light transmission through a multimode optical fibre: complex transformation analysis and applications in biophotonics," Optics Express **19**(20), 18871-18884 (2011).

85. D. Richardson, J. Nilsson, and W. Clarkson, "High power fiber lasers: current status and future perspectives [Invited]," JOSA B **27**(11), B63-B92 (2010).

86. H. Itoh, T. Urakami, S.-i. Aoshima, and Y. Tsuchiya, "Femtosecond pulse delivery through long multimode fiber using adaptive pulse synthesis," Japanese journal of applied physics **45**(7R), 5761 (2006).

87. Y. Vidne and M. Rosenbluh, "Spatial modes in a PCF fiber generated continuum," Optics Express **13**(24), 9721-9728 (2005).

88. L. G. Wright, W. H. Renninger, D. N. Christodoulides, and F. W. Wise, "Spatiotemporal dynamics of multimode optical solitons," Optics Express **23**(3), 3492-3506 (2015).

89. G. D. Hesketh, F. Poletti, and P. Horak, "Spatio-Temporal Self-Focusing in Femtosecond Pulse Transmission Through Multimode Optical Fibers," Lightwave Technology, Journal of **30**(17), 2764-2769 (2012).

90. J. Nicholson, A. Yablon, S. Ramachandran, and S. Ghalmi, "Spatially and spectrally resolved imaging of modal content in large-mode-area fibers," Optics Express **16**(10), 7233-7243 (2008).

91. D. Schimpf, R. Barankov, and S. Ramachandran, "Cross-correlated (C 2) imaging of fiber and waveguide modes," Optics Express **19**(14), 13008-13019 (2011).

92. R. Rokitski and S. Fainman, "Propagation of ultrashort pulses in multimode fiber in space and time," Optics Express **11**(13), 1497-1502 (2003).

93. T. Kaiser, D. Flamm, S. Schröter, and M. Duparré, "Complete modal decomposition for optical fibers using CGH-based correlation filters," Optics Express **17**(11), 9347-9356 (2009).

94. F. Stutzki, H.-J. Otto, F. Jansen, C. Gaida, C. Jauregui, J. Limpert, and A. Tünnermann, "High-speed modal decomposition of mode instabilities in high-power fiber lasers," Optics Letters **36**(23), 4572-4574 (2011).

95. S. Akturk, X. Gu, M. Kimmel, and R. Trebino, "Extremely simple single-prism ultrashort-pulse compressor," Opt. Expr. **14**(21), 10101-10108 (2006).

96. Z. Guang, M. Rhodes, and R. Trebino, "Numerical simulations of holographic spatiospectral traces of spatiotemporally distorted ultrashort laser pulses," Applied Optics **54**(22), 6640-6651 (2015).

97. D. Gloge, "Weakly guiding fibers," Applied Optics **10**(10), 2252-2258 (1971).

98. A. M. Weiner, J. P. Heritage, and E. Kirschner, "High-resolution femtosecond pulse shaping," JOSA B **5**(8), 1563-1572 (1988).

99. G. Zhu, J. Van Howe, M. Durst, W. Zipfel, and C. Xu, "Simultaneous spatial and temporal focusing of femtosecond pulses," Optics Express **13**(6), 2153-2159 (2005).

100. C. Fiorini, C. Sauteret, C. Rouyer, N. Blanchot, S. Seznec, and A. Migus, "Temporal aberrations due to misalignments of a stretcher-compressor system and compensation," Quantum Electronics, IEEE Journal of **30**(7), 1662-1670 (1994).

101. Z. Bor, B. Racz, G. Szabo, M. Hilbert, and H. Hazim, "Femtosecond pulse front tilt caused by angular dispersion," Optical Engineering **32**(10), 2501-2504 (1993).

102. J. Hebling, "Derivation of the pulse front tilt caused by angular dispersion," Optical and Quantum Electronics **28**(12), 1759-1763 (1996).

103. E. Block, J. Thomas, C. Durfee, and J. Squier, "Integrated single grating compressor for variable pulse front tilt in simultaneously spatially and temporally focused systems," Optics Letters **39**(24), 6915-6918 (2014).

104. D. Asoubar, R. Kammel, S. Nolte, and F. Wyrowski, "Analysis of pulse front tilt in simultaneous spatial and temporal focusing," JOSA A **31**(11), 2437-2446 (2014).

105. P. Bowlan and R. Trebino, "Extreme pulse-front tilt from an etalon," J. Opt. Soc. Am. B **27**(11), 2322-2327 (2010).

106. J. A. Wheeler, A. Borot, S. Monchocé, H. Vincenti, A. Ricci, A. Malvache, R. Lopez-Martens, and F. Quéré, "Attosecond lighthouses from plasma mirrors," Nature Photonics **6**(12), 829-833 (2012).

107. K. T. Kim, C. Zhang, T. Ruchon, J.-F. Hergott, T. Auguste, D. Villeneuve, P. Corkum, and F. Quéré, "Photonic streaking of attosecond pulse trains," Nature Photonics **7**(8), 651-656 (2013).

108. T. Hammond, K. T. Kim, C. Zhang, D. Villeneuve, and P. Corkum, "Controlling attosecond angular streaking with second harmonic radiation," Optics Letters **40**(8), 1768-1770 (2015).

109. C. Zhang, G. Vampa, D. Villeneuve, and P. Corkum, "Attosecond lighthouse driven by sub-two-cycle, 1.8? m laser pulses," Journal of Physics B: Atomic, Molecular and Optical Physics **48**(6), 061001 (2015).

110. H. Vincenti and F. Quéré, "Attosecond lighthouses: how to use spatiotemporally coupled light fields to generate isolated attosecond pulses," Physical Review Letters **108**(11), 113904 (2012).

111. H. Vincenti, A. Borot, T. Hammond, K. T. Kim, J. Wheeler, C. Zhang, T. Ruchon, T. Auguste, J. Hergott, and D. Villeneuve, "Applications of ultrafast wavefront rotation in highly nonlinear optics," Journal of Physics B: Atomic, Molecular and Optical Physics **47**(12), 124004 (2014).